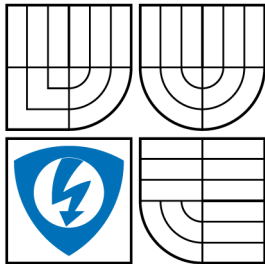


BRNO UNIVERSITY OF TECHNOLOGY  
VYSOKÉ UČENÍ TECHNICKÉ V BRNĚ



FACULTY OF ELECTRICAL ENGINEERING AND  
COMMUNICATION  
DEPARTMENT OF RADIO ELECTRONICS

FAKULTA ELEKTROTECHNIKY A KOMUNIKAČNÍCH  
TECHNOLOGIÍ  
ÚSTAV RADIOELEKTRONIKY

## DIFFRACTION EFFECTS IN TRANSMITTED OPTICAL BEAM

DIFRAKČNÍ JEVY VE VYSÍLANÉM OPTICKÉM SVAZKU

DOCTORAL THESIS  
DIZERTAČNÍ PRÁCE

AUTHOR  
AUTOR PRÁCE

Ing. JURAJ POLIAK

SUPERVISOR  
VEDOUCÍ PRÁCE

prof. Ing. OTAKAR WILFERT, CSc.

BRNO 2014

## **ABSTRACT**

The thesis was set out to investigate on the wave and electromagnetic effects occurring during the restriction of an elliptical Gaussian beam by a circular aperture. First, from the Huygens-Fresnel principle, two models of the Fresnel diffraction were derived. These models provided means for defining contrast of the diffraction pattern that can be used to quantitatively assess the influence of the diffraction effects on the optical link performance. Second, by means of the electromagnetic optics theory, four expressions (two exact and two approximate) of the geometrical attenuation were derived. The study shows also the misalignment analysis for three cases – lateral displacement and angular misalignment of the transmitter and the receiver, respectively. The expression for the misalignment attenuation of the elliptical Gaussian beam in FSO links was also derived. All the aforementioned models were also experimentally proven in laboratory conditions in order to eliminate other influences. Finally, the thesis discussed and demonstrated the design of the all-optical transceiver. First, the design of the optical transmitter was shown followed by the development of the receiver optomechanical assembly. By means of the geometric and the matrix optics, relevant receiver parameters were calculated and alignment tolerances were estimated.

## **KEYWORDS**

Free-space optical link, Fresnel diffraction, geometrical loss, pointing error, all-optical transceiver design

## **ABSTRAKT**

Dizertačná práca pojednáva o vlnových a elektromagnetických javoch, ku ktorým dochádza pri zatičení eliptického Gausovského zväzku kruhovou apertúrou. Najprv boli z Huygensovho-Fresnelovho princípu odvodené dva modely Fresnelovej difrakcie. Tieto modely poskytli nástroj pre zavedenie kontrastu difrakčného obrazca ako veličiny, ktorá kvantifikuje vplyv difrakčných javov na prevádzkové parametre optického spoja. Následne, pomocou nástrojov elektromagnetickej teórie svetla, boli odvodené štyri výrazy (dva presné a dva aproximatívne) popisujúce geometrický útlm optického spoja. Zároveň boli skúmané tri rôzne prípady odsmerovania zväzku - priečne posunutie a uhlové odsmerovanie vysielača, resp. prijímača. Bol odvodený výraz, ktorý tieto prípady kvantifikuje ako útlm elipticky symetrického Gausovského zväzku. Všetky vyššie uvedené modely boli overené v laboratórnych podmienkach, aby sa vylúčil vplyv iných javov. Nakoniec práca pojednáva o návrhu plne fotonického optického terminálu. Najprv bol ukázaný návrh optického vysielača nasledovaný vývojom optomechanickej sústavy prijímača. Pomocou nástrojov geometrickej a maticovej optiky boli vypočítané parametre spoja a odhad tolerancie pri zamierení spoja.

## **KLÍČOVÁ SLOVA**

Optický bezdrôtový spoj, Fresnelova difrakcia, geometrický útlm, chyba zamierením, návrh plne optického spoja.

POLIAK, Juraj *Diffraction effects in transmitted optical beam*: doctoral thesis. Brno: Brno University of Technology, Faculty of Electrical Engineering and Communication, Department of Radio Electronics, 2014. 113 p. Supervised by prof. Ing. Otakar Wilfert, CSc.

## DECLARATION

I declare that I have written my doctoral thesis on the theme of “Diffraction effects in transmitted optical beam” independently, under the guidance of the doctoral thesis supervisor and using the technical literature and other sources of information which are all quoted in the thesis and detailed in the list of literature at the end of the thesis.

As the author of the doctoral thesis I furthermore declare that, as regards the creation of this doctoral thesis, I have not infringed any copyright. In particular, I have not unlawfully encroached on anyone’s personal and/or ownership rights and I am fully aware of the consequences in the case of breaking Regulation § 11 and the following of the Copyright Act No 121/2000 Sb., and of the rights related to intellectual property right and changes in some Acts (Intellectual Property Act) and formulated in later regulations, inclusive of the possible consequences resulting from the provisions of Criminal Act No 40/2009 Sb., Section 2, Head VI, Part 4.

Brno .....

.....

(author’s signature)

## ACKNOWLEDGEMENT

I would like to express the deepest appreciation to my Professor Otokar Wilfert, who was great mentor in my countless queries. Without his guidance and persistent help this dissertation would not have been possible.

I would like to thank to Professor Zdeněk Kolka, who provided me not only a unique opportunity and free hand during development and testing of the optical and optomechanical parts of the photonic FSO link, but also financial support without which this would not have been possible.

In addition, many thanks to Professor Jiří Komrška, who introduced me to the beauty of Wave Optics and mainly to the theory of diffraction, and whose enthusiasm and physicist's point-of-view were a motor in the theoretical part of the research. A big thank you to Professor Erich Leitgeb whose guidance and nice words came always at the perfect time for encouragement, professional and personal advices as well as for the introduction (not only) to the European OWC community. I would also like to thank to the OptaBro team, Department of Radio Electronics and to SIX Research Centre for their financial and personal support granted through my doctoral studies.

Last, but not least, I would like to thank to my family and to my life partner Lucia for their continuous support during my studies and for always believing in me.

Brno .....

.....

(author's signature)



Faculty of Electrical Engineering  
and Communication  
Brno University of Technology  
Technická 12, CZ-61600 Brno  
Czech Republic  
<http://www.six.feec.vutbr.cz>

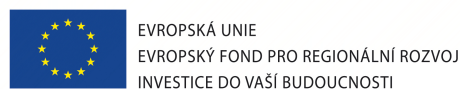
## ACKNOWLEDGEMENT

Výzkum popísaný v tejto doktorskej práci bol realizovaný v laboratóriách podporených z projektu SIX; registračné číslo CZ.1.05/2.1.00/03.0072, operační program Výzkum a vývoj pro inovace.

Brno .....

.....

(author's signature)



# CONTENTS

<b>Introduction</b>	<b>14</b>
<b>1 State of the art</b>	<b>16</b>
1.1 Optical wireless communications . . . . .	16
1.2 Atmospheric effects in FSO systems . . . . .	16
1.3 Deterministic effects in FSO systems . . . . .	21
1.3.1 Thermal and wind effects . . . . .	22
1.3.2 Geometrical loss . . . . .	22
1.3.3 Diffraction effects . . . . .	23
<b>2 Objectives of the thesis</b>	<b>25</b>
<b>3 Wave effects in OWC</b>	<b>26</b>
3.1 Gaussian beam . . . . .	26
3.2 Fresnel diffraction integral . . . . .	31
3.3 Fresnel diffraction in form of integration of Bessel functions . . . . .	36
3.4 Fresnel diffraction in form of FFT . . . . .	38
3.5 Diffraction effect assessment . . . . .	39
3.5.1 Experimental verification of models . . . . .	39
3.5.2 Model based on the Bessel functions integration . . . . .	41
3.5.3 Model based on the FFT . . . . .	43
3.6 Summary . . . . .	44
<b>4 Geometrical and pointing loss</b>	<b>49</b>
4.1 Derivation of exact expressions . . . . .	50
4.2 Derivation of approximative expressions . . . . .	54
4.3 Misalignment loss . . . . .	58
4.4 Experimental Verification and Discussion . . . . .	62
4.5 Summary . . . . .	69
<b>5 All-optical FSO transceiver</b>	<b>71</b>
5.1 Dual-wavelength single-aperture transmitter . . . . .	71
5.1.1 WDM-based DAS . . . . .	72
5.1.2 POF-based DAS . . . . .	73
5.1.3 Dual-core fibre-based DAS . . . . .	75
5.2 All-optical receiver: optomechanical design . . . . .	78
5.2.1 Telescope selection . . . . .	78
5.2.2 Fibre-coupling elements . . . . .	79

5.2.3	Final RX OMA design . . . . .	80
5.2.4	OMA alignment tolerances . . . . .	81
5.3	Non-standard atmospheric effects . . . . .	84
5.4	Summary . . . . .	87
<b>6</b>	<b>Conclusion</b>	<b>89</b>
	<b>Bibliography</b>	<b>91</b>
	<b>List of symbols, physical constants and abbreviations</b>	<b>98</b>
	<b>List of appendices</b>	<b>105</b>
<b>A</b>	<b>Sheet specifications of used components</b>	<b>106</b>
	<b>Curriculum Vitae</b>	<b>110</b>
	<b>List of Publications</b>	<b>112</b>

# LIST OF FIGURES

1.1	Atmospheric transmittance based on absorption analysis using LOW-TRAN. A zenith path from 0 km to 120 km altitude as well as the midlatitude summer atmospheric model are assumed. Atmospheric transmission windows are highlighted in grey color [3]. . . . .	18
1.2	Schematic of dual-wavelength FSO system . . . . .	21
1.3	Realisation of the dual-wavelength testing FSO transmitter at the Department of Radio Electronics, Brno University of Technology. . .	21
1.4	Experimental observation of the Fresnel diffraction in the planar optical beam transmission. Wavelength $\lambda = 632.8$ nm, TXA radius $r_{\text{TXA}} = 4.0$ mm, beam radius in the TXA plane $w_{\text{TXA}} = 14$ mm, distance $L = 6.32$ mm, which corresponds to the number $N_f$ of observable Fresnel zones at the distance $L N_f = 4$ . . . . .	24
3.1	Evolution of the beam widths $w_x(z)$ and $w_y(z)$ (a) and evolution of the beam radii $R_x(z)$ and $R_y(z)$ (b) along the $z$ axis, where negative and positive values represent a converging and a diverging wave, respectively. $z = 0$ corresponds to the location of beam waist. Simulation parameters: $w_{0x} = 0.1$ mm, $w_{0y} = 0.25$ mm, $\lambda = 633$ nm, distance $\Delta_z$ between both beam waists was 360 mm due to astigmatism.	30
3.2	To the explanation of Huygens-Fresnel principle in Cartesian coordinates. . . . .	32
3.3	To the derivation of the Fresnel zone diameter $r_n$ [25]. $M_0$ is point in the plane $\Sigma_{\text{TXA}}$ and $P$ point in the plane $\Sigma_{\text{RXA}}$ . . . . .	34
3.4	To the explanation of Huygens-Fresnel principle in cylindrical coordinates. . . . .	37
3.5	Simulation of Fresnel diffraction effect in FSO systems. Top left - primary elliptical Gaussian beam with beam-widths $w_x = 1.72$ mm and $w_y = 0.48$ mm in $x$ and $y$ axis, respectively. Top right - circular aperture (TXA) with radius $r_{\text{TXA}} = 1$ mm. Central plot shows the diffracted beam in the plane of observation $r_{\text{RXA}}$ and bottom left and right - optical intensity of the diffracted beam along $x$ and $y$ axis, respectively. In the bottom left section, power $P_{\text{out}}$ transmitted through the circular aperture is calculated relative to the total radiated power $P_{\text{in}}$ of the optical source. . . . .	40

3.6	Measured data ( $\times$ ) is in very good agreement with the model based on the integration of the Bessel function (3.44) ( $*$ ) and FFT-based model (3.29) ( $\diamond$ ). Parameters of the experiment and simulations: Wavelength $\lambda = 543.5$ nm, transmitter aperture $r_{\text{TXA}} = 4$ mm, distance $z$ to the observation plane $\Sigma_{\text{RXA}}$ $z = 7.36$ m, which corresponds to the number of observed Fresnel zones $N_f = 4$ and assuming a collimated circular Gaussian beam with beam half-width $w = 14$ mm. Measurement error was estimated as $\delta_e = 7.95\%$ . . . . .	41
3.7	a) Intensity distribution calculated using the method of integration of the Bessel functions as a function of both radial and axial distance from the aperture in the units of the aperture radius $r_{\text{TXA}}$ according to (3.44). b) Calculated intensity distributions using the complete Rayleigh-Sommerfeld model [38]. Simulation parameters: $\lambda = 10.6$ $\mu\text{m}$ and $r_{\text{TXA}} = 0.1$ mm. The boundary between near field and far field is located around $z \approx 9.4 \cdot r_{\text{TXA}}$ . . . . .	46
3.8	Transverse optical intensity distributions at various distances. Extremes of the functions are highlighted: maxima(o) and minima(x). Individual plots are related to cross-sections in Fig.3.7 at various distances $z$ corresponding to various Fresnel numbers $N_f$ . Top to bottom: $N_f$ changes from 1 to 3 with step 0.5, which corresponds to distances $z_1 = 9.4340 \cdot r_{\text{TXA}}$ , $z_{1.5} = 6.29 \cdot r_{\text{TXA}}$ , $z_2 = 4.72 \cdot r_{\text{TXA}}$ , $z_{2.5} = 3.77 \cdot r_{\text{TXA}}$ and $z_3 = 3.14 \cdot r_{\text{TXA}}$ . . . . .	47
3.9	Contrast of the central region of the diffraction pattern as a function of the number of transmitted Fresnel zones $N_f$ . Shown are only the results in near-field zone where contrast is relevant, i.e. for $N_f > 1$ . Contrast minima occur when $N_f \approx n + 1/2$ , $n \in N$ , whereas maximal contrast occurs when $N_f$ is a whole number $N$ . . . . .	48
4.1	To the explanation of geometrical attenuation loss. . . . .	49
4.2	Experimental setup of the geometrical attenuation measurement used to verify validity of Eq.(4.12) and Eq.(4.18). LD - laser diode with wavelength $\lambda = 650$ nm, mW - optical power meter. Distance $z$ between the laser diode and Iris diaphragm was $z = 0.2$ m, where beam half-widths where $w_x = 1.72$ mm and $w_y = 0.48$ mm and axial optical intensity $I(0, 0, z) = 2583$ W/m <sup>2</sup> . Diaphragm diameter $2r_{\text{RXA}}$ was calibrated and adjustable in range $2r_{\text{RXA}} \in < 0.5; 5 >$ mm with 0.5 mm step. . . . .	54

4.3	Comparison of the measured optical power $P_{\text{det}}$ transmitted through a circular iris diaphragm with diameter $2r_{\text{RXA}}$ with the simulated power $P_{\text{sim}}$ according to Eq.(4.11) and Eq. (4.15). Distance $z$ between the laser diode and iris diaphragm was $z = 0.2$ m, where beam half-widths where $w_x = 1.72$ mm and $w_y = 0.48$ mm and axial optical intensity $I(0, 0, z) = 2583$ W/m <sup>2</sup> . Diaphragm diameter $2r_{\text{RXA}}$ was calibrated and adjustable in range $2r_{\text{RXA}} \in < 0.5; 5 >$ mm with 0.5 mm step. Measurement error $P_{\text{err}} = 10\%$ for $2r_{\text{RXA}} \leq 2.0$ mm and $P_{\text{err}} = 2\%$ otherwise. . . . .	55
4.4	Comparison of the precise value of modified Bessel function $I_0$ calculated by MATLAB and its approximation given by two, three and four terms of eq.(4.19). . . . .	56
4.5	Asymptotic approximation of modified Bessel function $I_0$ according to Eq. (4.20). . . . .	57
4.6	To the explanation of lateral misalignment loss. $\Delta$ represents the lateral misalignment and $\theta$ and $\theta_{\text{FOV}}$ stand for the divergence of the transmitter and field-of-view of the receiver, respectively. . . . .	59
4.7	To the explanation of angular misalignment attenuation loss. $\gamma_t$ represents the angular misalignment of the transmitter and $\theta$ and $\theta_{\text{FOV}}$ stand for the divergence of the transmitter and FOV of the receiver, respectively. . . . .	60
4.8	Front view of the misaligned elliptical beam in the receiver plane $\Sigma_{\text{RXA}}$ . $\Delta_x$ and $\Delta_y$ are displacements and $w_y$ are the beam-widths in $x$ and $y$ axis, respectively, and $r_{\text{RXA}}$ is the aperture radius of the receiver RX. . . . .	62
4.9	To the explanation of RXA angular misalignment loss (pointing error). $\gamma_r$ represents the angular misalignment of the transmitter and $\theta$ and FOV stand for the divergence of the transmitter and field-of-view of the receiver, respectively. . . . .	63
4.10	Comparison of the measured geometrical attenuation of the beam at various distances between TXA and RXA and simulation according to (4.25). $\theta = 0.2$ rad, $r_{\text{RXA}} = 31.25$ $\mu\text{m}$ . . . . .	64
4.11	Comparison of the measured lateral misalignment and geometrical attenuation of the beam at $z = 5$ mm for various lateral displacement $\Delta$ and simulation according to (4.32). $\theta = 0.2$ rad, $r_{\text{RXA}} = 31.25$ $\mu\text{m}$ . Estimation assumes constant intensity distribution over RXA, whereas simulation takes into account Gaussian distribution of the optical intensity. Due to relatively large ratio $w/r_{\text{RXA}}$ , the estimation and simulation results overlap. . . . .	65

4.12	Geometrical and lateral misalignment attenuation measured along the minor optical beam axis (x points) compared to the results of Eq.(4.37) (solid line). Simulation parameters: $r_{\text{RXA}} = 0.25$ mm, $w_x = 9.6$ mm, $w_y = 32$ mm. . . . .	66
4.13	Absolute difference between attenuation measured along the minor optical beam axis (Fig.4.12) and the results of Eq.(4.37). Simulation parameters: $r_{\text{RXA}} = 0.25$ mm, $w_x = 9.6$ mm, $w_y = 32$ mm. . . . .	66
4.14	Geometrical and lateral misalignment attenuation measured along the major optical beam axis (x points) compared to the results of Eq.(4.37) (solid line). Simulation parameters: $r_{\text{RXA}} = 0.5$ mm, $w_x = 6$ mm, $w_y = 20$ mm. . . . .	67
4.15	Absolute difference (error) between attenuation measured along the major optical beam axis (Fig.4.14) and the results of Eq.(4.37). Simulation parameters: $r_{\text{RXA}} = 0.5$ mm, $w_x = 6$ mm, $w_y = 20$ mm. . . . .	67
4.16	Lateral misalignment attenuation as a function of lateral misalignment $\Delta$ for various link distances $L$ assuming constant circular Gaussian beam divergence angle $\theta = 2^\circ$ and receiver radius $r_{\text{RXA}} = 1$ mm. . . . .	68
4.17	Angular misalignment (pointing error) attenuation as a function of transmitter tilt $\gamma_t$ assuming various Gaussian beam divergence angles $\theta$ at constant link distance $L = 2$ m and receiver radius $r_{\text{RXA}} = 1$ mm. . . . .	69
5.1	Dual-wavelength all-optical single-aperture transmitter. LD – laser diode, OI – optical isolator. Detailed specifications are shown in Chapter A. . . . .	73
5.2	Optical intensity distribution at the end of POF excited by laser diode with $\lambda = 850$ nm. Cross-sections of the beam pattern, shown in the right and lower part of the figure, demonstrate the “quasi-Top-Hat” pattern. . . . .	74
5.3	Prototype of the testing FSO link transmitter using the fibre WDM and POF final fibre. Two laser sources (1550 nm on the top and 850 nm on the bottom) are connected via optical isolators (OI) to the inputs of WDM. WDM output is coupled using POF to the collimating lens (TXA) from which both beams are transmitted to the free-space. The three yellow fibres are fibre patch cables, which solve the connector compatibility problem. They are equipped with FC/PC connector on one side and FC/APC on the other side. . . . .	75
5.4	Cross-section of the dual core OF. Distance between centre of the cores is $125\mu\text{m}$ . Not to scale. . . . .	76

5.5	Schematics of the dual-wavelength all-optical single-aperture (DAS) FSO transmitter. Two external inputs and two internal laser diodes (LD) with optical isolator (OI) are in each branch of SM fibre coupler connected to the respective input of a dual-core (DC) final fibre. Output optical beam emerging from the output of the final fibre is coupled to the free-space by the plano-convex lens (TXA) with focal length $f_{\text{TXA}}$ . Light gray colour indicates SM OF SM800-5.6-125 for 850 nm, black colour indicates SM OF SM980-5.8-125 for 1550 nm and dark gray colour represents the DC OF. Unless otherwise stated, all optical connectors are FC/APC type. . . . .	77
5.6	Schematic representation of the optical ray propagation in a GRIN lens exactly one “pitch” $p$ long [62] and the definition of the pitch $p$ . .	80
5.7	Schematics of the proposed OMA RX design. $D_{\text{RXA}}$ and $D_{\text{A}}$ stand for the Keplerian telescope diameter and the beam diameter at the output of the asphere, respectively, $f_{\text{tel}}$ and $f_{\text{A}}$ stand for the telescope and collimating asphere diameter, respectively, $o_{\text{RXA}}$ represents the OMA optical axis. Not to scale. . . . .	80
5.8	Schematic representation of the angular alignment tolerance $\alpha_{\text{tol}}$ of the proposed receiver. $r_i$ and $\theta_i$ represent the ray lateral and angular displacement, respectively, in the plane of the telescope input, $r_o$ and $\theta_o$ represent the ray lateral and angular displacement, respectively, in the plane of the GRIN input aperture, $M_1$ , $M_2$ , $M_3$ and $M_4$ represent matrices of the telescope, space between telescope and asphere, aspheric lens and space between asphere and GRIN lens. Not to scale.	83
5.9	Wind-related FSO link availability estimation model. . . . .	86

# LIST OF TABLES

4.1	Comparison of the measured optical power $P_{\text{det}}$ transmitted through a circular iris diaphragm with diameter $2r_{\text{RXA}}$ (experimental setup is shown in Fig.4.2) with the simulated optical power $P_{\text{sim}}$ according to Eq.(4.11) and Eq.(4.15) and experimental setup in Fig.4.2. Measurement error $P_{\text{err}} = 10\%$ for $2r_{\text{RXA}} \leq 2.0$ mm and $P_{\text{err}} = 2\%$ otherwise. . . . .	54
4.2	Maximal range of argument $z$ in Eq. (4.19) achievable for different number of approximation terms to maintain uncertainty below 1%. . .	56
5.1	Specifications of the all-optical RX design. . . . .	82
A.1	Sheet specifications of 850 nm LD. . . . .	106
A.2	Sheet specifications of 1550 nm LD. . . . .	106
A.3	Sheet specifications of SM800-5.6-125 fibre. . . . .	106
A.4	Sheet specifications of SM980-5.8-125 fibre. . . . .	107
A.5	Sheet specifications of SMF-28e+ fibre. . . . .	107
A.6	Sheet specifications of IO-F-850APC optical isolator. . . . .	108
A.7	Sheet specifications of IO-H-1550APC optical isolator. . . . .	108
A.8	Sheet specifications of fibre-optic WDM. . . . .	109

# INTRODUCTION

“If you would be a real seeker after truth, it is necessary that at least once in your life you doubt, as far as possible, all things.” – René Descartes

Wireless optical signal transmission has many applications in communications nowadays – point-to-point connection (buildings, satellites), indoor communications inside buildings or public transport (Li-Fi as an alternative to Wi-Fi [1]) up to experimental applications (UV non-line-of-sight (NLOS) communications). The main advantage of using optical links, in comparison with RF (radio frequency) technology [2], is their non-licensed operation, significantly greater usable bandwidth, immunity against other EM sources [3] and last, but not least, high power efficiency and low weight, which makes them optimal for using in mobile and satellite communications.

Free-space optical (FSO, or optical wireless communication – OWC) links, which are of the main interest of the thesis, exploit the atmosphere as the transmission environment. In comparison with RF or MMW (millimetre wave) technology, the FSO links achieve much larger antenna gain and therefore it is possible to use beam with a very low divergence, which is in practice only a few milirads (terrestrial FSO links) down to a fraction of milirads (satellite communications)[4].

However, these advantages are often deteriorated by effects which give rise to some phenomena. FSO links performance is highly sensitive to outside atmospheric conditions. Another issue is also so far relatively low level of practical and theoretical experience with wireless optical links which have been studied mainly for last 30 years (whereas RF communications have already more than a century of development). This is linked with an insufficient or even a lack of a thorough analysis of many optical wave or geometrical effects, which are common in OWC systems. This often leads to omission of such effects during the phase of FSO link design. This is mainly caused by the fact that the main focus was so far to understand the optical properties of atmosphere and its influence on the optical wave. The shift of the focus of interest towards more advanced optical effects in OWC systems is mainly due to recent development in the photonics (more powerful optical sources), communication techniques (sophisticated modulations and codings) and optics (more advanced optical parts). This shift is also reflected in the thesis and is summarised by effects which are random, often omitted and non-standard.

The thesis then deals mainly with the geometrical effects caused by the restriction of the optical beam by an optical system (i.e. restriction of a generally elliptical optical beam by a circular lens socket or transmitter aperture). The restriction then gives rise to the diffraction (wave effect) and attenuation (geometrical effect). Other non-standard effects are then introduced and studied – influence of the wind on the FSO link mechanics and building sway; influence of the rain drops on the FSO

transceiver aperture. Direct effects are here effects which have a direct influence on the FSO transceiver and indirect effects mainly influence the optical beam itself in the atmospheric transmission media [5]. This point of view changes the understanding of the optical links as solely communication devices to sensoric devices.

Author of the dissertation has set goals of his work to study, analyse and understand obstacles and restrictions which are to be faced in OWC systems and to quantify and model them. Based on the outcomes of the analyses, possible solutions how to reduce if not even eliminate the mentioned drawbacks.

During the times when the author was conducting his research he struggled between theoretical principles of pure mathematics, beauty of physics and practical reasons of engineering. This challenge however has provided a unique point-of-view as an intersection of all three sets of fields.

# 1 STATE OF THE ART

## 1.1 Optical wireless communications

Free-space optical (FSO) links are used for optical signal transmission between a transmitter TX and a receiver RX in the atmospheric transmission media, mostly in troposphere. The optical beam between two FSO terminals propagates, in general, in a non-stationary and inhomogeneous atmospheric media. Maintaining the line-of-sight (LOS) between the terminals signal propagates over several hundreds of metres for terrestrial FSO links, up to thousands of kilometres for satellite links [6] or deep-space links [7]. In order to maintain a stable, reliable link connection with high availability, optimisation in terms of the deterministic parameters of the transceiver with respect to the statistical parameters of the link location are needed.

FSO links are evaluated according to their availability and reliability. Availability is mostly influenced by the instantaneous state of the atmosphere [8, 9] causing extinction, turbulent effects due to refractive index fluctuation in the atmosphere and by noise in general (background noise, thermal noise etc.). Lately, term "non-standard" effects began to be discussed. These effects cover not only atmospheric, but also wave and geometrical effects which are often hard to define quantitatively and which cause either the beam shape distortion or deteriorate the optical power measurements in testing FSO links.

Reliability of the link is determined not only by transceiver parameters, e.g. link margin, beam divergence, receiver aperture diameter, modulation and coding scheme, but also by its internal structure (heating, shading) and by its design and shape (due to aerodynamics). While the first set of parameters is well described in the literature, the internal structure and overall terminal design are taken for granted and are more subject to personal taste. The thesis analyses and models the design of internal and overall transceiver characteristics in terms of the non-standard effects in order to minimise spurious effects and maximise overall link reliability and availability.

## 1.2 Atmospheric effects in FSO systems

As the optical beam propagates in the atmosphere, it experiences loss due to attenuation of the optical power, random fluctuations of the optical power due to turbulence [10] and dispersion due to scattering on the air particles, which results in multipath beam propagation.

Attenuation loss in the atmosphere is caused by absorption and scattering of the optical beam on molecules and aerosols. Quantitatively is this phenomenon

described by Beer's (or Beer-Lambert's or Beer-Lambert-Bouguer's) law [8], which defines extinction coefficient  $\gamma$  in terms of the ratio between the initial optical intensity  $I(\lambda, 0)$  and the optical intensity  $I(\lambda, L)$  at the distance  $L$  as

$$\frac{I(\lambda, L)}{I(\lambda, 0)} = \exp[-\gamma(\lambda)L], \quad (1.1)$$

where  $I(\lambda, L)$  stands for the optical power at distance  $L$  from the transmitter,  $P(\lambda, 0)$  for the total optical transmitted power and  $\gamma(\lambda)$  for the extinction coefficient which includes effects of absorption and scattering (dimensionally  $\text{km}^{-1}$ ).

There are several forms of extinction effects divided according to the relative size of the atmospheric particles and wavelength and the extinction coefficient  $\gamma$  is sum of the absorption coefficient  $\alpha$  and scattering coefficient  $\beta$ . Moreover, both scattering and absorption coefficients may be influenced by both aerosol and molecular constituents in the atmosphere [10]. Extinction coefficient is then given as the sum

$$\gamma = \alpha_m + \alpha_a + \beta_m + \beta_a. \quad (1.2)$$

Atmospheric environment consists of molecules of oxygen, nitrogen and water, which are all responsible mainly for the attenuation of the optical power even in case of ideally clear atmosphere and give rise to the attenuation of a clear atmosphere  $\tilde{\alpha}_{\text{atm}}$  [11]. This additional attenuation is strongly wavelength dependent. Spectral regions of a minimal or negligible attenuation, so called atmospheric windows, may be used for FSO link operation and are shown in Fig.1.1. The most significant atmospheric windows are regions of 850 nm, 1064 nm, 1550 nm and 10.6  $\mu\text{m}$ . Each of the given regions has an advantage based on the technological development and atmospheric spectral properties. Whereas the region at 10.6  $\mu\text{m}$  has very low attenuation at the price of high costs, the region at 1550 nm is widely used in telecommunications and therefore offers commercially available components and the region 850 nm is relatively affordable.

Dominant effect responsible for the optical beam attenuation is Mie scattering<sup>1</sup> on aerosols, mainly on water drops of fog [4]. Dependency of Mie scattering coefficient  $\beta_a$  on the meteorological visibility  $V$  according to [ITU-R P.1817: Propagation data required for the design of terrestrial free-space optical links] is:

$$\beta_a = \frac{3.912}{V} \left( \frac{\lambda}{550 \text{ nm}} \right)^{-q}, \quad [\text{km}^{-1}; \text{km}, \text{nm}] \quad (1.3)$$

where parameter  $q$  in is defined in ITU-R P.1814 according to Kruse model [12] as

---

<sup>1</sup>Mie scattering is also responsible for the white colour of clouds.

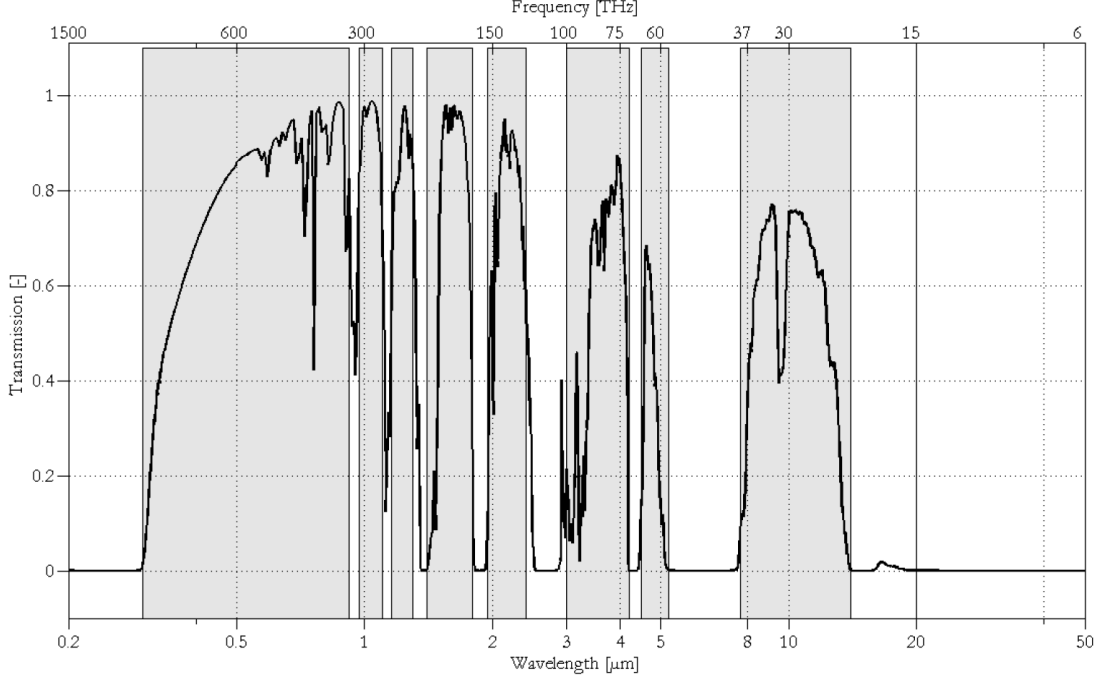


Fig. 1.1: Atmospheric transmittance based on absorption analysis using LOW-TRAN. A zenith path from 0 km to 120 km altitude as well as the midlatitude summer atmospheric model are assumed. Atmospheric transmission windows are highlighted in grey color [3].

$$q = \begin{cases} 1.6 & \text{for clear atmosphere } V > 50 \text{ km} \\ 1.3 & \text{for } 6 \text{ km} < V < 50 \text{ km} \\ 0.585 \cdot V^{1/3} & \text{for } V < 6 \text{ km.} \end{cases} \quad (1.4)$$

Based on the Kruse model, Kim model [13] later on specified parameter  $q$  for the visibility  $V$  smaller than 6 km as

$$q = \begin{cases} 0.16V + 0.34 & \text{for haze } 1 \text{ km} < V < 6 \text{ km} \\ V - 0.5 & \text{for mist } 500 \text{ m} < V < 1 \text{ km} \\ 0 & \text{for fog } V < 500 \text{ m.} \end{cases} \quad (1.5)$$

Molecular (Rayleigh<sup>2</sup>) scattering represented by scattering coefficient  $\beta_m$  with a strong spectral dependency with a term  $C_R$  depending on the different particle cross sections and concentrations and is nearly negligible in infra-red region

$$\beta_m(\lambda) = \frac{C_R}{\lambda^4}. \quad (1.6)$$

---

<sup>2</sup>Rayleigh scattering gives rise to the blue colour of the sky.

On the other hand, Rayleigh scattering gives rise to a whole new field of OWC applications in non-line of sight (NLOS) scenarios using ultraviolet (UV) radiation.

Geometrical attenuation loss is caused by the attenuation and scattering on rain drops and snow flakes. Attenuation coefficient  $\alpha_{\text{rain}}$  and  $\alpha_{\text{snow}}$  of the optical signal due to rain and snow depend on the rain rate  $R$  and the snow rate  $S$  (both dimensionally mm/h) and according to the ITU-R P.1817 are expressed as

$$\alpha_{\text{rain}} = 1.076 \cdot R^{0.67}, [\text{dB/km}] \quad (1.7)$$

and

$$\alpha_{\text{snow}} = \begin{cases} 0.0001023 \cdot \lambda_{\text{nm}} + 3.7855466 \cdot S^{0.72} & \text{for wet snow,} \\ 0.0000542 \cdot \lambda_{\text{nm}} + 3.4958776 \cdot S^{1.38} & \text{for dry snow, [dB/km]} \end{cases} \quad (1.8)$$

respectively.

A different approach of FSO link availability estimation is used when satellite optical links (mainly on GEO and LEO orbits) are considered. There, unlike in terrestrial communications, high elevation angle and small beam divergence require beam steering and tracking to maintain the connection. The availability of such link is mainly limited by the statistical probability of cloud occurrence in the optical beam propagation path. This is mainly due to relatively large attenuation and thickness of clouds. Therefore, special attention is required when considering the optical ground station (OGS) location. Not only a low individual cloud occurrence at the OGS location is required, but also a low cross-correlation of the cloud occurrence between OGSs [14].

In FSO links in general, there is a technology shift in last years with the transceivers being equipped with optical fibre technology, which gives rise to fully photonic FSO links discussed also later in the thesis. In photonic links, optical fibre is used as the primary optical source in the transmitter. On the other hand, in the receiver, the optical beam is coupled directly to the optical fibre. This allows for much higher flexibility in the system design at the cost of much higher complexity. The crucial point is the optical beam reception from free-space with a receiving aperture diameter of several centimetres (or tens of centimetres) to the optical fibre core of several microns. High optical gain to be achieved causes a relatively narrow field of view (FOV), which gives rise to pointing errors. Lately, several design possibilities have been tested and presented worldwide. While Parca et al. [15] used a relatively simple approach combining a plano-convex lens and a GRIN-pigtailed fibre, Boroson et. al in [16] describe the Lunar Lasercom Space Terminal (LLST), where Cassegrain-Schmidt optical system have been used. While the first mentioned system is considered to be unreliable over larger distances in turbulent environment,

the latter is optimal, but would require investments too high for practical implementation in terrestrial FSO systems. Therefore, one of the goals of the dissertation has been set to analyse and to optimise FSO terminal design with respect to its optical and optomechanical structure, reliability and cost.

Lately, there is a shift in focus from extending the range of FSO links towards increasing reliability and availability of OWC. This topic has been widely discussed also at COST Action IC1101 where the author is an active participant. Many teams, not only from Europe, study the influence of the frost or raindrops on cover windows of FSO links on the fluctuation and attenuation of the measured optical power. This gives rise to misinterpretation of measured results. There is an increasing number of publications on the impact of the rain [17] or of the wind direction and speed [18] on testing FSO link attenuation. However, the lack of quantitative analysis, which may determine the impact of these phenomena on FSO link from meteorological statistics at given location, make them unsuitable to define requirements on the covers, mechanical stability or beam divergence in order to obtain reliable data. Therefore, one of the aims of the dissertation will be the quantitative analysis of the direct influence of the rain and wind on the testing FSO links, both of which give rise to inaccurate or deteriorated measurements of the optical beam attenuation in the atmosphere depending on the current state of the atmosphere (visibility, rain rate, etc.).

The rain influence on the optical signal propagation through the atmosphere is well described and documented. In real scenario, however, due to inappropriate terminal design (undersized cover length) or due to high elevation of the link, rain drops may fall on the transparent window cover of the terminal. These rain drops then work as microlenses, which may scatter portions of the optical beam outside the desired path causing random attenuation and received optical power fluctuations. This may be misinterpreted as a direct impact of the rain on the transmitted beam itself in the atmosphere and lead to false conclusions.

Equally important is to take into account influence of the wind on the mechanical stability of the terminal based on the meteorological statistics at the given location [18]. Not only random building sway but also terminal vibrations may cause received optical power fluctuation and attenuation. There is a lack of publications on the quantitative analysis of the optical beam misalignment in FSO links caused by direct wind influence. This might give rise to requirements regarding mechanical stability and design of FSO link terminals.

Testing FSO links serve to study spectral dependency of the atmospheric conditions on the optical beam attenuation and scintillation. For this purpose, so called dual testing FSO links have been developed [19] consisting of two separate terminals operating at different wavelengths (commonly 850 nm and 1550 nm). The current

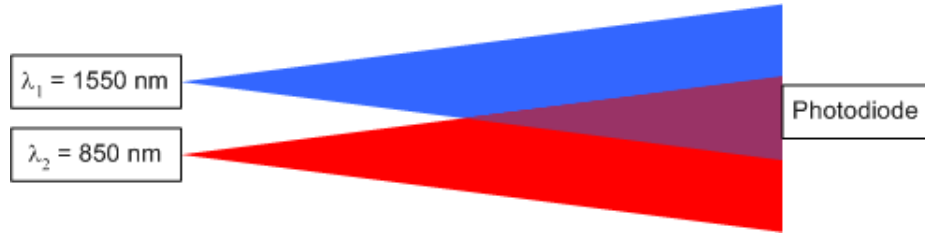


Fig. 1.2: Schematic of dual-wavelength FSO system

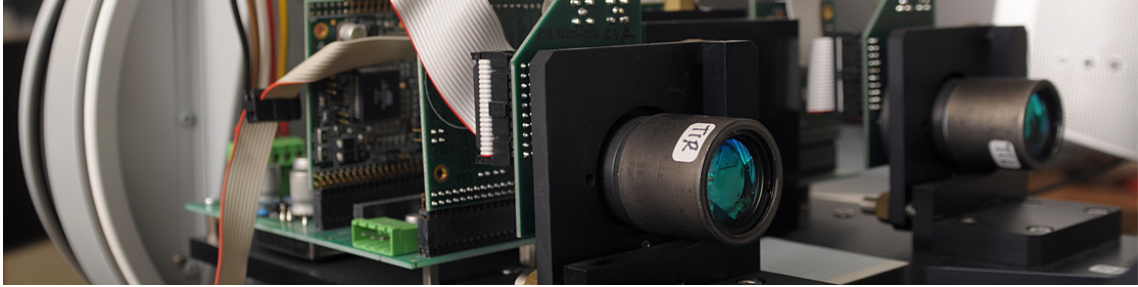


Fig. 1.3: Realisation of the dual-wavelength testing FSO transmitter at the Department of Radio Electronics, Brno University of Technology.

dual testing FSO link design is extremely sensitive to misalignments and a small thermal variation induces additional attenuation which might be misinterpreted as the impact of the measured atmospheric condition in the affected testing channel. This may lead to false conclusion that the operating wavelength is unsuitable for use in OWC.

There are some restrictions when two individual transmitters are used in case of transversally inhomogeneous fog event. Then, each of the optical beams is influenced in a different amount which leads again to misinterpretation of the measured data. Therefore, a thorough redesign of testing dual FSO links should be considered to merge both optical channels into a single optical channel. As will be shown in the thesis, this part is challenging not only practically but also theoretically.

### 1.3 Deterministic effects in FSO systems

This chapter deals with special (non-standard) effects, which are, however, not uncommon in FSO links. They have been called non-standard effects since their occurrence is highly random causing mainly attenuation and fluctuation of optical power and there is lack of thorough mathematical analysis of such effects. Many teams worldwide work on their identification and description (COST Action IC1101: <http://opticwise.uop.gr/>), which is a complex task since they rarely occur separately

from other effects.

### 1.3.1 Thermal and wind effects

The most common effect is attenuation, or fluctuation of received optical power, due to optical beam misalignment caused by temperature variation, sun radiation towards receiver (or transmitter) or by the wind (building sway, console vibrations) [11]. Elimination of these effects is difficult but can be predicted based on the meteorological statistics of the location. Then, right measures can be taken to minimise the vibrations by improving the console stability, or heuristically or analytically [20] determine possible degree of misalignment and increase the beam divergence.

However, by increasing the optical beam divergence, the optical power density at the receiver decreases which causes decrease of the received optical power and of the link margin in case of severe meteorological conditions. In practice, for terrestrial FSO systems operating with ranges of several hundreds of metres, it is optimal to choose beam divergence of 2 – 3 mrad. On the other hand, in case of satellite links, the beam divergence is lower by two degrees of magnitude. Generally, the optical beam spot at the receiving plane should be significantly larger than size of the receiver aperture (RXA).

### 1.3.2 Geometrical loss

Common practice is to estimate the misalignment error of FSO link (usually 1 – 3 dB). Taking into account the beam divergence, one may find the geometrical loss for circularly symmetrical beam [11]. Literature survey points out the lack of an exact model describing precisely the case of an elliptically symmetrical Gaussian beam which is generated by common semiconductor laser diodes (LD).

A solution actively sensing misalignments is to use an automatic pointing, acquisition and tracking (PAT) system. Using a beacon, the PAT system points the terminal towards a receiver with larger FOV than the communication link. This is carried out for both directions and after successful acquisition, the PAT system tracks small changes in terminal direction to maintain line-of-sight (LOS) a increase the system availability. System allows to decrease the divergence angle FOV to increase the range of such system or in mobile communications. Higher costs make such system mostly used for satellite communications.

To evaluate the system sensitivity to atmospheric and geometrical effects, one uses the FSO link budget. The result of the link budget analysis is the link margin  $M$  [4]. Its value defines the acceptable attenuation caused by atmospheric effects,

misalignments, aging or mechanical instability to achieve required FSO link reliability and availability. The percentage of time over a period when the link margin is larger than zero defines the link availability, which is a key design parameter and is given by the particular link application and nature of the transmitted signal.

Analysis of all individual effects gives rise to a complex model of optical wireless communications which quantifies with a given precision individual effects.

### 1.3.3 Diffraction effects

To study some particular properties of the interaction between matter and light (characterised by very short wavelengths), one must leave the purely geometrical model of the optical field propagation. Especially at the edges between an obstacle and the free space and in areas where large number of optical rays meet, one must consider the optical field no longer as a set of rays, but rather as a wave. The very first reference to the phenomena later known as diffraction was made by Leonardo da Vinci [21] in 15<sup>th</sup> century. However, first thorough investigation on this subject was brought later in 1665 by Grimaldi in a book published two years after his death [22]. The subject was later studied by Huygens, who was also the first proponent of the optical wave theory. His famous principle was supplemented by Fresnel in 1818 [23] to give rise to the famous Huygens-Fresnel principle. The first rigorous solution to diffraction problems was given by Sommerfeld no sooner than in 1896.<sup>3</sup>

Diffraction effects occur as a result of the light interaction with an obstacle of dimensions comparable with the wavelength of the impinging wave (e.g. slit or aperture) or at the boundary of the obstacle and free-space (e.g. half-plane). In FSO systems, the diffraction is usually considered as the broadening of the optical beam due to Fraunhofer diffraction on the circular lens socket with radius  $r_{\text{TXA}}$  inside the transmitter. However, when the receiver is positioned in the near-field zone of the wave we may witness the Fresnel diffraction pattern at plane of the receiver aperture RXA, which might have severe consequences. The Fresnel diffraction causes that the beam shadow behind the transmitter aperture to be blurred rather than sharp. However, unlike the Fraunhofer diffraction, Fresnel diffraction does not change the beam divergence. Although the Fresnel diffraction is more known and described in the fields of instrumentational optics and diffraction-based material structure analysis, one should always take it into account when working with optical beams in free-space optical links. Only very seldom and in a very limited number of scenarios we may neglect its effects. To quantitatively assess this phenomenon, proper understanding of the optical wave is essential.

---

<sup>3</sup>His exact solution of diffraction phenomena can be found in chapter XI in [21], but will not be discussed since in our case  $L \gg r_{\text{TXA}} \gg \lambda$ .

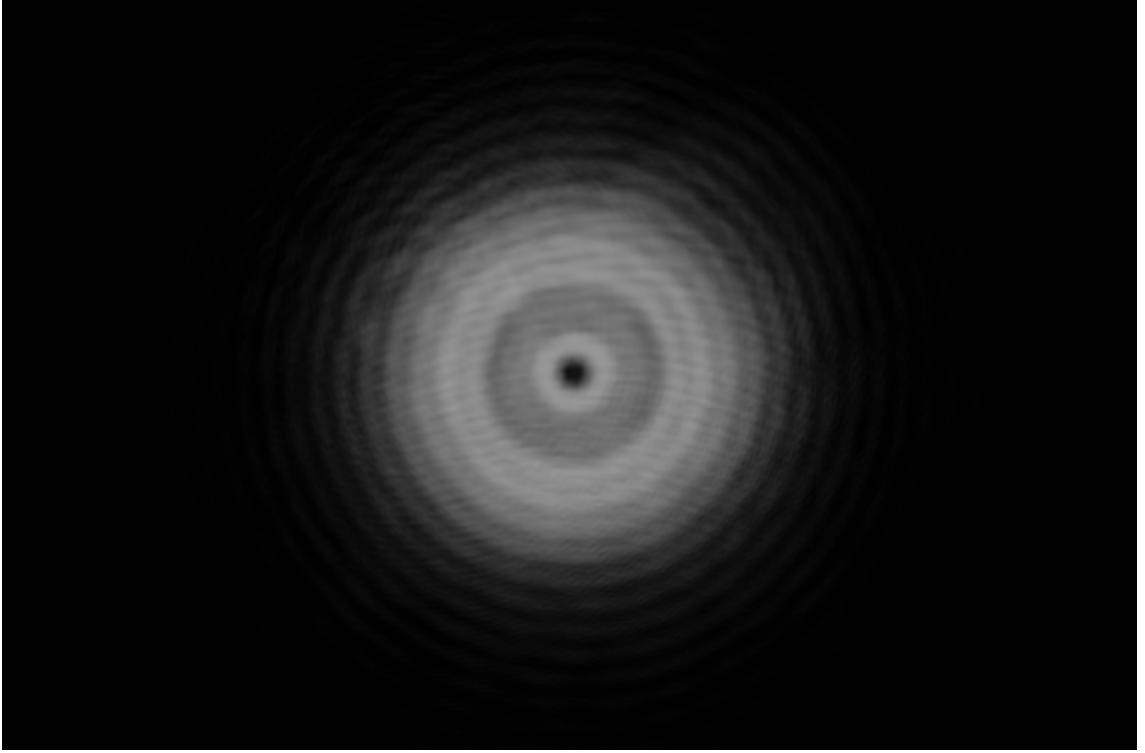


Fig. 1.4: Experimental observation of the Fresnel diffraction in the planar optical beam transmission. Wavelength  $\lambda = 632.8$  nm, TXA radius  $r_{\text{TXA}} = 4.0$  mm, beam radius in the TXA plane  $w_{\text{TXA}} = 14$  mm, distance  $L = 6.32$  mm, which corresponds to the number  $N_f$  of observable Fresnel zones at the distance  $L$   $N_f = 4$ .

Moreover, as is shown in Fig.1.4, the Fresnel diffraction pattern of an optical wave observed behind a circular aperture shows no longer a smooth exponential decline of the optical intensity from the beam centre towards its edges, but rather complicated structure with a number of maxima and minima. In the worst-case scenario, we might have the diameter of the central maximum larger than the diameter of the receiver aperture RXA. Then, when ideally aligned, the received optical power is zero. If, however, one aligns the FSO link in the direction of the first maximum, the atmospheric scintillation increases the variance of the received power. This is mainly due to very sharp and narrow distribution of the optical intensity at the first maximum. The thesis presents how to analyse the problem of Fresnel diffraction, quantitatively assess its influence on the particular FSO link performance and how to minimise its effects to a reasonable level.

## 2 OBJECTIVES OF THE THESIS

Based on the actual state-of-the-art in the field of OWC, following thesis objectives have been proposed:

- Develop analytical model of the diffraction of an elliptically symmetrical generally astigmatic Gaussian beam on a circularly symmetrical transmitter aperture
- Develop analytical model of the geometrical attenuation of an elliptical Gaussian beam restricted by a circular optical system
- Develop analytical model of the attenuation due to misalignment of an elliptical Gaussian beam
- Based on the synthesis of the preceding objectives, propose methods and terminal design improvements to increase reliability and availability of both testing and data FSO links

### 3 WAVE EFFECTS IN OWC

The optical radiation is an electromagnetic (EM) radiation covering ultraviolet (UV), visible (VIS) as well as infrared (IR) part of the spectra. The optics is part of the physics, which analyses properties of the optical radiation and its interaction with the matter, can be divided into four disciplines with increasing complexity; geometrical, electromagnetic, wave and quantum optics. In this chapter, using the apparatus of wave optics, properties of the elliptical Gaussian beam (GB) will be shown and two models of Fresnel diffraction of the elliptical GB on a circular lens socket will be derived.

#### 3.1 Gaussian beam

For the study of wave effects in FSO systems it is essential to precisely describe the transmitted optical wave. In order to do so, one must mathematically define wave function  $\psi_0$  in the transmitter plane (TXA). Optical wave incident on the TX lens is emitted from a radiating source (e.g. LED or laser). While most LEDs exhibit a Lambertian radiation pattern [11], light emitted from the laser is described by means of the Gaussian beam theory [24].

In OWC, a semiconductor laser diode is often used as the light source for its monochromaticity and a relatively large bandwidth (up to several GHz). Mathematical description of distribution of the optical intensity  $I(x, y, z)$  emitted from a laser source is based on the paraxial approximation of Helmholtz equation [21], which yields one of the possible solutions of this equation known as Gaussian beam.

Let's assume a harmonic monochromatic wave  $\psi(\mathbf{s}, t)$  propagating in a homogeneous, isotropic, non-dispersive and non-absorbing environment with no additional sources of electromagnetic (EM) radiation. At each point of the space, the wave  $\psi(\mathbf{s}, t)$  must satisfy homogeneous linear differential equation of a second order known as the homogeneous wave equation

$$\nabla^2\psi(\mathbf{s}, t) - \frac{1}{v^2} \frac{\partial^2\psi(\mathbf{s}, t)}{\partial t^2} = 0, \quad (3.1)$$

where  $\nabla$  is the derivation of a function according to each spatial variable,  $\mathbf{s}$  is the position vector of the point of observation  $P$  (cf. Fig.3.2 and Fig.3.4) and  $v$  is the phase velocity of the wave.

There are several wave functions known as solutions to the wave equation (3.1) (e.g. plane, spherical or cylindrical waves [21]). However, the most significant wave function in practice is the spherical harmonic wave propagating in the direction of

a unit vector  $\mathbf{n}$  (cf. Fig.3.2 and Fig.3.4)

$$\psi(\mathbf{s}, t) = \frac{a}{s} \cos \left[ \omega \left( t - \frac{\mathbf{s} \cdot \mathbf{n}}{v} \right) + \alpha_i \right], \quad (3.2)$$

where the argument of the cosine term is called phase,  $\alpha_i$  is the initial phase at the time  $t_0$ ,  $a$  is the amplitude. At this point we may define the frequency  $\nu$  of the harmonic wave as

$$\nu = \frac{\omega}{2\pi} = \frac{1}{T} \quad (3.3)$$

and since the wave function changes periodically with period  $T$ , i.e.  $f(t) = f(t+T)$ , we call the parameter  $T$  the period of the wave oscillations. Moreover, the value of the wave function (3.2) remains constant at the points  $\mathbf{s}$  and  $\mathbf{s} + \lambda \mathbf{n}$  [25] when

$$\lambda = \frac{2\pi v}{\omega}, \quad (3.4)$$

where  $\lambda$  stands for the wavelength of the wave, referring to the smallest spatial period of the wave and is in a close relationship to the wave vector  $\mathbf{k}$  defined as

$$\mathbf{k} = \frac{2\pi}{\lambda} \mathbf{n}. \quad (3.5)$$

For spherical waves we may effectively assume only the amplitude (length)  $k$  of the wave vector  $\mathbf{k}$

$$k = \frac{2\pi}{\lambda} \quad (3.6)$$

and rewrite Eq.(3.2) using Eq.(3.6) in form

$$\psi(s, t) = \frac{a}{s} \cos(\omega t - ks + \alpha_i), \quad (3.7)$$

which represents divergent spherical harmonic wave propagating in the direction of the vector  $\mathbf{n}$ . For further mathematical analysis, it is more effective to use complex notation of harmonic waves instead of trigonometric functions. Based on the Euler formula [26] we can rewrite the spherical wave function in the following form

$$\psi(s, t) = \frac{A}{s} \exp(iks) \exp(-i\omega t), \quad (3.8)$$

where

$$A = a \exp(-i\alpha_i) \quad (3.9)$$

is the complex envelope of the wave  $\psi(s, t)$ .

Now, the wave function consists of two terms dependent on the spatial and time coordinate, respectively.

$$\psi(\mathbf{s}, t) = \psi(\mathbf{s}) \exp(-i\omega t). \quad (3.10)$$

Since the wavelength  $\lambda$  and frequency  $\nu$  remain constant during diffraction effects, assuming a non-dispersive environment, we may deal only with the spatial term of Eq.(3.10), which for the case of divergent spherical harmonic wave propagating in the direction of the vector  $\mathbf{k}$  is

$$\psi(\mathbf{s}) = A \frac{\exp(iks)}{s}. \quad (3.11)$$

Note: observed quantity is not the wave function  $\psi(\mathbf{s})$ , but the optical intensity  $I(\mathbf{s})$ . Luckily, its representation using the complex notation of wave function is considering the harmonic waves, relatively easy and is proportional to the square of the modulus of the spatial term of the wave function  $\psi(\mathbf{s})$

$$I(\mathbf{s}) \propto \psi(\mathbf{s})\psi^*(\mathbf{s}) = |\psi(\mathbf{s})|^2. \quad (3.12)$$

In practical applications we assume that the propagating optical wave is observed at a distance  $z$ , which is significantly larger than its wavelength  $\lambda$  and close to the axis. The condition of the paraxial approximation is mathematically expressed for length  $s$  of the vector  $\mathbf{s}$  (cf. Fig.3.2) from the origin in the transmitter plane  $\Sigma_{\text{TxA}}$  to the observation point  $P$  at the observation (receiver) plane  $\Sigma_{\text{RXA}}$  as

$$s = \sqrt{x^2 + y^2 + z^2} = z\sqrt{1 + \varepsilon^2} \approx z, \text{ where } \varepsilon = \frac{\sqrt{x^2 + y^2}}{z} \ll 1 \quad (3.13)$$

with relative precision  $\varepsilon^2/2$ . It may now approximately represent denominator in Eq. (3.11). The exponential term in numerator in Eq.(3.11), however, requires more precise approximation and can be expressed as

$$\exp(iks) \approx \exp(ikz) \exp\left[\frac{ik}{2z}(x^2 + y^2)\right]. \quad (3.14)$$

Finally, substituting (3.13) and (3.14) into (3.11) yields

$$\psi(\mathbf{s}) \propto \frac{\exp(iks)}{s} \approx \frac{\exp(ikz)}{z} \exp\left[\frac{ik}{2z}(x^2 + y^2)\right], \quad (3.15)$$

which is an equivalent form used by Fresnel to interpret diffraction effects in 1818. Therefore, approximation in (3.15) is called Fresnel approximation (of the spherical wave) as was shown in [25]. We will see the benefit of using it in the next part, where it will be used to derive Fresnel diffraction integral from the Huygens-Fresnel principle.<sup>1</sup> More complex expression of the wave function  $\psi$  of the Gaussian beam

---

<sup>1</sup>Exact diffraction theory is based on solving the Maxwell equations, provided they satisfy boundary conditions, characterising shape and properties of the diffraction aperture. This approach is mathematically much more challenging and provides solution only to a limited number of scenarios.

with elliptically symmetrical distribution is given by

$$\begin{aligned} \psi(x, y, z) = & \sqrt{\frac{w_{0x}w_{0y}}{w_x w_y}} \exp \left[ - \left( \frac{x}{w_x} \right)^2 - \left( \frac{y}{w_y} \right)^2 \right] \cdot \\ & \cdot \exp \left\{ ik \left[ z + \frac{x^2}{2R_x} + \frac{y^2}{2R_y} + \arctan \left( \frac{k(w_{0x}^2 + w_{0y}^2)}{2z - kw_{0x}w_{0y}} \right) \right] + i\frac{\pi}{2} \right\}, \end{aligned} \quad (3.16)$$

where  $w_{0x}$  and  $w_{0y}$  are beam half-widths in beam waist in  $x$  and  $y$  axis, respectively and

$$\begin{aligned} w_x = w_x(z) &= w_{0x} \left[ 1 + \left( \frac{\lambda z}{\pi w_{0x}^2} \right)^2 \right]^{1/2}, \\ w_y = w_y(z) &= w_{0y} \left[ 1 + \left( \frac{\lambda z}{\pi w_{0y}^2} \right)^2 \right]^{1/2}, \\ R_x = R_x(z) &= z \left[ 1 + \left( \frac{\pi w_{0x}^2}{\lambda z} \right)^2 \right], \\ R_y = R_y(z) &= z \left[ 1 + \left( \frac{\pi w_{0y}^2}{\lambda z} \right)^2 \right], \end{aligned} \quad (3.17)$$

are beam half-widths  $w$  and beam radii  $R$  in  $x$  and  $y$  axis, respectively [27]. According to Eq.(3.12), the detected optical intensity distribution  $I(x, y, z)$  of an elliptically symmetrical planar Gaussian beam is

$$I(x, y, z) = \frac{w_{0x}w_{0y}}{w_x w_y} \exp \left[ -2 \left( \frac{x^2}{w_x^2} + \frac{y^2}{w_y^2} \right) \right]. \quad (3.18)$$

However, due to astigmatism properties of the beam, the spherical wavefront and the circular irradiance pattern are never observed at the same time (see Fig.3.1, where it's shown that conditions for spherical wavefront (i.e.  $R_x = R_y$ ) and circular beam shape (i.e.  $w_x = w_y$ ) cannot be fulfilled simultaneously). There are two main important implications of this fact with respect to the OWC. First, there exists point  $z_R$  on axis  $z$ , where the optical intensity distribution is circular, i.e. where  $w_x(z_R) = w_y(z_R)$

$$z_R = \frac{k}{2} w_{0x} w_{0y} = \frac{\pi}{\lambda} w_{0x} w_{0y}, \quad (3.19)$$

which in case when  $w_{0x} = w_{0y}$  is called Rayleigh distance. This distance is also the boundary between near and far-field zone. Second, the orientation of the main axis changes from the  $z_R$  onward. The reason may be derived from Eq. (3.17)

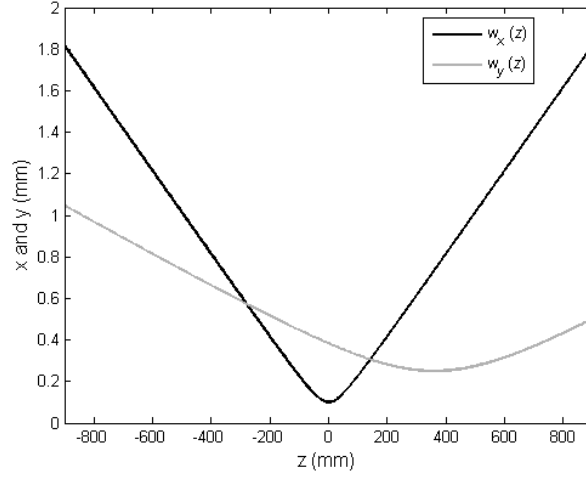
$$\frac{w_x}{w_y} \propto \begin{cases} \frac{w_{0x}}{w_{0y}} & \text{for } z \ll z_R, \\ \frac{w_{0y}}{w_{0x}} & \text{for } z \gg z_R. \end{cases} \quad (3.20)$$

Another interesting aspect is the Gouy phase shift [28], which causes phase to change by  $\pi$  at the  $z_R$ . Also the beam (half-angle) divergence  $\theta$  varies in the direction

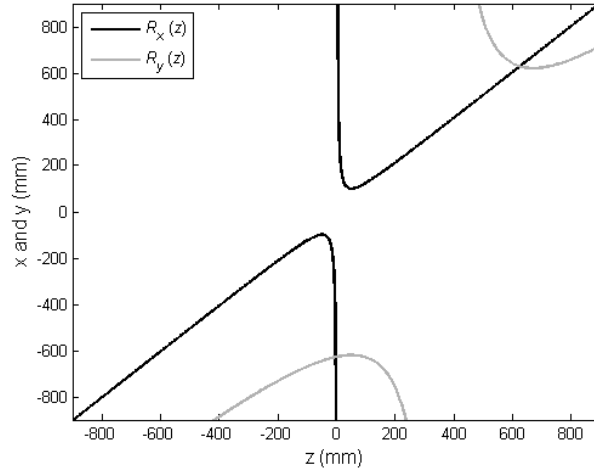
of axis  $x$  and  $y$

$$\begin{aligned}\theta_x &= \frac{2}{kw_{0x}} = \frac{\lambda}{\pi w_{0x}}, \\ \theta_y &= \frac{2}{kw_{0y}} = \frac{\lambda}{\pi w_{0y}},\end{aligned}\tag{3.21}$$

respectively, which gives rise to the astigmatism in laser beams. Wave function of



(a)



(b)

Fig. 3.1: Evolution of the beam widths  $w_x(z)$  and  $w_y(z)$  (a) and evolution of the beam radii  $R_x(z)$  and  $R_y(z)$  (b) along the  $z$  axis, where negative and positive values represent a converging and a diverging wave, respectively.  $z = 0$  corresponds to the location of beam waist. Simulation parameters:  $w_{0x} = 0.1$  mm,  $w_{0y} = 0.25$  mm,  $\lambda = 633$  nm, distance  $\Delta_z$  between both beam waists was 360 mm due to astigmatism.

an orthogonal astigmatic (elliptical) laser beam is then

$$\psi(x_M, y_M) = \frac{\exp\left(ik\sqrt{z_1 z_2}\right)}{\sqrt{z_1 z_2}} \exp\left[\frac{ik}{2}\left(\frac{x_M^2}{z_1} + \frac{y_M^2}{z_2}\right)\right] \exp\left[-\left(\frac{x_M^2}{w_x^2} + \frac{y_M^2}{w_y^2}\right)\right], \quad (3.22)$$

where  $z_1$  and  $z_2$  are distances from the point  $M$  to virtual sources of astigmatic radiation in  $x$  and  $y$  direction, respectively. Wave equation according to (3.22) represents more general case of a laser beam. When  $z_1 = z_2$ , i.e. when the wave is non-astigmatic and  $w_x = w_y$ , i.e. wave is circularly symmetrical, we obtain the circular divergent Gaussian beam as the product of the Fresnel approximation of a spherical wave and the exponential envelope defining the Gaussian shape of the intensity distribution.

As will be shown later, the wave  $\psi_0(x_M, y_M)$  in Eq. (3.29) consists of the incident wave (3.22) in the plane  $\Sigma_{\text{TXA}}$  and the circular aperture defined by its transmission function

$$t(x_M, y_M) = \text{circ}\left(\frac{x_M^2 + y_M^2}{r_{\text{TXA}}^2}\right), \quad (3.23)$$

where  $\text{circ}(x)$  is function defined by

$$\text{circ}(x) = \begin{cases} 1 & \text{for } x \leq 1, \\ 0 & \text{elsewhere.} \end{cases} \quad (3.24)$$

Finally, we may assume the primary wave in the Fresnel diffraction integral in form

$$\psi_0(x_M, y_M) = \psi(x_M, y_M) \cdot t(x_M, y_M), \quad (3.25)$$

The main advantage is that the expression 3.25 describes the source radiation in Cartesian coordinates (rather than in polar as is usual), which is of a great benefit for further computer processing and simulations (e.g. in MATLAB).

As will be shown in following sections, there are several methods to solve Fresnel diffraction integrals practically in order to avoid dealing with a rather complex Rayleigh-Sommerfeld diffraction integral. One, based on FFT-based calculation has been introduced previously and will be discussed more in depth later in this chapter. However, at first a second method, for very common circularly symmetrical scenarios as an alternative to the FFT-based model, will be shown. It uses integration of the product of Bessel and trigonometric functions.

## 3.2 Fresnel diffraction integral

According to the original Huygens principle, every point of a homogeneous isotropic environment to which the wave travels (each point on the front of the wave) may be

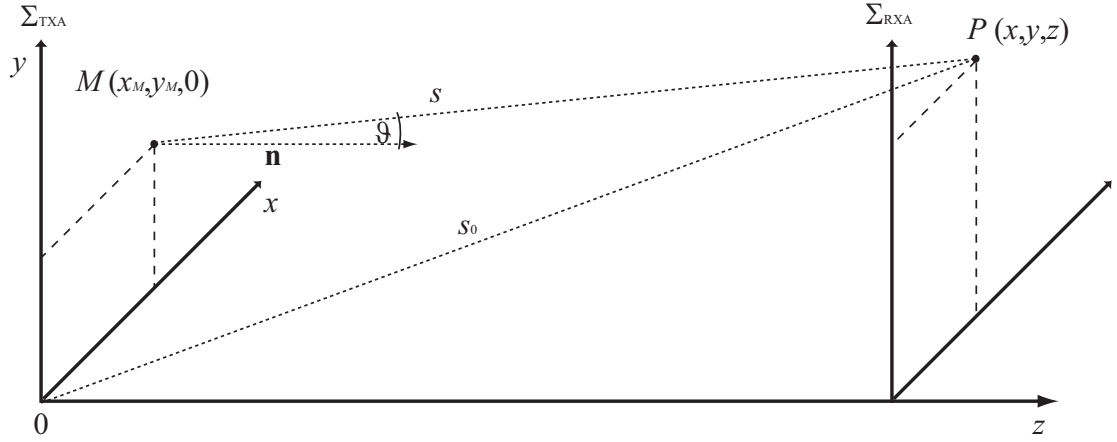


Fig. 3.2: To the explanation of Huygens-Fresnel principle in Cartesian coordinates.

considered a source of a secondary disturbance (spherical wavelets) and the resulting wavefront is determined by the envelope of these disturbances at any later instant. Augustin Jean Fresnel modified the Huygens principle and stated that these waves interfere with each other and specified their amplitude and phase [23, 25]. Resulting secondary wave  $\psi(s, \vartheta)$  emerging from the point  $M$  on the surface  $\Sigma_{\text{TXA}}$  (cf. Fig.3.2) is

$$\psi(s, \vartheta) = -\frac{i}{\lambda} K(\vartheta) \psi_0(M) \frac{\exp(iks)}{s}, \quad (3.26)$$

where  $s$  is the distance of the observation point  $P$  from the point  $M$ ,  $\vartheta$  stands for the angle between normal to the plane  $\Sigma_{\text{TXA}}$  and the direction  $s$ , factor  $K(\vartheta)$ , often referred to as inclination factor, can be, according to Fresnel, in most applications (including OWC) defined as  $K(\vartheta) = 1$  and  $\psi_0(M)$  is the known value of the wave function at the point  $M$  of the wavefront  $\Sigma_{\text{TXA}}$  called the primary wave. The discrepancy in the dimension of the secondary wave in Eq. 3.26 is given by the fact that secondary wave is, in the true (physical) sense not a wave, while the value of the function  $K(\vartheta)$  may determine whether it is the solution of the Helmholtz equation.

Value of the wave function  $\psi(P)$  at the point  $P$  (outside surface  $\Sigma_{\text{TXA}}$ ) is given as the sum of individual secondary waves emerging from the point  $M$  as

$$\psi(P) = -\frac{i}{\lambda} \iint_{\Sigma_{\text{TXA}}} \psi_0(M) \frac{\exp(iks)}{s} d\Sigma_{\text{TXA}}. \quad (3.27)$$

Diffraction integral for Fresnel diffraction effects can be derived by substituting

spherical wave  $\psi_0$  in (3.27) by its Fresnel approximation (3.15)

$$\psi(P) = -\frac{i}{\lambda} \iint_{\Sigma_{\text{TXA}}} \psi_0(x_M, y_M) \exp \left\{ \frac{ik}{2z} [(x - x_M)^2 + (y - y_M)^2] \right\} dx_M dy_M. \quad (3.28)$$

Subsequently, by expanding the square in the phasor and small modification one comes to the Fresnel diffraction integral

$$\begin{aligned} \psi(x, y, z) = & -\frac{i \exp(ikz)}{\lambda z} \exp \left[ \frac{ik}{2z} (x^2 + y^2) \right] \iint_{\Sigma_{\text{TXA}}} \psi_0(x_M, y_M) \times \\ & \times \exp \left[ \frac{ik}{2z} (x_M^2 + y_M^2) \right] \exp \left[ -\frac{ik}{z} (xx_M + yy_M) \right] dx_M dy_M, \end{aligned} \quad (3.29)$$

where the wave function characterising Fresnel diffraction integral is expressed in form of Fourier transform of product of the wave function  $\psi_0$  at the plane of diffraction aperture (in OWC TX lens socket) and of the phasor  $\exp \left[ \frac{ik}{2z} (x_M^2 + y_M^2) \right]$ . Fraunhofer diffraction phenomena may be regarded as a special case of more general Fresnel diffraction when this phasor is one (i.e. when the  $z \rightarrow \infty$ ), or more precisely, when it oscillates slow enough to be taken out of the integral in (3.29). To distinguish between various diffraction scenarios, one may effectively calculate the number of the Fresnel zones observed in the observation plane  $\Sigma_{\text{RXA}}$  represented by the Fresnel number  $N_f$ , which is derived as follows.

Let a spherical (primary) wave emerge from the point source  $P_1$  and in the distance  $z_1$  let there be a spherical wavefront  $S$ . In the distance  $z_1 + z$  from the source let there be the point of observation  $P$  (in the plane  $\Sigma_{\text{RXA}}$ ). Then, let  $\sigma_0, \sigma_1, \sigma_2, \dots$  be spherical surfaces with radii  $z, z + \lambda/2, z + 2\lambda/2, \dots$ , respectively, with the centre at the point  $P$ . These waves divide the equiphase surface  $S$  into zones. Now, let  $\psi_1, \psi_2, \psi_3, \dots$  mark sums of these secondary waves coming to the point  $P$  from the first, second, third,  $\dots$  zone respectively, then it is obvious, that  $\psi_2$  will have opposite phase, than  $\psi_1$  and so on. For radius  $r_n$  of  $n^{\text{th}}$  zone according to Pythagorean theorem (cf. Fig.3.3) yields

$$\begin{aligned} (z_1 - \Delta)^2 + r_n^2 &= z_1^2 \\ (z + \Delta)^2 + r_n^2 &= \left( z + n\frac{\lambda}{2} \right)^2. \end{aligned} \quad (3.30)$$

After the exclusion of  $\Delta$  we obtain

$$r_n^2 = \frac{n\lambda z_1 z}{z_1 + z} \left[ 1 + \frac{1}{2} \left( \frac{n\lambda}{2} \right) \frac{z_1^2 + z_1 z - z^2}{z_1 z (z_1 + z)} - \frac{1}{2} \left( \frac{n\lambda}{2} \right)^2 \frac{1}{z_1 (z_1 + z)} - \frac{1}{8} \left( \frac{n\lambda}{2} \right)^3 \frac{1}{z_1 z (z_1 + z)} \right]. \quad (3.31)$$



transmitted. When the radius is increased even more, the whole process repeats. Modulus of the wave function amplitude reaches maximum when an odd number of Fresnel zones is transmitted.

This maximum intensity is derived in [25], section 5.8.1. Here, the expression as Fresnel formulated it will be mentioned. Despite of Fresnel's inaccurate reasoning, this expression appeared to be correct. When an odd number of Fresnel zones is transmitted through the circular aperture, the optical intensity at  $P$  is quadruple compared with optical intensity that would be at this place in case of no shield is present, i.e. wave function would be double. This implies that if only half of the first Fresnel zone is transmitted, the optical intensity at the point  $P$  would be the same as in case of not restricted wave. Fresnel was aware of this result Fresnel and he supported it with an assumption, which he had known was incorrect. He calculated contribution  $\psi_i$  of individual zones

$$\psi(P) = \frac{1}{2}\psi_1 + \left(\frac{1}{2}\psi_1 + \psi_2 + \frac{1}{2}\psi_3\right) + \dots + \psi_\vartheta = \frac{1}{2}\psi_1, \quad (3.34)$$

and left out half of the contribution of the last zone

$$\psi_\vartheta = \frac{1}{2}\psi_n, \text{ resp. } \psi_\vartheta = \frac{1}{2}\psi_{n-1} + \psi_n.$$

He justified this with zero value of an inclination factor  $K(\vartheta) = \cos \vartheta$  for  $\vartheta = \pi/2$ .

Simply contribution of wave function from each even zone compensated with contributions from halves of adjacent odd zones. Result, even when not derived mathematically correctly, represents the reality.

When the planar incident wave is considered, surface  $S$  is planar and from the Pythagorean theorem can be for outer radius  $r_n$  of  $n^{\text{th}}$  Fresnel zone derived

$$r_n = \sqrt{n\lambda z} \sqrt{1 + \frac{n\lambda}{4z}}. \quad (3.35)$$

One may with high accuracy presume, that

$$r_n = \sqrt{n\lambda z}. \quad (3.36)$$

In optics, number of Fresnel zones  $n$  is often represented by the Fresnel number  $N_f$  to avoid confusion with the notation of the refractive index.

Fraunhofer region (also called far-field zone) is the region where  $N_f \ll 1$ . As the  $N_f$  approaches and exceeds one, the phasor discussed in Eq. (3.29) becomes relevant and resulting diffraction effects are called Fresnel diffraction. This region is often referred to as near-field zone. Not only in the optical instrumentation and in the laboratory is Fresnel diffraction limiting factor, but should also be taken into account during FSO link design. For instance, when one-inch transmitter optics

( $r_{\text{TXA}}$ ) and wavelength  $\lambda = 1550$  nm are considered, the near-field zone boundary (Rayleigh distance) is according to Eq. (3.36) as far as  $z = 416$  m. In many instances, the terrestrial FSO links do not exceed this distance and, therefore, work in the near-field zone.

An important part of the calculation is the right mathematical expression of the primary wave function  $\psi_0$  into diffraction integral respecting the physical properties of the transmitted beam. In practice, one should always consider diffraction of an elliptically symmetrical spherical wave on a circularly symmetrical aperture, which, however, excludes almost any analytical calculation. Another important aspect to take into account is the curvature radius of the wavefront, which depends on the beam divergence angle and last, but not least, the beam astigmatism. These effects form the main research focus of author.

### 3.3 Fresnel diffraction in form of integration of Bessel functions

Following section provides derivation and description of the Fresnel diffraction integral in terms of Bessel function integration for circularly symmetrical scenario. Let the planar optical wave with constant intensity distribution illuminate a circular aperture of the radius  $\rho_0$  in an opaque screen. When circularly symmetrical scenario is considered, cylindrical coordination system (cf. Fig.3.4) instead of Cartesian may be used to express the exponential term in (3.27). The distance  $s$  between  $M$  and  $P$  can be in cylindrical coordinates expressed in terms of Fresnel approximation as [29]

$$s^2 = \rho^2 + r^2 - 2\rho r \cos(\varphi - \theta) + z^2, \quad (3.37)$$

which yields

$$\frac{\exp(iks)}{s} \approx \frac{\exp\left[ik\left(z + \frac{r^2}{2z}\right)\right]}{z} \exp\left\{\frac{ik}{2z}\left[\rho^2 - 2\rho r \cos(\varphi - \theta)\right]\right\}. \quad (3.38)$$

Taylor expansion used for the approximation limits the validity of the expression and defines the validity condition defined in [30]

$$z > \frac{r_{\text{TXA}}^2 \pi}{2\lambda}. \quad (3.39)$$

Now, substituting expression (3.38) into (3.27) yields for the wave function at the observation point  $P$  in the receiver plane  $\Sigma_{\text{RXA}}$

$$\psi(P) = -\frac{i}{\lambda} \frac{\exp\left[ik\left(z + \frac{r^2}{2z}\right)\right]}{z} \int_0^{r_{\text{TXA}}} \exp\left(\frac{ik}{2z}\rho^2\right) \int_0^{2\pi} \exp\left[-\frac{ik}{z}\rho r \cos(\varphi - \theta)\right] d\varphi \rho d\rho, \quad (3.40)$$

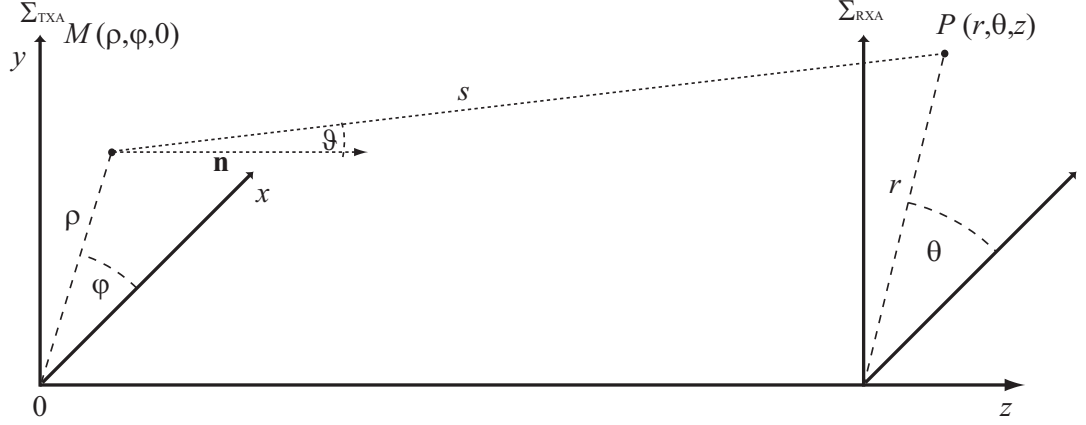


Fig. 3.4: To the explanation of Huygens-Fresnel principle in cylindrical coordinates.

where the exponential term in the inner integral may be solved using expression (3.915-2.) in [31]. Then the observed wave function takes form

$$\psi(P) = -\frac{2\pi i}{\lambda z} \exp\left[\frac{2\pi i}{\lambda}\left(z + \frac{r^2}{2z}\right)\right] \int_0^{r_{\text{TXA}}} \exp\left(\frac{\pi i}{\lambda z} \rho^2\right) J_0\left(\frac{2\pi r}{\lambda z} \rho\right) \rho d\rho, \quad (3.41)$$

where  $J_0$  is the Bessel function of the first kind and zero order.

Using the substitution for  $\rho = r_{\text{TXA}} \cdot t$  we may normalise the integration limits in the integral

$$\psi(P) = -\frac{2\pi i r_{\text{TXA}}^2}{\lambda z} \exp\left[\frac{2\pi i}{\lambda}\left(z + \frac{r^2}{2z}\right)\right] \int_0^1 \exp\left(\frac{\pi i r_{\text{TXA}}^2}{\lambda z} t^2\right) J_0\left(\frac{2\pi r r_{\text{TXA}}}{\lambda z} t\right) t dt. \quad (3.42)$$

We can further simplify this expression using Eq. (3.36) and by expressing the coordinate  $r$  in the plane  $\Sigma_{\text{RXA}}$  in units of the aperture radius in the plane  $\Sigma_{\text{TXA}}$  (by means of substitution  $r = r_{\text{TXA}} \rho$ ), which yields

$$\psi(\rho, N_f) = -2\pi i N_f \exp\left[i\left(\frac{2\pi}{\lambda} z + \pi N_f \rho^2\right)\right] \int_0^1 \exp(\pi i N_f t^2) J_0(2\pi N_f \rho t) t dt. \quad (3.43)$$

Finally, using the Euler's formula (to avoid dealing with complex exponential functions), the intensity at the observation point  $P$  is given by

$$I(\rho, N_f) = |\psi \psi^*|^2 = (2\pi N_f)^2 \left\{ \left[ \int_0^1 \cos(\pi N_f t^2) J_0(2\pi N_f \rho t) t dt \right]^2 + \left[ \int_0^1 \sin(\pi N_f t^2) J_0(2\pi N_f \rho t) t dt \right]^2 \right\}. \quad (3.44)$$

As was already mentioned, there are only a few scenarios, where an exact analytical solution is possible. However, the expression in (3.44) is not the case. Therefore, a numerical solution must be carried out in order to calculate the integral in it and to evaluate the wave function at the observation point  $P$ .

Taking into consideration a complementary situation (i.e. obscuration of the planar wave by an opaque circular disc, rather than by a circular aperture of the same size), using Babinet's<sup>2</sup> principle [21], expressions for Fresnel diffraction similar to (3.44) were obtained [29, 32] thus strongly supporting its validity.

Although the use of diffraction integrals in form of Bessel functions [33] is very common (not only) in instrumental optics [34], solutions to diffraction problems with circular symmetry may be also expressed in form of Lommel functions [25] when integrating "per partes" and using a certain relationships between Bessel functions we may write for diffraction integral in (3.43)

$$\int_0^1 \exp\left(\frac{i}{2}ut^2\right) J_0(t) t dt = \frac{\exp\left(\frac{i}{2}u\right)}{u} [U_1(u, v) - iU_2(u, v)], \quad (3.45)$$

where  $U_1(u, v)$  and  $U_2(u, v)$  are Lommel functions of two variables  $u$  and  $v$  [35]. Diffraction of a spherical wave originating at a point  $(0, 0, -z_1)$  (cf. Fig.3.3) from  $\Sigma_{\text{TXA}}$  is expressed by expression (3.44) multiplied by spherical wave function  $\psi_0$  given by [25]

$$\psi_0(\rho) = \frac{\exp\left(ik\sqrt{z_1^2 + \rho^2}\right)}{\sqrt{z_1^2 + \rho^2}} \text{circ}\left(\frac{\rho}{\rho_0}\right). \quad (3.46)$$

### 3.4 Fresnel diffraction in form of FFT

Section 3.2 introduced the Fresnel diffraction integral defined in terms of the Fourier Transform in Cartesian coordinates, which can be used for more efficient computer processing of diffraction pattern simulation compared to solutions expressed in cylindrical coordinates. It benefits from numerical methods to speed up the calculation of Fourier Transform. These methods, however, require gentle treatment and full understanding of physical principles and effects that occur during diffraction [36]. Direct substitution of the Eq. (3.25) into Eq. (3.29) and its modification leads to wave function of the diffracted wave at the plane of observation  $\Sigma_{\text{RXA}}$

$$\begin{aligned} \psi(x, y, z) = & -\frac{i}{\lambda} \frac{\exp[ik(z' + z)]}{z'z} \exp\left[\frac{ik}{2z}(x^2 + y^2)\right] \cdot \\ \mathcal{F} \left\{ \text{circ}\left(\frac{x_M^2 + y_M^2}{r_{\text{TXA}}^2}\right) \exp\left\{x_M^2 \left[\frac{ik}{2}\left(\frac{1}{z_1} + \frac{1}{z}\right) - \frac{1}{w_x^2}\right] + y_M^2 \left[\frac{ik}{2}\left(\frac{1}{z_2} + \frac{1}{z}\right) - \frac{1}{w_y^2}\right]\right\} \right\}, \end{aligned} \quad (3.47)$$

---

<sup>2</sup>J. Babinet, *Comptes Rendus de l'Académie des Sciences* 4, 638 (1837).

where  $z' = \sqrt{z_1 z_2}$ ,  $\mathcal{F}$  stands for the Fourier Transform.

The main objective of the simulation of Fresnel diffraction effects leads to the estimation of the minimal distance of the FSO link operation without any disturbance in the optical intensity distribution of the transmitted beam due to the beam restriction caused by the transmitter optics. The distance is obtained from Eq. (3.36) for  $N_f = 1$ , which determines the boundary between near and far-field radiation.

One must take into account also that diffraction effects can be significantly reduced by an appropriate choice of the transmitter objective diameter  $r_{\text{TXA}}$  with respect to the beam half-width  $w(z)$  at the transmitter plane TXA. To quantitatively assess the influence of the diffraction one may use the contrast of diffraction maxima which is being reduced by an increasing ratio  $r_{\text{TXA}}/w(z)$ , as shows Fig.3.5. It is therefore essential to optimise this parameter in order to minimise the contrast of the resulting diffraction pattern taking into account increasing spherical aberration and price of the lens. Assessment of the diffraction effects is introduced in the following section.

## 3.5 Diffraction effect assessment

### 3.5.1 Experimental verification of models

This section presents simulation results of individual models and discusses their validity and application. First, experimental verification of both models presented in the previous section will be shown on a circularly symmetrical scenario, where both the diffraction aperture and the Gaussian beam will have a circular symmetry and an identical axis of symmetry. Simulation of more general cases will follow the definition of the diffraction pattern contrast. This section is presented in form as submitted to Special Issue on Optical Wireless Communications in IEEE Journal of Selected Areas in Communications.

In order to study a model's validity, one must ensure proper conditions of the system setup. The transmitted laser beam was generated by a coherent He-Ne laser at the wavelength  $\lambda = 543.5$  nm, which was additionally spatially filtered using a limiting-mode diaphragm in order to obtain a single-mode Gaussian beam at the transmitter plane  $\Sigma_{\text{TXA}}$ .

Another important aspect is the beam collimation since the models (3.44) and (3.29) assume a planar wave. Collimation was carried out with a planoconvex lens with negligible spherical aberration. Laser beam collimation can be very roughly carried out by measuring the beam spot diameter along the  $z$  axis. However, in this experiment, a more precise collimation method [37] was used. The collimated laser beam was then restricted by a precise aperture with radius  $r_{\text{TXA}} = 4$  mm and

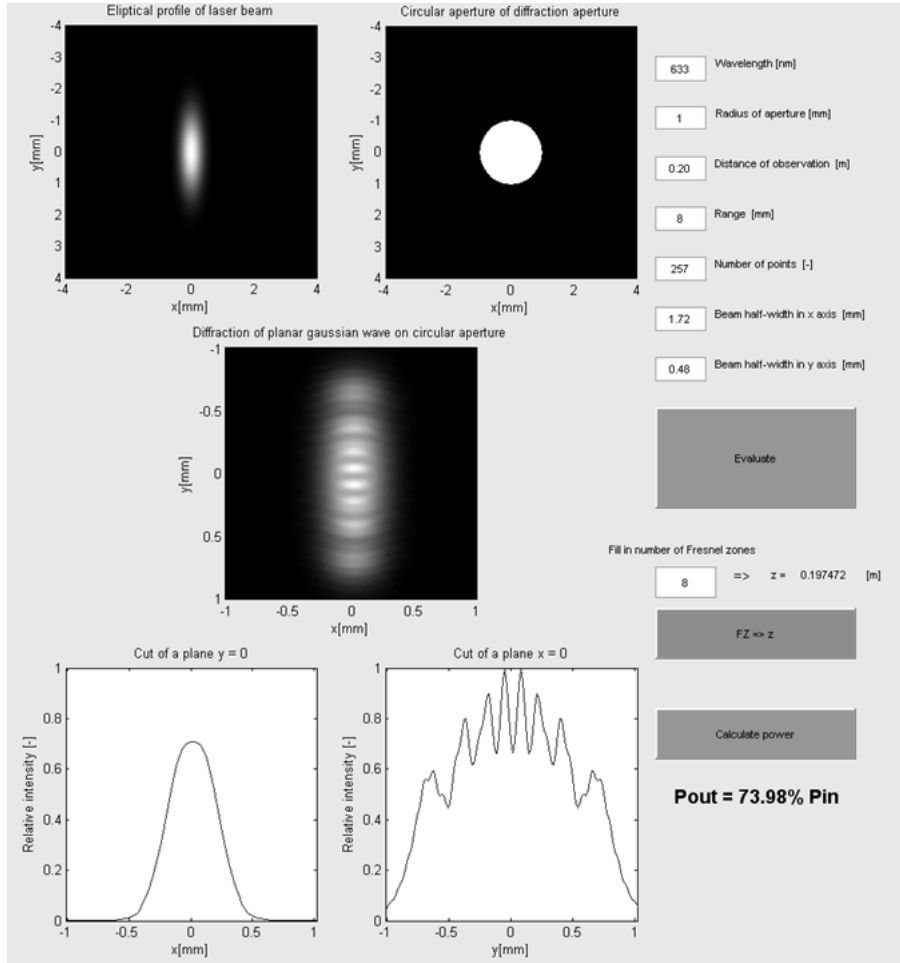


Fig. 3.5: Simulation of Fresnel diffraction effect in FSO systems. Top left - primary elliptical Gaussian beam with beam-widths  $w_x = 1.72$  mm and  $w_y = 0.48$  mm in  $x$  and  $y$  axis, respectively. Top right - circular aperture (TXA) with radius  $r_{\text{TXA}} = 1$  mm. Central plot shows the diffracted beam in the plane of observation  $r_{\text{RXA}}$  and bottom left and right - optical intensity of the diffracted beam along  $x$  and  $y$  axis, respectively. In the bottom left section, power  $P_{\text{out}}$  transmitted through the circular aperture is calculated relative to the total radiated power  $P_{\text{in}}$  of the optical source.

observed (and captured on a CCD sensor) at various distances corresponding to the given number of observed Fresnel zones  $N_f$  (see Fig.1.4 for the case of  $N_f = 4$ ). The measurement results shown in Fig.3.6 were obtained by the method of scanning the laser beam profile at given distance  $z$  using a photodiode with an aperture with diameter  $D_a = 0.5$  mm.

An experiment is always valid within limits of measurement (experimental) error  $\delta_e$  defined as the difference between measured value of a physical quantity and its

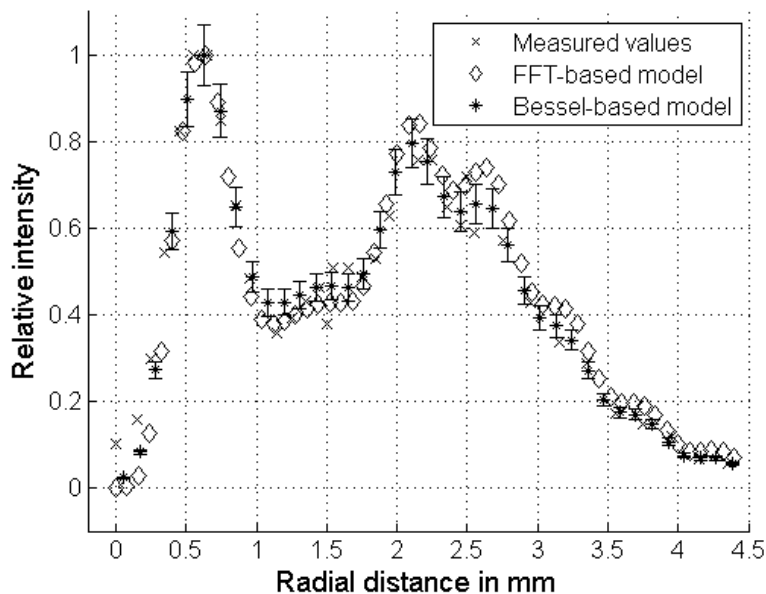


Fig. 3.6: Measured data ( $\times$ ) is in very good agreement with the model based on the integration of the Bessel function (3.44) ( $*$ ) and FFT-based model (3.29) ( $\diamond$ ). Parameters of the experiment and simulations: Wavelength  $\lambda = 543.5$  nm, transmitter aperture  $r_{\text{TXA}} = 4$  mm, distance  $z$  to the observation plane  $\Sigma_{\text{RXA}} z = 7.36$  m, which corresponds to the number of observed Fresnel zones  $N_f = 4$  and assuming a collimated circular Gaussian beam with beam half-width  $w = 14$  mm. Measurement error was estimated as  $\delta_e = 7.95\%$ .

actual value. The error  $\delta_e$  in this case was influenced by the collimation uncertainty  $\delta_c = 0.2\%$ , uncertainty of the distance measurement  $\delta_z = 1.5\%$ , uncertainty of the aperture size setting  $\delta_a = 1.25\%$  and mainly by the uncertainty of the sensor readout  $\delta_{\text{VPP}} = 5\%$ , all of which sum up the total estimated measurement error  $\delta_e = 7.95\%$ , which is also shown in Fig.3.6.

### 3.5.2 Model based on the Bessel functions integration

The Bessel-based model in (3.44) shows in Fig.3.7a) how the circular Gaussian beam intensity distribution changes due to diffraction along the link path. In order to compare the model with precise, but a computationally demanding, calculation of the diffraction effects based on Rayleigh-Sommerfeld integral presented in [38] and also for more general comparison, axial distance along the link path is shown in the units of aperture radii. First, comparing Fig.3.7a) and Fig.3.7b) [38] one may see that the benefit of using a much simpler calculation did not influence the overall results which are objectively similar. Furthermore, it is clearly visible that as we

move the receiver plane  $\Sigma_{\text{RXA}}$  along the optical axis, there are several positions on the  $z$  axis, where the optical intensity at the optical axis is zero and also areas where the contrast of the diffraction pattern is maximal. This is, for instance, visible at  $z \approx 4.7 \cdot r_{\text{TXA}}$ , i.e. where  $N_f = 2$ . More precisely, the beam intensity distribution changes with changing number of observed Fresnel zones  $N_f$ , which changes with  $z$ , which gives rise also to relation between contrast  $C$  and Fresnel number  $N_f$  shown in Fig.3.9.

Every cross-section of the plot in Fig.3.7a) along the  $y$  axis represents the transverse optical intensity distribution at this distance. It shows how the complicated diffracted intensity distribution near the transmitter (left) evolves into a smoother optical intensity in the Fraunhofer region (right). This is also shown in Fig.3.8 where the situation with fewer Fresnel zones  $N_f$  is shown on top ( $N_f = 1$ ) and proceeding downwards, the value of  $N_f$  increases to  $N_f = 3$  at the bottom. The upper-most plot represents the boundary between the near and far field where  $N_f = 1$ , which is the same as if we took the cross-section in Fig.3.7 at the distance  $z \approx 9.4 \cdot r_{\text{TXA}}$ . Now, as we move closer to the transmitter,  $N_f$  increases and the transverse optical intensity distribution changes rapidly with the most extreme case at  $z \approx 4.7 \cdot r_{\text{TXA}}$ , where the axial optical intensity is zero. In this scenario, if the receiver aperture  $r_{\text{RXA}}$  is much smaller than the beam radius (i.e. comparable with the central trough), the received optical power  $P_r$  will be close to zero. On the other hand, if the receiver plane is located at distance  $z \approx 3.14 \cdot r_{\text{TXA}}$ , the receiver would ideally detect the peak of the intensity pattern. The Fresnel diffraction pattern is recognisable by a series of maxima and minima. However, as can be seen, these peaks are much narrower compared to the pattern when no diffraction effect occurs. This may lead to severe beam tracking issues when an automatic PAT system is used. For better visualisation, the beam peaks were highlighted in Fig.3.8 with (o) for intensity maxima and (x) for minima of the optical intensity. These peaks will now be used to study and to objectively assess the contrast of the diffraction pattern.

As was mentioned in the introductory chapter, the motivation for the study of diffraction effects in FSO systems and the main problem it causes is related to the (nonzero) contrast of the diffraction pattern. Contrast or visibility of individual fringes is studied and defined in interference patterns to determine, for instance the degree of coherence between two individual optical beams in interferometers [39]. Contrast  $C$  of the diffraction peaks (similarly to the visibility  $V$  of the interference fringes) is defined as

$$C = \frac{I_{\max} - I_{\min}}{I_{\max} + I_{\min}}, \quad (3.48)$$

where  $I_{\max}$  and  $I_{\min}$  are the first optical intensity maximum and minimum in the spot of the diffracted beam closest to the optical axis, respectively. Note, that the

contrast  $C$  strongly relates to the number of observed Fresnel zones  $N_f$ .

Above it was shown that as the beam propagates within the near field zone, the transverse optical intensity distribution changes rapidly and the highest contrast is expected when a whole number (larger than one) of Fresnel zones is observed. Fig.3.9 shows these local maxima and the periodic change of the contrast as more Fresnel zones are visible. It is not surprising that the minimum of the function lays always at the points corresponding to the area around half-number of the visible Fresnel zones  $N_f$ , i.e. when  $N_f \approx n + 1/2$  for  $n$  being the non-negative integer. As a result, one is now able to determine the optimal transmitter aperture radius  $r_{\text{TXA}}$  according to (3.36) to reduce the spurious effects of a diffracted laser beam. This leads to lower error during APT operation for data links and more reliable data for testing FSO links. Please note that what is shown here is the worst-case scenario when the contrast may reach 100%. The contrast is significantly reduced as the ratio of the beam half-width to aperture radius  $\frac{w}{r_{\text{TXA}}}$  decreases. Although, as far as the FSO receiver is located in the near field, diffraction can never be avoided, it can be dealt with by a proper FSO link design with respect to all negative effects, including diffraction.

The Fraunhofer region, i.e. region where  $N_f < 1$ , was excluded from the analysis as there is no minimum of the intensity function within the range of interest.

### 3.5.3 Model based on the FFT

Figure 3.5 shows the simulation of the FFT-based diffraction model. After filling the simulation parameters on the right-hand side of the window, the computer performs the FFT calculation in (3.29) to evaluate the diffraction of the elliptical optical wave (in the upper-left corner of the window) on a circular aperture (upper-right). The result in the receiver plane  $\Sigma_{\text{RXA}}$  is shown in the middle. Cross-sections through the center of the optical beam along the  $x$  and  $y$  axes are shown in the bottom-left and bottom-right corner, respectively.

As was mentioned above, reducing the diffraction pattern contrast or number of observed Fresnel zones leads to more reliable performance of the PAT system. In practice, the PAT performance experiences higher error in tracking in one direction (e.g.  $y$ ) than in the direction perpendicular to it (here  $x$ ). The reason is shown in Fig.3.5 where the optical beam cross-section is smoother in one direction (bottom-left plot) than in the other (bottom-right plot), which is significantly deteriorated due to diffraction.

The situation in Fig.3.5 also shows the scenario when nearly eight Fresnel zones are observed, i.e.  $N_f \approx 8$ . Since the ratio  $\frac{w_y}{r_{\text{TXA}}}$  is around one half, we can see the

effect of the diffraction contrast reduction in the beam cross-section along the  $y$  axis, i.e. the diffraction effect is not observed.

Moreover, according to Eq. (3.48) and Fig.3.9 and assuming  $N_f = 8$ , the expected contrast of the diffraction pattern is nearly one. However, the contrast  $C_{\text{sim}}$  in the simulation in Fig.3.5 according to the cross-section in  $x$  axis (bottom right plot) is

$$C_{\text{sim}} = \frac{I_{\text{max}} - I_{\text{min}}}{I_{\text{max}} + I_{\text{min}}} = \frac{1 - 0.7}{1 + 0.7} \approx 0.2, \quad (3.49)$$

which proves the hypothesis that the contrast of the beam diffraction can be significantly optimised (decreased) by decreasing the ratio  $\frac{w_{x,y}}{r_{\text{TXA}}}$ .

The beam restriction gives rise not only to the diffraction effects. Another, not less significant aspect described in [40] is the power attenuation. The model presented in Fig.3.5 also shows in the bottom-left corner the portion of the power transmitted through the transmitter optical system and will be in detail described in Chapter 4.

## 3.6 Summary

This chapter introduced the elliptical GB as a model of a real laser beam. By means of the wave optics apparatus, I derived two models of Fresnel diffraction. One, based on the integration of Bessel function, used in circularly symmetrical scenarios when diffraction of a circular GB on a circular aperture occurs. Second model, based on FFT, is more complex and derived in Cartesian coordinates, which serves for computer analysis. In the FFT-based model, I show the Fresnel diffraction of the elliptical GB on a circular lens socket and its influence on the optical intensity distribution in the receiver plane.

Analyses carried out in the work have impact from both the theoretical and the practical aspect and have been summarised and submitted for publication in Journal on Selected Areas in Communications and presented at international conferences [41].

Theoretical work includes:

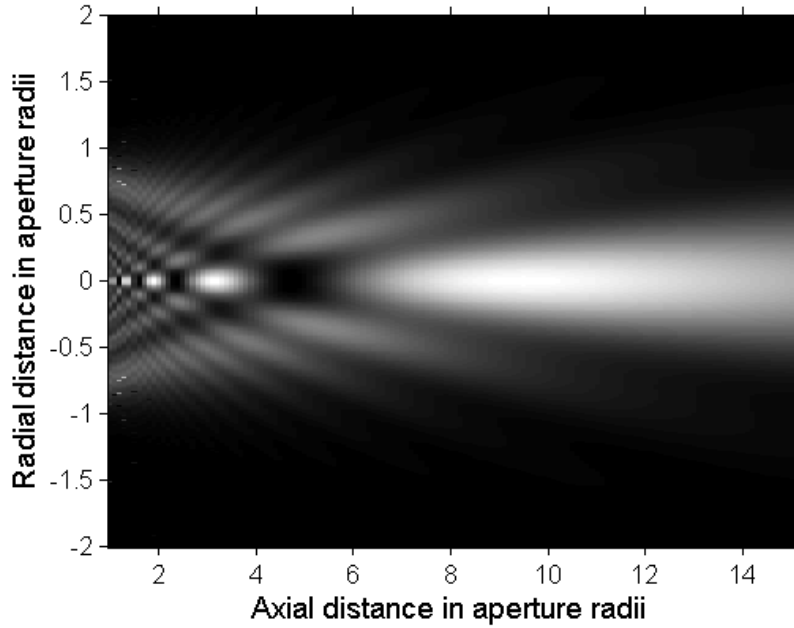
- Fresnel approximation of the elliptical GB in Cartesian coordinates
- Discussion on the astigmatism of GB
- Derivation of Fresnel diffraction integral from Huygens-Fresnel principle
- Expression of Fresnel diffraction integral in terms of Fourier transform
- Proof of validity in terms of the Babinet's principle

The practical impact of the work includes:

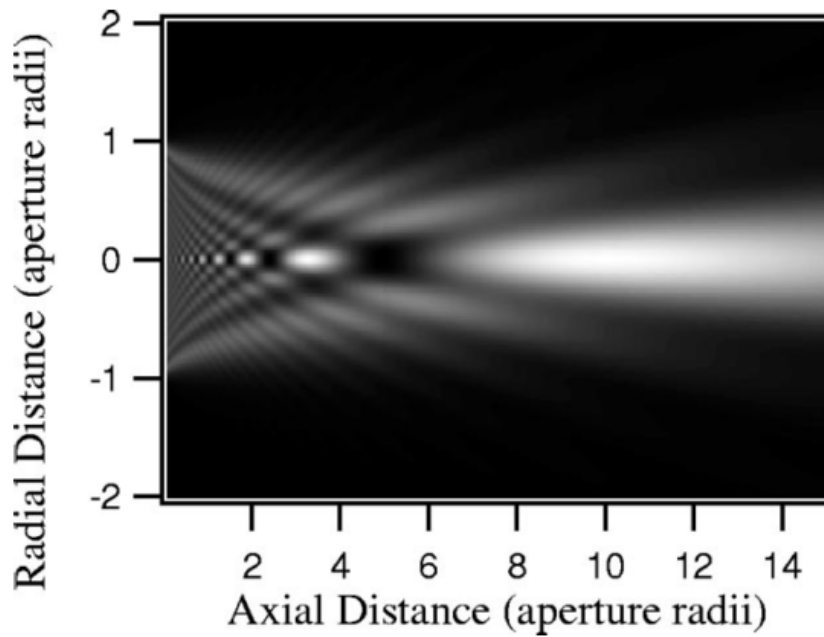
- Expression of the Fresnel diffraction integral in terms of numerical integration of Bessel function

- Expression of the Fresnel diffraction integral in terms of numerical evaluation of FFT of product of the wave function  $\psi_0$  at the plane of diffraction aperture (in OWC TX lens socket) and of the phasor  $\exp\left[\frac{ik}{2z}(x_M^2 + y_M^2)\right]$
- Qualitative discussion on the impact of the number of observed Fresnel zones in the receiver plane  $\Sigma_{\text{RXA}}$

At this point, I would like to acknowledge that most of the work described in this chapter was carried out thanks to countless hours of consultations with prof. Jiří Komrška, mainly in the first stages of the study [36, 42].



(a)



(b)

Fig. 3.7: a) Intensity distribution calculated using the method of integration of the Bessel functions as a function of both radial and axial distance from the aperture in the units of the aperture radius  $r_{\text{TXA}}$  according to (3.44).

b) Calculated intensity distributions using the complete Rayleigh-Sommerfeld model [38]. Simulation parameters:  $\lambda = 10.6 \mu\text{m}$  and  $r_{\text{TXA}} = 0.1 \text{ mm}$ . The boundary between near field and far field is located around  $z \approx 9.4 \cdot r_{\text{TXA}}$ .

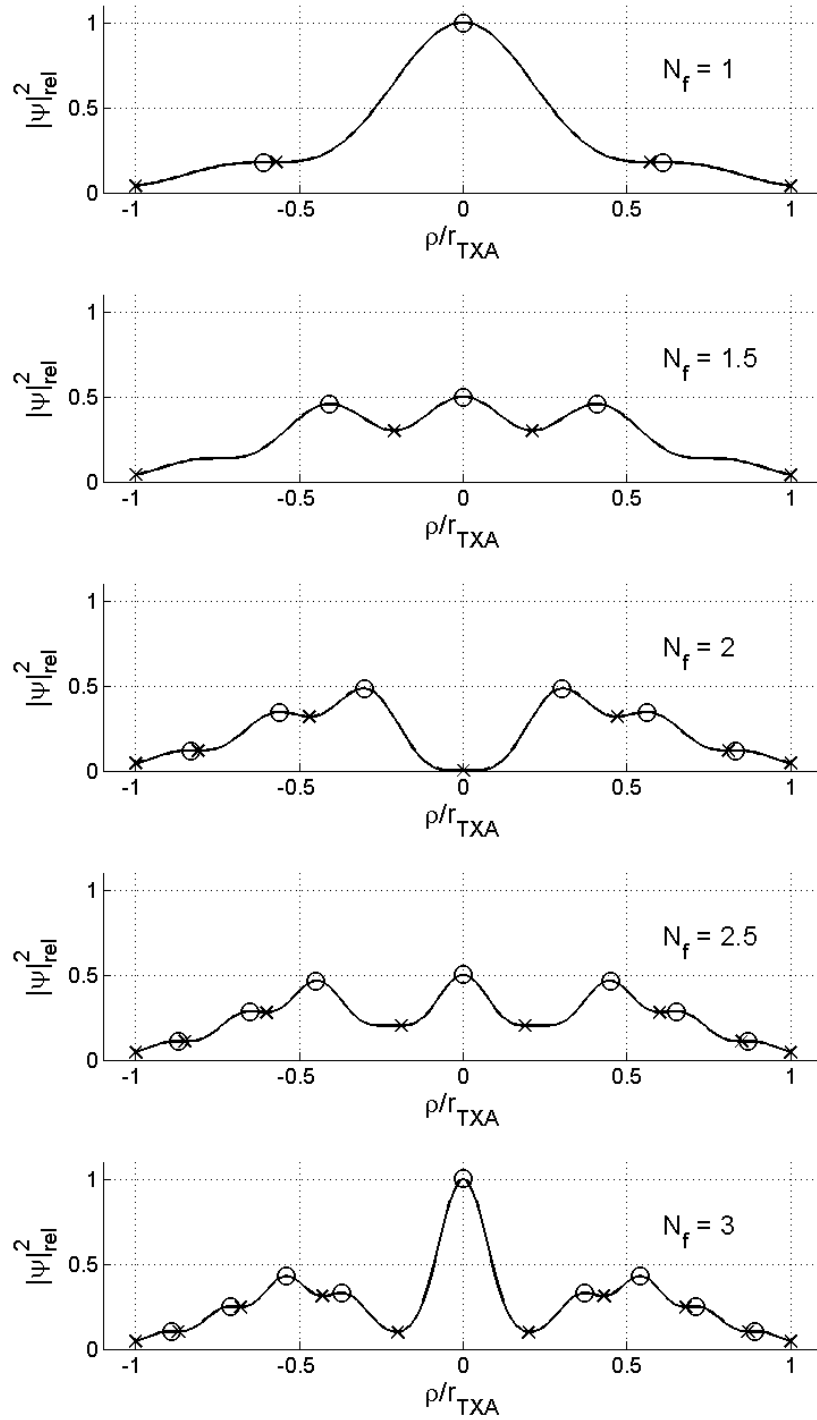


Fig. 3.8: Transverse optical intensity distributions at various distances. Extremes of the functions are highlighted: maxima(o) and minima(x). Individual plots are related to cross-sections in Fig.3.7 at various distances  $z$  corresponding to various Fresnel numbers  $N_f$ . Top to bottom:  $N_f$  changes from 1 to 3 with step 0.5, which corresponds to distances  $z_1 = 9.4340 \cdot r_{\text{TXA}}$ ,  $z_{1.5} = 6.29 \cdot r_{\text{TXA}}$ ,  $z_2 = 4.72 \cdot r_{\text{TXA}}$ ,  $z_{2.5} = 3.77 \cdot r_{\text{TXA}}$  and  $z_3 = 3.14 \cdot r_{\text{TXA}}$ .

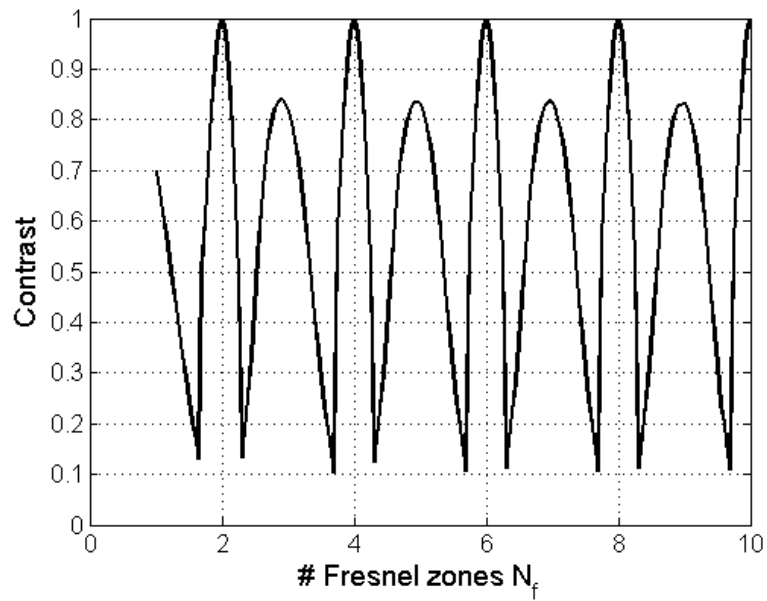


Fig. 3.9: Contrast of the central region of the diffraction pattern as a function of the number of transmitted Fresnel zones  $N_f$ . Shown are only the results in near-field zone where contrast is relevant, i.e. for  $N_f > 1$ . Contrast minima occur when  $N_f \approx n + 1/2, n \in N$ , whereas maximal contrast occurs when  $N_f$  is a whole number  $N$ .

## 4 GEOMETRICAL AND POINTING LOSS

This section introduces the derivation of the geometrical and pointing (misalignment) loss calculation for case of an elliptical Gaussian beam being restricted by a circular aperture. The main results of the work presented in this chapter was published in [40].

When the FSO link is aligned ideally, the beam optical axis and aperture axis of symmetry are identical. Optical power attenuation on RXA, when no turbulence effects are taken into account, is defined by the relative size of the beam  $w_{\text{RXA}}$  and the radius  $r_{\text{RXA}}$  and is called geometrical loss  $\alpha_{\text{geom}}$  (cf. Fig.4.1). Additional attenuation occurs when the beam and aperture axes are not identical, which gives rise to the misalignment loss  $\alpha_{\text{mis}}$ , sometimes also referred to as pointing error. The degree of the misalignment is quantified by tilt angle  $\gamma_t$  (cf. Fig.4.7).

Currently used models typically assume constant optical intensity distribution of the beam at the receiver aperture (RXA) as well as its circular symmetry. Especially in case of direct FSO links this assumption is far from reality and may degrade the overall results with a significant error. Therefore, in the following text we will show the derivation of the analytical calculation of the geometrical attenuation loss of an elliptically symmetrical Gaussian beam at a circular aperture.

Optical power  $P$  of the beam is defined

$$P(z) = \iint_{-\infty}^{\infty} I(x, y, z) dS, \quad (4.1)$$

where  $S$  is unrestricted part of the surface of the beam (theoretically infinite for unrestricted beam). In case of an elliptically symmetrical Gaussian beam described by Eq. (3.18), the total optical power  $P_0$  is

$$P_0(z) = \iint_{-\infty}^{\infty} I(0, 0, z) \exp \left[ -2 \left( \frac{x^2}{w_x^2} + \frac{y^2}{w_y^2} \right) \right] dS = I(0, 0, z) \frac{\pi}{2} w_x w_y, \quad (4.2)$$

where  $I(0, 0, z)$  is the axial optical intensity of the beam at the distance  $z$ .

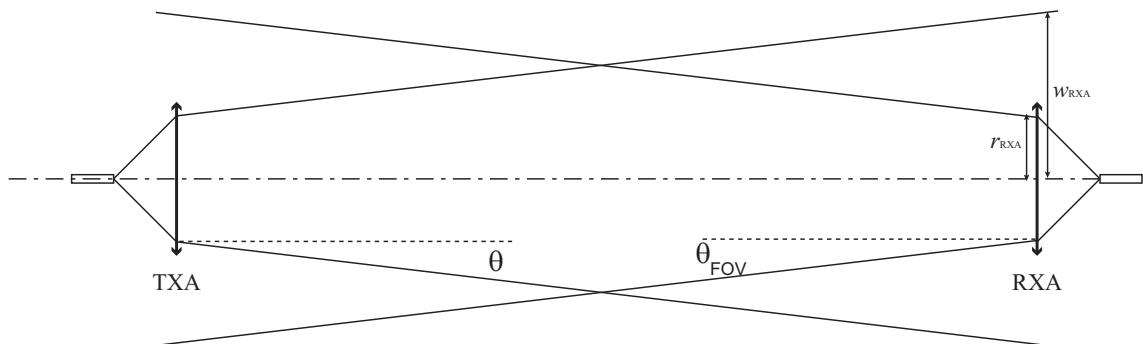


Fig. 4.1: To the explanation of geometrical attenuation loss.

Geometrical attenuation is determined by the part of the optical power transmitted from TX, which is not received by an optical receiver RX with a finite aperture with radius  $r_{\text{RXA}}$  (or  $r_{\text{TXA}}$ ) at the distance  $z$  mainly due to the beam divergence  $\theta$ . However, it is more efficient to calculate the part  $P_t$  of the beam, which is received by the receiver aperture (RXA) and divide it by the total optical power  $P_0$  (4.2) in order to estimate the losses. In such case we must calculate the integral in Eq. (4.2) within the limits given by the receiver geometry. In terms of physics, this can be expressed as the calculation of the optical power of an elliptical beam transmitted through a circular aperture, which mathematically complicates the calculation. In [41], four different calculations of a geometrical loss depending on the distance  $z$  and the radius of the receiver aperture  $r_{\text{RXA}}$  were shown - two exact formulas (4.12) and (4.18) requiring numerical integration and two approximative formulas (4.21) and (4.24). Following text shows the step-by-step derivation of these expressions.

## 4.1 Derivation of exact expressions

Power  $P_t$  of an elliptical beam with beam-widths  $w_x$  and  $w_y$  received by a circular aperture with radius  $r_{\text{RXA}}$  is given by

$$P_t = I(0, 0, z) \iint_{x^2+y^2 \leq r_{\text{RXA}}^2} \exp \left[ -2 \left( \frac{x^2}{w_x^2} + \frac{y^2}{w_y^2} \right) \right] dx dy, \quad (4.3)$$

which in polar coordinates  $(\rho, \varphi)$  yields

$$P_t = 4I(0, 0, z) \int_0^{r_{\text{RXA}}} \int_0^{\pi/2} \exp \left[ -2\rho^2 \underbrace{\left( \frac{\cos^2 \varphi}{w_x^2} + \frac{\sin^2 \varphi}{w_y^2} \right)}_A \right] d\varphi \rho d\rho, \quad (4.4)$$

where

$$\begin{aligned} A &= \frac{\cos^2 \varphi}{w_x^2} + \frac{\sin^2 \varphi}{w_y^2} = \frac{1}{w_x^2} + \left( \frac{1}{w_y^2} - \frac{1}{w_x^2} \right) \sin^2 \varphi = \\ &= \frac{1}{2} \left( \frac{1}{w_x^2} + \frac{1}{w_y^2} \right) - \frac{1}{2} \left( \frac{1}{w_y^2} - \frac{1}{w_x^2} \right) \cos 2\varphi = \\ &= \frac{1}{2} \left( \frac{1}{w_x^2} + \frac{1}{w_y^2} \right) \left[ 1 - \frac{w_x^2 - w_y^2}{w_x^2 + w_y^2} \cos 2\varphi \right]. \end{aligned} \quad (4.5)$$

## I. Integration first according to $\rho$

First, let's integrate Eq. (4.4) according to the radial variable  $\rho$  and substitute for  $t = 2A\rho^2$ , which yields

$$\int_0^{r_{\text{RXA}}} \exp(-2A\rho^2) \rho \, d\rho = \frac{1}{4A} \int_0^{2Ar_{\text{RXA}}^2} \exp(-t) \, dt = \frac{1}{4A} [1 - \exp(-2Ar_{\text{RXA}}^2)]. \quad (4.6)$$

Then, for the power  $P_t$  we may write

$$\begin{aligned} P_t &= \int_0^{\pi/2} \frac{I(0,0,z)}{A} [1 - \exp(-2Ar_{\text{RXA}}^2)] \, d\varphi = \\ &= I(0,0,z) \underbrace{\int_0^{\pi/2} \frac{d\varphi}{A}}_{I_1} - I(0,0,z) \underbrace{\int_0^{\pi/2} \frac{\exp(-2Ar_{\text{RXA}}^2)}{A} \, d\varphi}_{I_2}. \end{aligned} \quad (4.7)$$

Now, integrals  $I_1$  and  $I_2$  are calculated as follows

$$\begin{aligned} I_1 &= \int_0^{\pi/2} \frac{d\varphi}{A} = 2 \frac{w_x^2 w_y^2}{w_x^2 + w_y^2} \int_0^{\pi/2} \frac{d\varphi}{1 + \frac{w_y^2 - w_x^2}{w_y^2 + w_x^2} \cos 2\varphi} = \\ &= \frac{w_x^2 w_y^2}{w_x^2 + w_y^2} \int_0^{\pi} \frac{d\varphi}{1 + \frac{w_y^2 - w_x^2}{w_y^2 + w_x^2} \cos \varphi}, \end{aligned} \quad (4.8)$$

which can be solved by using eq.(3.661-4) in [31] for  $n = 0$ ,  $a = 1$  and  $b$  the fraction in the denominator of the integrand

$$\begin{aligned} I_1 &= \frac{w_x^2 w_y^2}{w_x^2 + w_y^2} \frac{\pi}{\sqrt{1 - \left(\frac{w_y^2 - w_x^2}{w_y^2 + w_x^2}\right)^2}} = \frac{\pi w_x^2 w_y^2}{\sqrt{(w_y^2 + w_x^2)^2 - (w_y^2 - w_x^2)^2}} = \\ &= \frac{\pi w_x^2 w_y^2}{2w_x w_y} = \frac{\pi}{2} w_x w_y. \end{aligned} \quad (4.9)$$

Finally, the integral  $I_2$  is calculated as follows

$$\begin{aligned}
I_2 &= \int_0^{\pi/2} \frac{\exp(-2Ar_{\text{RXA}}^2)}{A} d\varphi = \\
&= \frac{\exp\left[-r_{\text{RXA}}^2\left(\frac{1}{w_x^2} + \frac{1}{w_y^2}\right)\right]}{\frac{1}{2}\left(\frac{1}{w_x^2} + \frac{1}{w_y^2}\right)} \int_0^{\pi/2} \frac{\exp\left[\left(\frac{1}{w_y^2} - \frac{1}{w_x^2}\right)r_{\text{RXA}}^2 \cos 2\varphi\right]}{1 + \frac{w_y^2 - w_x^2}{w_y^2 + w_x^2} \cos 2\varphi} d\varphi = \\
&= \frac{1}{2} \frac{\exp\left[-r_{\text{RXA}}^2\left(\frac{1}{w_x^2} + \frac{1}{w_y^2}\right)\right]}{\frac{1}{w_x^2} + \frac{1}{w_y^2}} \int_0^{\pi} \frac{\exp\left[\left(\frac{1}{w_y^2} - \frac{1}{w_x^2}\right)r_{\text{RXA}}^2 \cos \varphi\right]}{1 + \frac{w_y^2 - w_x^2}{w_y^2 + w_x^2} \cos \varphi} d\varphi = \\
&= \frac{\exp\left(-r_{\text{RXA}}^2 \frac{w_x^2 + w_y^2}{w_x^2 w_y^2}\right)}{2 \frac{w_x^2 + w_y^2}{w_x^2 w_y^2}} \underbrace{\int_0^{\pi} \frac{\exp\left(\frac{w_x^2 - w_y^2}{w_x^2 w_y^2} r_{\text{RXA}}^2 \cos \varphi\right)}{1 - \frac{w_x^2 - w_y^2}{w_x^2 + w_y^2} \cos \varphi} d\varphi}_{I_3(r_{\text{RXA}}^2)}.
\end{aligned} \tag{4.10}$$

However, the integral  $I_2$ , to the best of my knowledge, has no analytical solution. Therefore, one must solve  $I_2$  by means of other methods, e.g. numerical integration. Now, the power  $P_t$  is from Eq. (4.7)

$$\begin{aligned}
P_t &= I(0, 0, z)(I_1 - I_2) = \\
&= I(0, 0, z) \frac{\pi}{2} w_x w_y - I(0, 0, z) \frac{w_x^2 w_y^2}{w_x^2 + w_y^2} \exp\left(-r_{\text{RXA}}^2 \frac{w_x^2 + w_y^2}{w_x^2 w_y^2}\right) I_3(r_{\text{RXA}}^2) = \\
&= I(0, 0, z) \frac{\pi}{2} w_x w_y \left[1 - \frac{2}{\pi} \frac{w_x w_y}{w_x^2 + w_y^2} \exp\left(-r_{\text{RXA}}^2 \frac{w_x^2 + w_y^2}{w_x^2 w_y^2}\right) I_3(r_{\text{RXA}}^2)\right].
\end{aligned} \tag{4.11}$$

Note, that  $I_1$  in the calculation represents the overall beam power and  $I_2$  the part of the power, which is shadowed by the aperture leaving only the transmitted power  $P_t$ . In practical application, we rather than expressing optical power transmitted through an optical system define the attenuation of the restricted part of the beam. First exact solution  $\alpha_{\text{ex},1}$  yields

$$\alpha_{\text{ex},1} = \frac{P_t}{P_0} = 1 - \frac{2}{\pi} \frac{w_x w_y}{w_x^2 + w_y^2} \exp\left(-r_{\text{RXA}}^2 \frac{w_x^2 + w_y^2}{w_x^2 w_y^2}\right) \int_0^{\pi} \frac{\exp\left(\frac{w_x^2 - w_y^2}{w_x^2 w_y^2} r_{\text{RXA}}^2 \cos \varphi\right)}{1 - \frac{w_x^2 - w_y^2}{w_x^2 + w_y^2} \cos \varphi} d\varphi, \tag{4.12}$$

where  $\alpha_{\text{ex},1}$  stands for the (first) exact analytical expression of the geometrical attenuation of an elliptical Gaussian beam on a circular aperture, which can be used in the FSO link budget calculations. However, expression (4.12) can only be solved by means of numerical integration methods. Therefore, we now show the integration of integrals in Eq.(4.4) in a different order.

## II. Integration first according to $\varphi$

Now, we first integrate integrals in Eq.(4.4) according to the angular variable.

Let

$$\begin{aligned}
 I_4 &= \int_0^{\pi/2} \exp \left[ -2\rho^2 \left( \frac{\cos^2 \varphi}{w_x^2} + \frac{\sin^2 \varphi}{w_y^2} \right) \right] d\varphi = \\
 &= \exp \left[ -\rho^2 \left( \frac{1}{w_x^2} + \frac{1}{w_y^2} \right) \right] \int_0^{\pi/2} \exp \left( \rho^2 \frac{w_x^2 - w_y^2}{w_x^2 w_y^2} \cos 2\varphi \right) d\varphi = \\
 &= \frac{1}{2} \exp \left[ -\rho^2 \left( \frac{1}{w_x^2} + \frac{1}{w_y^2} \right) \right] \int_0^{\pi} \exp \left( \rho^2 \frac{w_x^2 - w_y^2}{w_x^2 w_y^2} \cos \varphi \right) d\varphi,
 \end{aligned} \tag{4.13}$$

which can be calculated using eq.(3.339) in [31] as

$$I_4 = \frac{\pi}{2} \exp \left[ -\rho^2 \left( \frac{1}{w_x^2} + \frac{1}{w_y^2} \right) \right] I_0 \left( \rho^2 \frac{w_x^2 - w_y^2}{w_x^2 w_y^2} \right), \tag{4.14}$$

where  $I_0$  stands for the modified Bessel function of the first kind and zeroth order.

Now, the power  $P_t$  is

$$P_t = 2\pi I(0, 0, z) \int_0^{r_{\text{RXA}}} \exp \left[ -\rho^2 \left( \frac{1}{w_x^2} + \frac{1}{w_y^2} \right) \right] I_0 \left( \rho^2 \frac{w_x^2 - w_y^2}{w_x^2 w_y^2} \right) \rho d\rho. \tag{4.15}$$

Substitution

$$t = \left( \frac{\rho}{r_{\text{RXA}}} \right)^2 \tag{4.16}$$

yields for the power  $P_t$

$$P_t = \pi r_{\text{RXA}}^2 I(0, 0, z) \int_0^1 \exp \left( -r_{\text{RXA}}^2 \frac{w_x^2 + w_y^2}{w_x^2 w_y^2} t \right) I_0 \left( r_{\text{RXA}}^2 \frac{w_x^2 - w_y^2}{w_x^2 w_y^2} t \right) dt. \tag{4.17}$$

Again, the expression for power  $P_t$  has no analytical solution. For the second exact expression of geometrical attenuation  $\alpha_{\text{ex},2}$  we may now write

$$\alpha_{\text{ex},2} = \frac{P_t}{P_0} = \frac{2r_{\text{RXA}}^2}{w_x w_y} \int_0^1 \exp \left( -r_{\text{RXA}}^2 \frac{w_x^2 + w_y^2}{w_x^2 w_y^2} t \right) I_0 \left( r_{\text{RXA}}^2 \frac{w_x^2 - w_y^2}{w_x^2 w_y^2} t \right) dt. \tag{4.18}$$

Despite the fact that both Eq.(4.12) and Eq.(4.18) have no analytical solution, they provide equivalent and valid results. To compare their validity with experiment, an experimental setup in Fig.4.2 was used. Experimental data are shown in Table 4.1. The value of the axial optical intensity  $I(0, 0, z)$  was experimentally measured  $I(0, 0, z) = 2583 \text{ W/m}^2$ . Measured data show that the proposed expressions of geometrical attenuation are valid within the limits of the experimental error  $P_{\text{err}}$ . That is for iris diameter setting below  $2r_{\text{RXA}} \leq 2.0 \text{ mm}$   $P_{\text{err}} = 10\%$  and



Fig. 4.2: Experimental setup of the geometrical attenuation measurement used to verify validity of Eq.(4.12) and Eq.(4.18). LD - laser diode with wavelength  $\lambda = 650$  nm, mW - optical power meter. Distance  $z$  between the laser diode and Iris diaphragm was  $z = 0.2$  m, where beam half-widths were  $w_x = 1.72$  mm and  $w_y = 0.48$  mm and axial optical intensity  $I(0, 0, z) = 2583$  W/m<sup>2</sup>. Diaphragm diameter  $2r_{\text{RXA}}$  was calibrated and adjustable in range  $2r_{\text{RXA}} \in < 0.5; 5 >$  mm with 0.5 mm step.

$2r_{\text{RXA}}$	0.5	1.0	1.5	2.0	2.5	3.0	3.5	4.0	4.5	5.0
$P_{\text{det}}$	0.35	1.12	1.75	2.28	2.72	3.04	3.24	3.34	3.35	3.35
$P_{\text{sim}}$	0.44	1.30	2.00	2.50	2.80	3.10	3.20	3.30	3.30	3.30

Tab. 4.1: Comparison of the measured optical power  $P_{\text{det}}$  transmitted through a circular iris diaphragm with diameter  $2r_{\text{RXA}}$  (experimental setup is shown in Fig.4.2) with the simulated optical power  $P_{\text{sim}}$  according to Eq.(4.11) and Eq.(4.15) and experimental setup in Fig.4.2. Measurement error  $P_{\text{err}} = 10\%$  for  $2r_{\text{RXA}} \leq 2.0$  mm and  $P_{\text{err}} = 2\%$  otherwise.

$P_{\text{err}} = 2\%$  for larger settings. This difference is caused by the calibration method and construction of the diaphragm.

An engineering approach would not require more in-depth analysis of the geometrical attenuation expressions when two exact solutions have been introduced, but if further study reveals some of their interesting physical and mathematical aspects. In [31] we may find two approximations of the modified Bessel function  $I_0$ , which lead to two additional expressions of geometrical attenuation.

## 4.2 Derivation of approximative expressions

This section provides derivation of approximative analytical solution to exact geometrical loss expressions derived in the previous section. First, according to Equation (8.447-1) in [31] we can approximate the modified Bessel function  $I_0$  as

$$I_0(z) = \sum_{k=0}^{\infty} \frac{\left(\frac{z}{2}\right)^{2k+1}}{(k!)^2} \approx 1 + \frac{z^2}{4} + \frac{z^4}{64} + \frac{z^6}{2304} = \left(1 + \frac{z}{2} + \frac{z^2}{8}\right)^2 + \frac{z^6}{2304}. \quad (4.19)$$

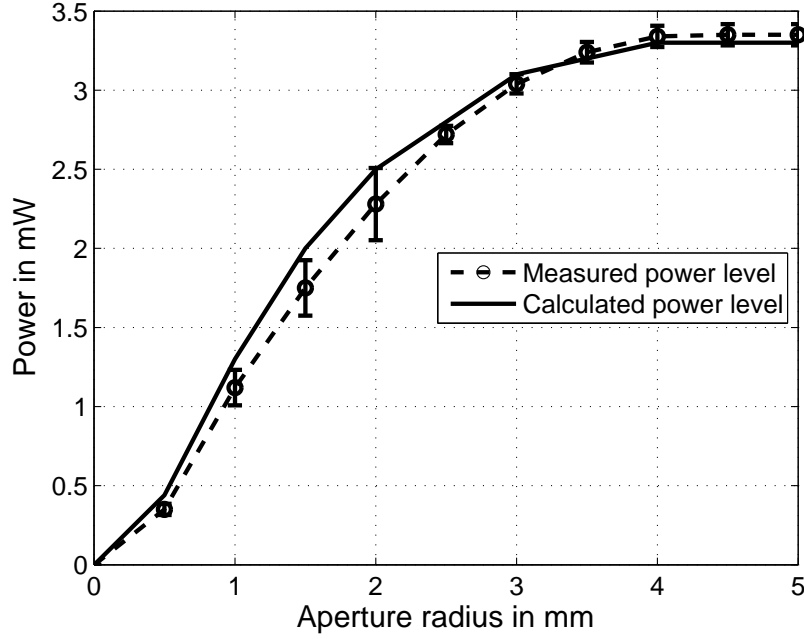


Fig. 4.3: Comparison of the measured optical power  $P_{\text{det}}$  transmitted through a circular iris diaphragm with diameter  $2r_{\text{RXA}}$  with the simulated power  $P_{\text{sim}}$  according to Eq.(4.11) and Eq. (4.15). Distance  $z$  between the laser diode and iris diaphragm was  $z = 0.2$  m, where beam half-widths were  $w_x = 1.72$  mm and  $w_y = 0.48$  mm and axial optical intensity  $I(0,0,z) = 2583$  W/m<sup>2</sup>. Diaphragm diameter  $2r_{\text{RXA}}$  was calibrated and adjustable in range  $2r_{\text{RXA}} \in < 0.5; 5 >$  mm with 0.5 mm step. Measurement error  $P_{\text{err}} = 10\%$  for  $2r_{\text{RXA}} \leq 2.0$  mm and  $P_{\text{err}} = 2\%$  otherwise.

Results of Eq.(4.19) are shown in Fig.4.4 for two, three and four terms and compared with the value of  $I_0$  used by MATLAB <sup>1</sup>. The calculation precision is determined by the number of terms included in our calculations. Fig.4.4 also shows that the higher is the number of terms used for the approximation, the wider is the range of applicability for certain precision. The highest value of the argument  $z$  achievable for different number of terms in order to maintain approximation precision higher than 1% is shown in Tab.4.2

Before validity of the geometrical attenuation approximation based on Eq. (4.19) is further discussed, another approximation approach will be introduced. That is based on an asymptotic approximation of the modified Bessel function  $I_0$  (for large

<sup>1</sup>Bessel function value computation in MATLAB is based on the definition of the Bessel function, which for  $I_0$  leads to the same formula as Eq.(4.19). Difference is in much higher number of terms used for calculations.

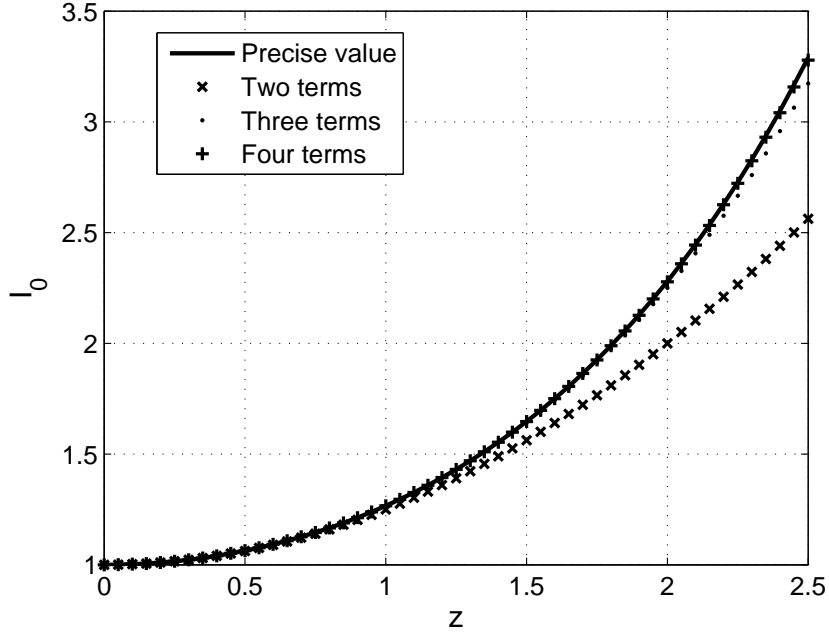


Fig. 4.4: Comparison of the precise value of modified Bessel function  $I_0$  calculated by MATLAB and its approximation given by two, three and four terms of eq.(4.19).

values of  $|z|$ ) by Eq. (8.451-5) in [31]

$$I_0(z) \approx \frac{\exp(z)}{\sqrt{2\pi z}}. \quad (4.20)$$

According to the definition and as Fig.4.5 shows, the approximation in Eq. (4.20) can be used for larger values of argument of modified Bessel function in Eq. (4.18), unlike the approximation in Eq. (4.19). The value of this function for  $z = 0$  is infinity and is minimal for  $z = 0.5$ , where  $I_0 = 0.93$ . When  $z > 1$ , the approximated value is constantly smaller than the precise value and the difference does not exceed 2%, which is acceptable compared to the measurement error.

Therefore, one may conclude that when the argument of  $I_0$  in Eq. (4.18) is  $z \leq 1$ , its approximation based on Eq. (4.19) containing first three terms can be used. For

No. of terms in Eq.(4.19)	$z_{\max}$
2	0.9
3	1.9
4	3.0

Tab. 4.2: Maximal range of argument  $z$  in Eq. (4.19) achievable for different number of approximation terms to maintain uncertainty below 1%.

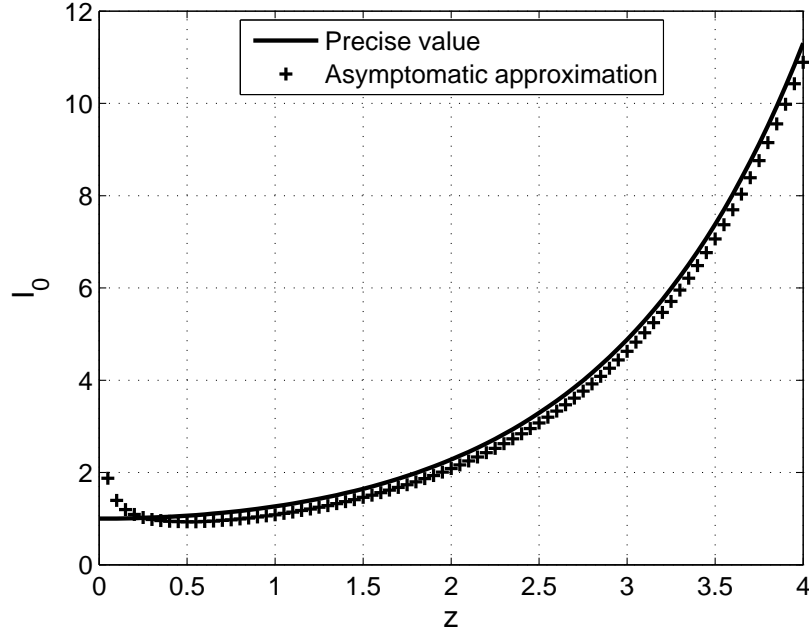


Fig. 4.5: Asymptotic approximation of modified Bessel function  $I_0$  according to Eq. (4.20).

larger values of argument, one may use expression (4.20). Now, final approximative expressions of geometrical attenuation  $\alpha_{\text{app}}$  are shown in the following text.

First, approximation of  $I_0$  in (4.18) by (4.19) yields (first) approximative expression for geometrical attenuation  $\alpha_{\text{app},1}$

$$\alpha_{\text{app},1} = \frac{2r_{\text{RXA}}^2}{w_x w_y} \left[ \int_0^1 \exp(-\alpha t) dt + \frac{\beta^2}{4} \int_0^1 t^2 \cdot \exp(-\alpha t) dt + \frac{\beta^4}{64} \int_0^1 t^4 \cdot \exp(-\alpha t) dt \right], \text{ for } u \leq 1 \quad (4.21)$$

where

$$\alpha = r_{\text{RXA}}^2 \frac{w_x^2 + w_y^2}{w_x^2 w_y^2}, \quad (4.22a)$$

$$\beta = r_{\text{RXA}}^2 \frac{w_x^2 - w_y^2}{w_x^2 w_y^2}, \quad (4.22b)$$

$$u = r_{\text{RXA}}^2 \frac{w_x^2 - w_y^2}{w_x^2 w_y^2} t, \quad (4.22c)$$

$$t = \left( \frac{\rho}{r_{\text{RXA}}} \right)^2. \quad (4.22d)$$

Second approximative expression is obtained by means of approximation of  $I_0$  in (4.18) by (4.20). This approach actually provides means of analytical solution. In order to effectively compute this integral, I recommend the backwards substitution (4.16) in (4.18) prior to the approximation as follows

$$\begin{aligned}
\alpha_{\text{app},2} &= \frac{4}{w_x w_y} \int_0^{r_{\text{RXA}}} \exp\left(-\rho^2 \frac{w_x^2 + w_y^2}{w_x^2 w_y^2}\right) I_0\left(\rho^2 \frac{w_x^2 - w_y^2}{w_x^2 w_y^2}\right) \rho d\rho = \\
&= \sqrt{\frac{8}{\pi(w_x^2 - w_y^2)}} \int_0^{r_{\text{RXA}}} \exp\left(-\rho^2 \frac{w_x^2 + w_y^2}{w_x^2 w_y^2}\right) \exp\left(\rho^2 \frac{w_x^2 - w_y^2}{w_x^2 w_y^2}\right) d\rho = \\
&= \sqrt{\frac{8}{\pi(w_x^2 - w_y^2)}} \int_0^{r_{\text{RXA}}} \exp\left[\rho^2 \left(\frac{w_x^2 - w_y^2}{w_x^2 w_y^2} - \frac{w_x^2 + w_y^2}{w_x^2 w_y^2}\right)\right] d\rho = \\
&= \sqrt{\frac{8}{\pi(w_x^2 - w_y^2)}} \int_0^{r_{\text{RXA}}} \exp\left[-\rho^2 \frac{2}{w_x^2}\right] d\rho.
\end{aligned} \tag{4.23}$$

Modification using Eq.(3.321-2) in [31] yields the (second) approximative expression of geometrical attenuation

$$\alpha_{\text{app},2} = \frac{w_x}{\sqrt{w_x^2 - w_y^2}} \operatorname{erf}\left(\sqrt{2} \frac{r_{\text{RXA}}}{w_x}\right), \text{ for } u > 1, \tag{4.24}$$

where  $\operatorname{erf}(\cdot)$  is the error function [31] and  $u$  is defined in (4.22c).

As can be easily shown, the simplification  $w_x = w_y = w$  of the Eq.(4.12) leads to a known calculation of the geometrical attenuation (4.25) of a circular Gaussian beam [20].

$$\alpha_{\text{geom,circ}} = 1 - \exp\left[-2 \frac{r_{\text{RXA}}^2}{w^2(z)}\right]. \tag{4.25}$$

### 4.3 Misalignment loss

The previous section describes the geometrical loss in terms of the change of the received optical power  $P_r$  as a function of the link distance (range)  $z$ . This section introduces and analyses two possible misalignment scenarios and their influence on the link performance; the (lateral) displacement  $\Delta$  between the relative position of TXA and RXA (shown in Fig.4.6) in the lateral direction and the angular deviation (tilt; pointing error)  $\gamma_t$  of TXA relative to RXA (cf. Fig.4.7). The main cause giving rise to the attenuation due to misalignment is non-uniform intensity distribution of the Gaussian beam. In case of a uniform beam distribution (e.g. using so-called ‘‘Top-Hat’’ beam), the received optical power would not change unless the misalignment is larger than beam dimensions. Other considered causes are the finite divergence  $\theta$  of the transmitted beam and finite FOV. In the first approximation it

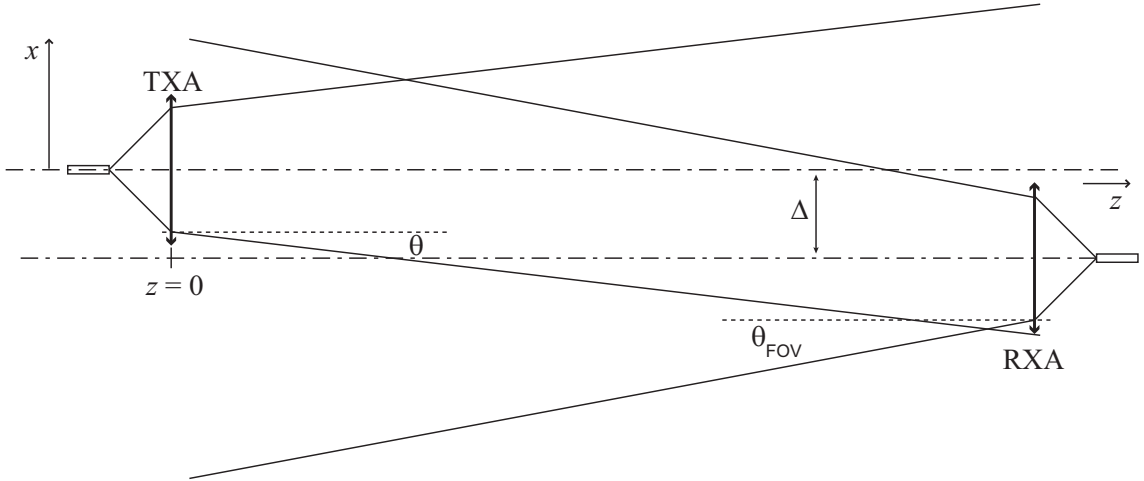


Fig. 4.6: To the explanation of lateral misalignment loss.  $\Delta$  represents the lateral misalignment and  $\theta$  and  $\theta_{\text{FOV}}$  stand for the divergence of the transmitter and field-of-view of the receiver, respectively.

would seem that the relation between lateral misalignment  $\Delta$  and tilt  $\gamma_t$  of TXA depending on the distance  $z$  is simply given by

$$\Delta = z \cdot \tan(\gamma_t). \quad (4.26)$$

However, the tilt, as well as the lateral displacement, give rise to an angular deviation of the beam spot at the focal plane of receiving lens, which, as discussed in Chapter 5, is critical in FSO links.

The change  $\Delta$  of the relative position of TXA and RXA in the lateral direction may occur either due to a random influence of the atmospheric conditions (e.g. wind [18] or beam wander) or due to mechanical misalignment caused by human error during link alignment. The dependency of the received optical power  $P_r$  on the deviation  $\Delta$  is often underestimated and may lead to severe misinterpretation of data. In data links this additional loss leads to decreased data rate and link availability. In the following text we therefore show the derivation of the received optical power  $P_r$  as a function of the distance  $z$  and the lateral misalignment (deviation)  $\Delta$  when the optical beam axis is not identical with the link axis considering an elliptically symmetrical Gaussian beam.

The derivation itself is based on the integration of the optical intensity distribution over RXA. Mathematically this situation is expressed in Cartesian coordinates as

$$P_r = \iint_{\Sigma_{\text{RXA}}} I(x, y, z) d\Sigma_{\text{RXA}}, \quad (4.27)$$

where  $I(x, y, z)$  represents the optical intensity distribution of the Gaussian beam in the receiver plane  $\Sigma_{\text{RXA}}$ .

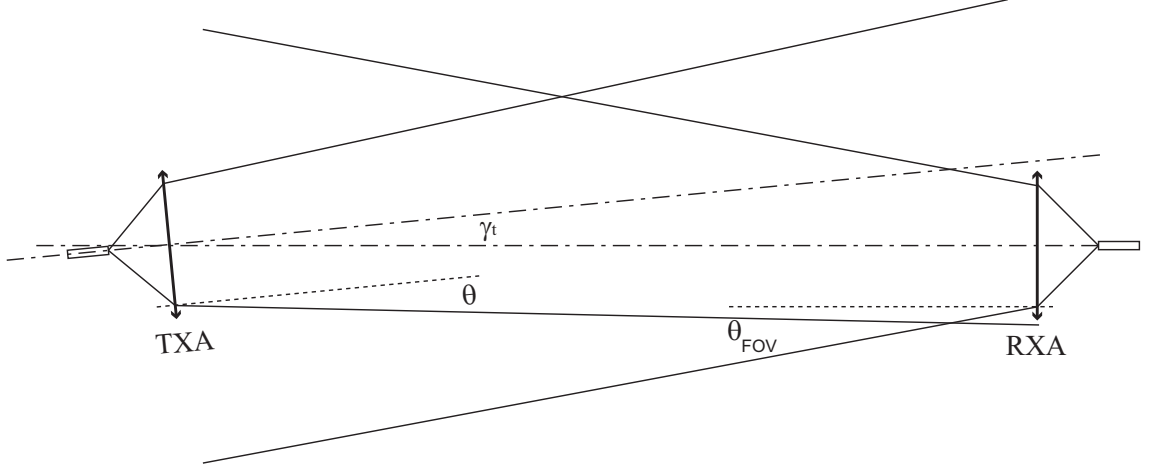


Fig. 4.7: To the explanation of angular misalignment attenuation loss.  $\gamma_t$  represents the angular misalignment of the transmitter and  $\theta$  and  $\theta_{\text{FOV}}$  stand for the divergence of the transmitter and FOV of the receiver, respectively.

First, let's assume only the case of circularly symmetrical beam, when only one (axial) parameter  $\Delta$  is sufficient to fully describe the lateral misalignment of the two terminals. In order to calculate integral in Eq. (4.27), we must define the integration limits

$$x \in < -r_{\text{RXA}}, r_{\text{RXA}} > \quad (4.28a)$$

$$y \in < \Delta - \sqrt{r_{\text{RXA}}^2 - x^2}, \Delta + \sqrt{r_{\text{RXA}}^2 - x^2} >. \quad (4.28b)$$

Now, for the power  $P_r$  of the beam misaligned by  $\Delta$  relative to RXA we write [20]

$$P_r = I(0, 0, z) \int_{-r_{\text{RXA}}}^{r_{\text{RXA}}} \int_{\Delta - \sqrt{r_{\text{RXA}}^2 - x^2}}^{\Delta + \sqrt{r_{\text{RXA}}^2 - x^2}} \exp \left[ -2 \frac{x^2 + y^2}{w^2(z)} \right] dx dy, \quad (4.29)$$

where  $w(z)$  is the beam radius in the receiver plane  $\Sigma_{\text{RXA}}$ .

The inner integral can be calculated using Equation (3.321-2) in [31]

$$\int_{\Delta - \sqrt{r_{\text{RXA}}^2 - x^2}}^{\Delta + \sqrt{r_{\text{RXA}}^2 - x^2}} \exp \left[ \frac{-2y^2}{w^2(z)} \right] dy = \frac{1}{2} \sqrt{\frac{\pi}{2}} w(z) \operatorname{erf} \left[ \frac{\sqrt{2}}{w(z)} y \right] \Big|_{\Delta - \sqrt{r_{\text{RXA}}^2 - x^2}}^{\Delta + \sqrt{r_{\text{RXA}}^2 - x^2}}. \quad (4.30)$$

Then Eq. (4.29) takes form

$$P_r = \sqrt{\frac{\pi}{2}} w(z) I(0, 0, z) \int_0^{r_{\text{RXA}}} \exp \left[ \frac{-2x^2}{w^2(z)} \right] \cdot \left\{ \operatorname{erf} \left[ \frac{\sqrt{2}}{w(z)} \left( \Delta + \sqrt{r_{\text{RXA}}^2 - x^2} \right) \right] - \operatorname{erf} \left[ \frac{\sqrt{2}}{w(z)} \left( \Delta - \sqrt{r_{\text{RXA}}^2 - x^2} \right) \right] \right\} dx. \quad (4.31)$$

And finally for the attenuation  $\alpha_{\text{mis,circ}}$  due to misalignments considering circular beam we may write [43]

$$\alpha_{\text{mis,circ}}(\Delta, z) = \sqrt{\frac{2}{\pi w^2(z)}} \int_0^{r_{\text{RXA}}} \exp\left[\frac{-2x^2}{w^2(z)}\right] \cdot \left\{ \operatorname{erf}\left[\frac{\sqrt{2}}{w(z)}\left(\Delta + \sqrt{r_{\text{RXA}}^2 - x^2}\right)\right] - \operatorname{erf}\left[\frac{\sqrt{2}}{w(z)}\left(\Delta - \sqrt{r_{\text{RXA}}^2 - x^2}\right)\right] \right\} dx. \quad (4.32)$$

After substitution  $t = x/r_{\text{RXA}}$  this equation simplifies to form

$$\alpha_{\text{mis,circ}}(\Delta, z) = \sqrt{\frac{2}{\pi}} \frac{r_{\text{RXA}}}{w(z)} \int_0^1 \exp\left[\frac{-2r_{\text{RXA}}^2 t^2}{w^2(z)}\right] \cdot \left\{ \operatorname{erf}\left[\frac{\sqrt{2}}{w(z)}\left(\Delta + r_{\text{RXA}}\sqrt{1-t^2}\right)\right] - \operatorname{erf}\left[\frac{\sqrt{2}}{w(z)}\left(\Delta - r_{\text{RXA}}\sqrt{1-t^2}\right)\right] \right\} dt \quad (4.33)$$

and can be solved by means of numerical integration methods.

However, in case of elliptically symmetrical beams the situation is more complex. One needs to distinguish between lateral displacement  $\Delta_x$  and  $\Delta_y$  in the  $x$  and  $y$  axis, respectively. For the integration, the optimal choice of integration limits in (4.27) is essential. Proposed integration limits are based on Fig.4.8

$$x \in \langle \Delta_x - r_{\text{RXA}}, \Delta_x + r_{\text{RXA}} \rangle \quad (4.34a)$$

$$y \in \langle \Delta_y - \sqrt{r_{\text{RXA}}^2 - x^2}, \Delta_y + \sqrt{r_{\text{RXA}}^2 - x^2} \rangle. \quad (4.34b)$$

Using integration limits in Eq. (4.34) in Eq. (4.27) yields

$$P_{\text{r}}(\Delta_x, \Delta_y, z) = I(0, 0, z) \int_{\Delta_x - r_{\text{RXA}}}^{\Delta_x + r_{\text{RXA}}} \exp\left[\frac{-2x^2}{w_x^2(z)}\right] \int_{\Delta_y - \sqrt{r_{\text{RXA}}^2 - x^2}}^{\Delta_y + \sqrt{r_{\text{RXA}}^2 - x^2}} \exp\left[\frac{-2y^2}{w_y^2(z)}\right] dy dx. \quad (4.35)$$

Let's denote the inner integral in (4.35)  $I_5$  and according to (3.321-2) in [31] one may write

$$I_5 = \int_{\Delta_y - \sqrt{r_{\text{RXA}}^2 - x^2}}^{\Delta_y + \sqrt{r_{\text{RXA}}^2 - x^2}} \exp\left[\frac{-2y^2}{w_y^2(z)}\right] dy = \sqrt{\frac{\pi}{8}} w_y \left\{ \operatorname{erf}\left[\frac{\sqrt{2}}{w_y}\left(\Delta_y + \sqrt{r_{\text{RXA}}^2 - x^2}\right)\right] - \operatorname{erf}\left[\frac{\sqrt{2}}{w_y}\left(\Delta_y - \sqrt{r_{\text{RXA}}^2 - x^2}\right)\right] \right\}. \quad (4.36)$$

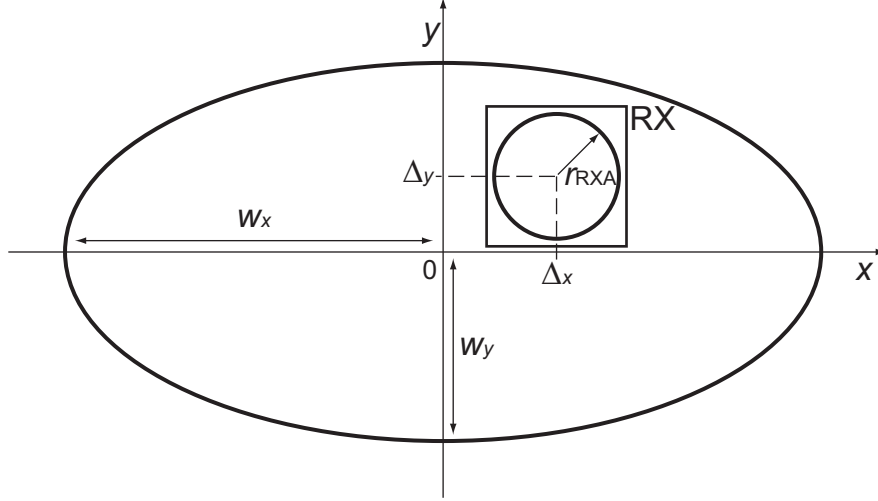


Fig. 4.8: Front view of the misaligned elliptical beam in the receiver plane  $\Sigma_{\text{RXA}}$ .  $\Delta_x$  and  $\Delta_y$  are displacements and  $w_y$  are the beam-widths in  $x$  and  $y$  axis, respectively, and  $r_{\text{RXA}}$  is the aperture radius of the receiver RX.

Finally, using (4.36) in (4.35) we may write for the lateral misalignment attenuation  $\alpha_{\text{mis,ellip}}$  considering the elliptical Gaussian beam

$$\alpha_{\text{mis,ellip}}(\Delta_x, \Delta_y, z) = \sqrt{\frac{2}{\pi w_x^2(z)}} \cdot \int_{\Delta_x - r_{\text{RXA}}}^{\Delta_x + r_{\text{RXA}}} \exp\left[\frac{-2x^2}{w_x^2(z)}\right] \left\{ \operatorname{erf}\left[\frac{\sqrt{2}}{w_y(z)}\left(\Delta_y + \sqrt{r_{\text{RXA}}^2 - x^2}\right)\right] - \operatorname{erf}\left[\frac{\sqrt{2}}{w_y(z)}\left(\Delta_y - \sqrt{r_{\text{RXA}}^2 - x^2}\right)\right] \right\} dx, \quad (4.37)$$

which is essentially a generalisation of Eq. (4.32) for elliptical beam.

Finally, due to angular misalignment of the receiver, the effective active area of RXA and the received optical power decreases with the cosine of the angle  $\gamma_r$  (cf. Fig.4.9) [20]. Again, the angular misalignment  $\gamma_r$  causes also the deviation of the beam spot in the focal plane of the receiving optics. Lateral displacement together with the beam angular displacement and the receiver tilt cover all main contributions to additional attenuation in FSO systems due to misalignments and hence improve the estimation of the FSO link budget.

## 4.4 Experimental Verification and Discussion

This section provides two experimental verifications of the simulated system performance. First experiment was aimed to compare results of the circular beam model

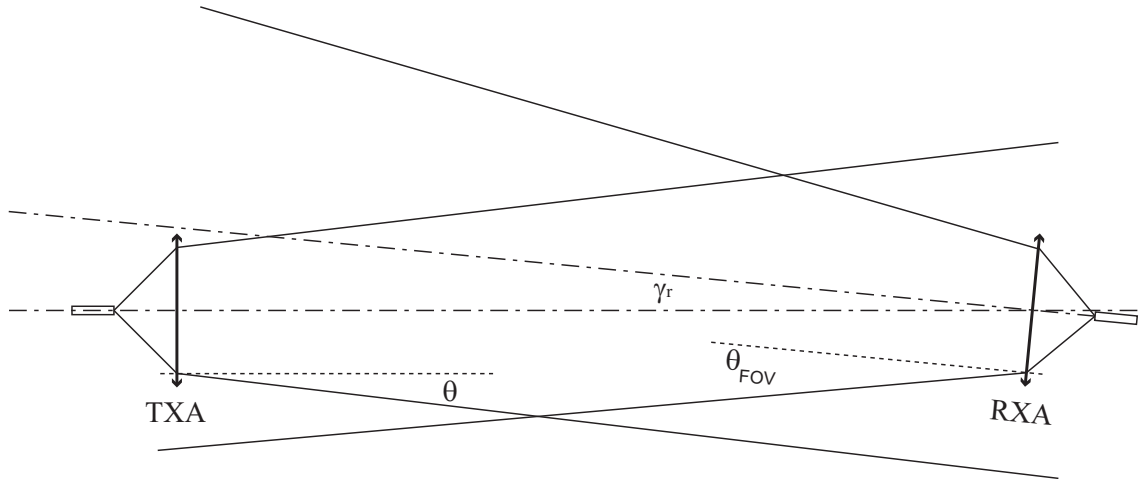


Fig. 4.9: To the explanation of RXA angular misalignment loss (pointing error).  $\gamma_r$  represents the angular misalignment of the transmitter and  $\theta$  and FOV stand for the divergence of the transmitter and field-of-view of the receiver, respectively.

with its model based on Eq. (4.25) and Eq. (4.32). The second experiment compares the elliptical beam geometrical loss according to Eq. (4.12) and Eq. (4.18).

At first we show the validity of Eq. (4.32) for various distance  $z$  and the change of the lateral distances of the optical axes  $\Delta$ . If we assume only the change of the distance between the transmitter aperture (TXA) and the receiver RXA and zero displacement  $\Delta$ , Eq. (4.32) simplifies to (4.25), which is compared with experiment in Fig. 4.10.

As was described above, the additional attenuation in case of lateral displacement increases. This dependency is shown in Fig.4.11, where dash-dotted line represents the estimation based on the assumption that the intensity decreases with the beam misalignment, but for simplicity it also assumes constant intensity distribution at the receiver aperture RXA. This assumption is valid only when the RXA radius  $r_{\text{RXA}}$  is much smaller than beam half-width  $w$ , as was also in this case. The dashed line shows the result of the analysis respecting the Gaussian variation of the optical intensity at RXA according to (4.32). Finally, the solid line joins the measured attenuation points (marked with a + sign).

The second part of the experiment is the validation of the elliptical beam attenuation model. The validity estimation of Eq. (4.12), Eq. (4.18), Eq. (4.21) and Eq. (4.24) is based on the measurement of the optical beam geometrical attenuation. Considering relatively small divergence of the transmitted beam, dependency of the attenuation on the aperture radius  $r_{\text{RXA}}$  instead of the dependency on the distance  $z$  was used. Fig.4.3 shows the results of the measurement and simulations according to exact models presented in Section 4.1. The confirmation of approximative model,

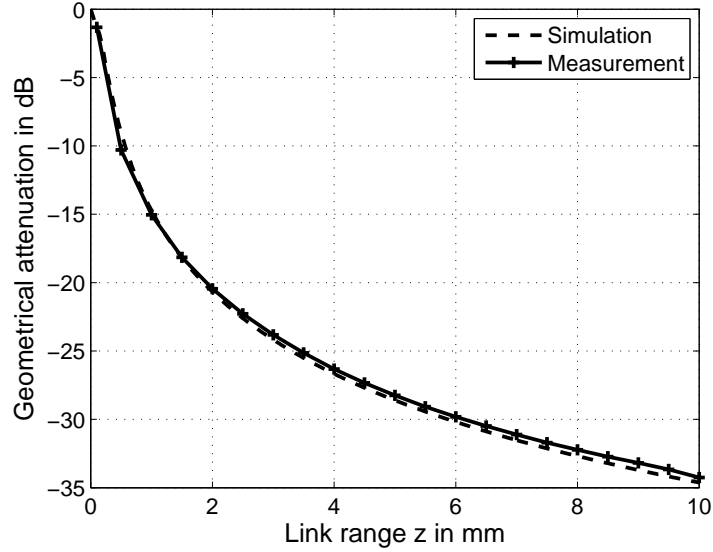


Fig. 4.10: Comparison of the measured geometrical attenuation of the beam at various distances between TXA and RXA and simulation according to (4.25).  $\theta = 0.2$  rad,  $r_{\text{RXA}} = 31.25$   $\mu\text{m}$ .

which consists of two equations, Eq. (4.21) and Eq. (4.24), was shown in [41].

Finally, to experimentally prove the validity of the proposed FSO link misalignment model (4.37) and to show the benefit of using an elliptically symmetrical optical beam, following experimental setup for optical power attenuation measurement of the optical beam for different lateral misalignments was proposed. The elliptically symmetrical Gaussian beam emerging from a semiconductor laser is pointed towards the circularly symmetrical RXA with a radius  $r_{\text{RXA}}$  and the optical power is then measured behind the aperture by an optical power meter. The aperture is then positioned along the major and minor axis of the Gaussian beam spot to measure the attenuation along the respective axes.

The comparison of the measured and simulated optical power attenuation for various lateral misalignments along the minor and major beam axis is shown in Fig. 4.12 and Fig. 4.14, respectively. To minimise the measurement error and to maximise liability of the measurement, we couldn't use the same beam geometry for measurement in both minor and major axis (cf. Fig.4.12 and Fig.4.14). In the first case, the major axis is positioned in the direction of  $y$  axis. Fig.4.12 shows that the lateral misalignment attenuation at the point  $\Delta_x = w_x/2$  is practically equal to the lateral misalignment attenuation at the point  $\Delta_y = w_y/2$  in Fig.4.14 and is approximately 2.5 dB. And since  $w_x < w_y$  I concluded that the sensitivity of the FSO link on the misalignment in the direction of major axis is smaller than in the

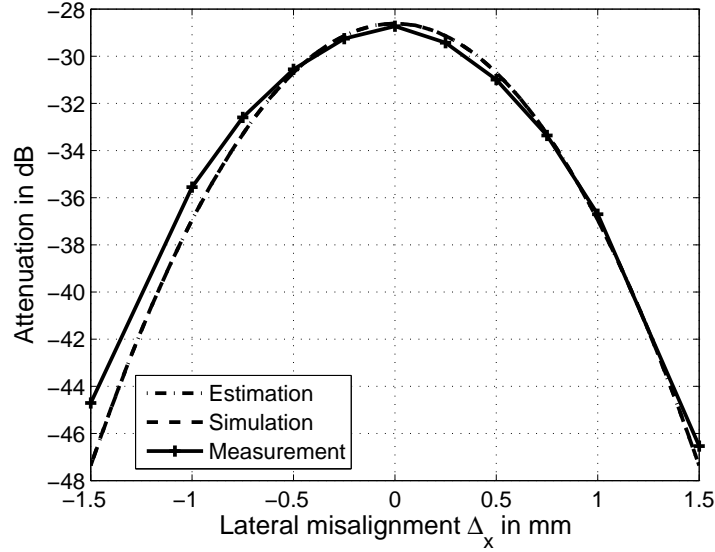


Fig. 4.11: Comparison of the measured lateral misalignment and geometrical attenuation of the beam at  $z = 5$  mm for various lateral displacement  $\Delta$  and simulation according to (4.32).  $\theta = 0.2$  rad,  $r_{\text{RXA}} = 31.25$   $\mu\text{m}$ . Estimation assumes constant intensity distribution over RXA, whereas simulation takes into account Gaussian distribution of the optical intensity. Due to relatively large ratio  $w/r_{\text{RXA}}$ , the estimation and simulation results overlap.

minor axis.

Now, depending on the application, one may optimise the beam pattern at the receiver to reduce the sensitivity of the system on various effects. One of the most significant effects deteriorating the FSO link performance in terms of lateral misalignment and pointing error is wind. It typically causes the sway of a building or a terminal stand on top of which the FSO terminal is installed (generally referred to as base motion). Let's assume two elementary scenarios; base motion in the direction parallel to the link and motion in the direction perpendicular to the link. The motion parallel to the link direction gives rise to angular misalignment of individual terminals, whereas base motion perpendicular to the link direction gives rise to lateral displacement. It was shown that the angular misalignment caused by base motion is more critical and is responsible for the link availability deterioration [44]. The pointing error caused by angular base motion can be minimised by using a wider beam (i.e. increase the beam divergence  $\theta$ ). Resulting decrease in optical power density at the receiver would decrease the link margin. However, using an elliptically symmetrical beam would efficiently decrease the sensitivity of the system on angular base motion while maintaining the optical power density at RXA.

As was reported in [40], anisotropic behaviour of the scintillation effects was

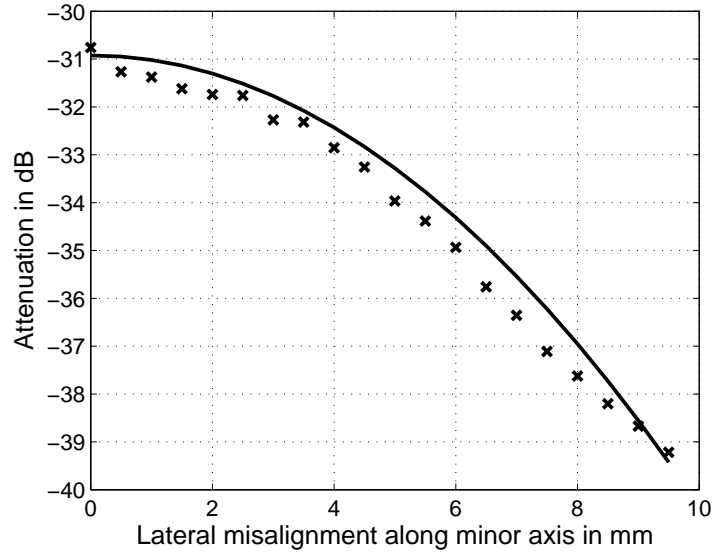


Fig. 4.12: Geometrical and lateral misalignment attenuation measured along the minor optical beam axis (x points) compared to the results of Eq.(4.37) (solid line). Simulation parameters:  $r_{\text{RXA}} = 0.25$  mm,  $w_x = 9.6$  mm,  $w_y = 32$  mm.

observed. This gives rise to higher relative variance of relative laser beam motion  $\sigma_C^2$  dependence on the variance of relative optical intensity  $\sigma_I^2$  in laser beam in vertical direction. Subsequently, the pointing and tracking error are significantly higher in the vertical direction.

Figure 4.16 demonstrates the system sensitivity on the lateral misalignments for increasing beam half-width. Changing half-width is represented by observing the

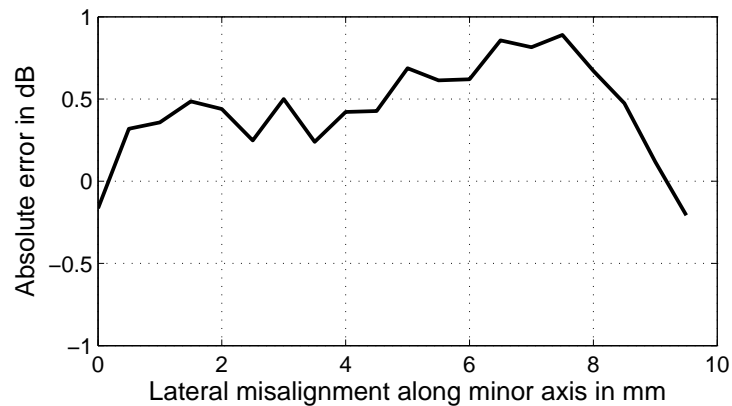


Fig. 4.13: Absolute difference between attenuation measured along the minor optical beam axis (Fig.4.12) and the results of Eq.(4.37). Simulation parameters:  $r_{\text{RXA}} = 0.25$  mm,  $w_x = 9.6$  mm,  $w_y = 32$  mm.

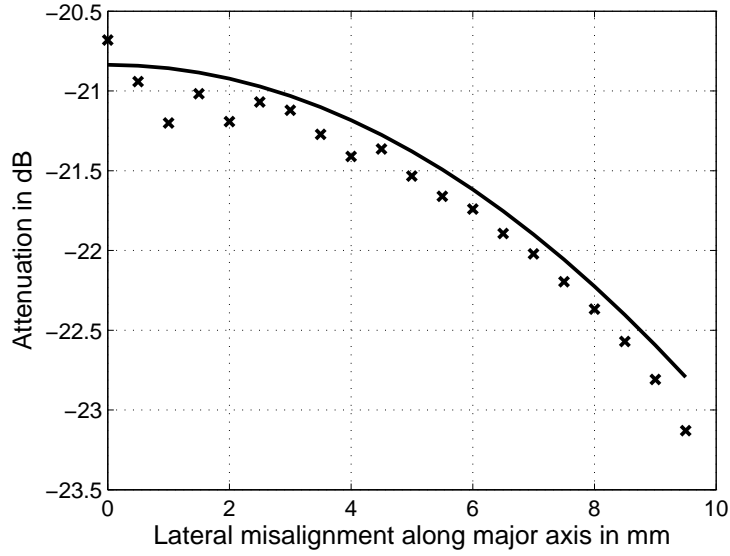


Fig. 4.14: Geometrical and lateral misalignment attenuation measured along the major optical beam axis (x points) compared to the results of Eq.(4.37) (solid line). Simulation parameters:  $r_{\text{RXA}} = 0.5$  mm,  $w_x = 6$  mm,  $w_y = 20$  mm.

system performance at various link distances  $L$  at a constant beam divergence angle, here set to  $\theta = 2^\circ$ . On one hand, increasing beam half-width deteriorates system performance in terms of the received optical power, but at the same time improves its reliability in terms of sensitivity to lateral misalignment. This compromise is also shown in Fig.4.17, where additional attenuation caused by transmitter tilt as a function of this angular misalignment  $\gamma_t$  is shown for various beam divergence angle

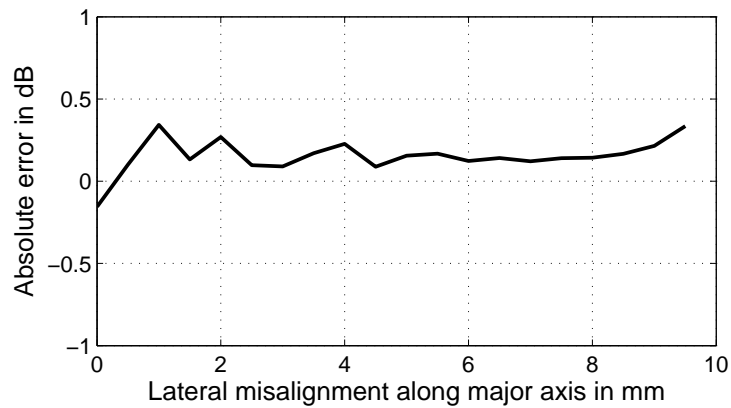


Fig. 4.15: Absolute difference (error) between attenuation measured along the major optical beam axis (Fig.4.14) and the results of Eq.(4.37). Simulation parameters:  $r_{\text{RXA}} = 0.5$  mm,  $w_x = 6$  mm,  $w_y = 20$  mm.

settings. Similarly to previous case, the wider is the beam (higher beam divergence  $\theta$ ), the lower is the beam sensitivity to misalignment or tilt of the respective transceiver. The relation between transmitter tilt  $\gamma_t$  and corresponding lateral misalignment  $\Delta$  described by Eq. 4.26 is also depicted in the same graph (for clarity on separate y axis).

Optimisation of the beam divergence for specific FSO link and specific application is always a trade-off between link budget analysis and system sensitivity to misalignments.

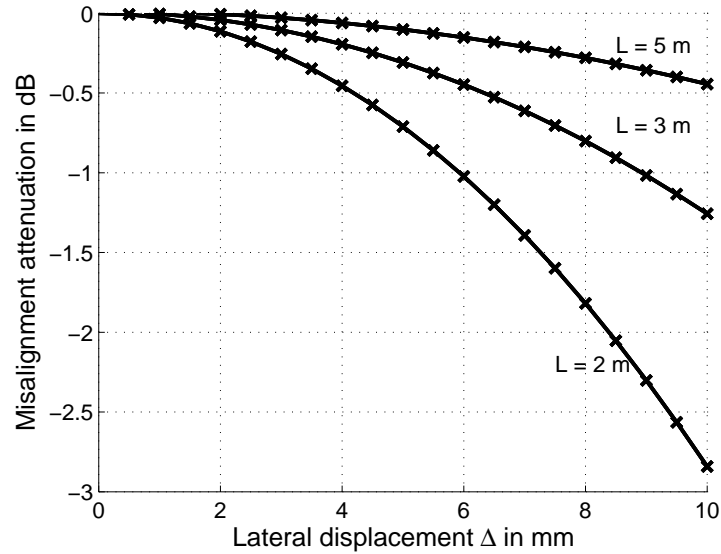


Fig. 4.16: Lateral misalignment attenuation as a function of lateral misalignment  $\Delta$  for various link distances  $L$  assuming constant circular Gaussian beam divergence angle  $\theta = 2^\circ$  and receiver radius  $r_{\text{RXA}} = 1$  mm.

Now, as long as the long distance FSO links are considered, one should prefer elliptically symmetrical Gaussian beams with the major beam axis situated vertically to decrease both the effects of scintillations and beam wandering as well as the effect of the building sway.

There are, however, special (dedicated) FSO links for short-range mobile applications, where horizontally symmetrical Gaussian beams may provide a great advantage. In case of Ground-to-Train FSO links reported in [45, 46], using the elliptical Gaussian beam increases the link coverage thanks to a more efficient optical power distribution in the horizontal plane.

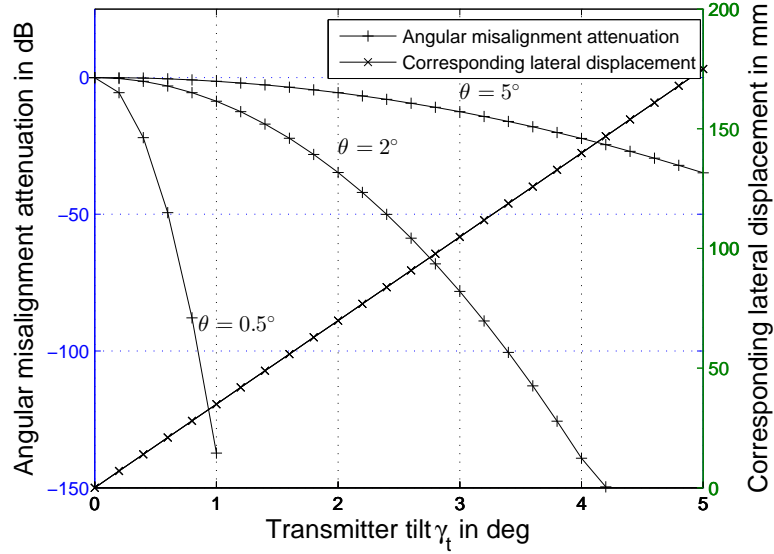


Fig. 4.17: Angular misalignment (pointing error) attenuation as a function of transmitter tilt  $\gamma_t$  assuming various Gaussian beam divergence angles  $\theta$  at constant link distance  $L = 2$  m and receiver radius  $r_{\text{RXA}} = 1$  mm.

## 4.5 Summary

In this chapter I introduced the derivation of the expressions describing the influence of the geometrical and misalignment (pointing) loss in FSO links. I distinguish between angular misalignment (pointing error) determined by the angle of misalignment  $\gamma_t$  of the transmitter and the lateral displacement  $\Delta_{x,y}$  of the relative lateral position of the transmitter and receiver in respective axis. The main contribution is that the expressions assume elliptically symmetrical Gaussian beam.

For the geometrical attenuation I derived and experimentally proven four expressions; two exact and two approximative. The two exact expressions provide accurate result, but they require numerical integration. In order to avoid numerical integration, I approximated the modified Bessel function  $I_0$  in one of the expressions by two methods; series expansion and asymptotic approximation. Each of these two approximative methods can be used within different boundaries, which I derived in the work, as well. Finally, I showed the range of applicability of the two approximative expressions of geometrical attenuation. The calculation can also be used to estimate losses during beam restriction by the TXA. This functionality was implemented in the beam diffraction model presented in the previous chapter. Now, we have a model that estimates impact of the elliptical Gaussian beam restriction by a circular aperture from the point of view of a wave optics (Chapter 3) as well as electromagnetic optics (Chapter 4).

Furthermore, I derived and experimentally verified the expression for the lateral misalignment attenuation. In the first approximation it can be used for calculation of the pointing error due to transmitter tilt provided the tilt angle  $\gamma_t$  is small enough to give rise to the lateral displacement much smaller than the link distance. The analysis assumes elliptically symmetrical Gaussian beam received by a circular aperture. Next challenge includes analysis of the misalignment tolerances, which is discussed in the next chapter for the case of all-optical receiver.

Results presented in this chapter have been also published in conference proceedings [20, 41, 43, 45] and impacted journals [40, 46].

## 5 ALL-OPTICAL FSO TRANSCEIVER

This chapter follows previous two analytical chapters and describes the development of the fully photonic transceiver. Fully photonic (or all-optical) transceiver stands for a design with no optoelectronic (O/E) and electro-optic (E/O) conversion, i.e. the input optical signal from the optical fiber (OF) is collimated and transmitted to the free-space by means of transmitter optics and on the other side is focused and coupled back into the OF. This approach eliminates distortion and delays introduced by the E/O and O/E conversions needed to transmit electrical signals by optical means; especially in applications, which are already based on the optical signals (e.g. fibre telecommunications), but also in applications, which use coherent properties of the optical beam to transmit time (or synchronisation pulses).

There are two main challenges (related to the transmitter and receiver optics, respectively) one has to face during the design phase of the all-optical wireless transceiver. First, the design of the optical part of the transmitter has been covered in numerous publications and is considered as well described. Some additional restrictions from the point of view of wave (diffraction) and electromagnetic optics (power attenuation) have also been discussed in previous chapters. However, the design becomes more complex when two or more optical beams need to be transmitted at the same time. If we, for reasons discussed later, want to avoid multi aperture transmitter concept, the system becomes more complex and requires a gentle approach.

Second, the receiving optical system is in general more complex and more sensitive to manufacturing defects and imperfections. Assuming that the adaptive optics (AO), which can be used to mitigate unwanted power fluctuations caused by turbulence effects [47] is not suitable for commercial applications for its cost at the moment, one had to come up with an effective solution to laser beam coupling from large aperture FSO receiver to a single-mode (SM) OF.

The following chapter shows the synthesis of the transmitter optics design for dual-wavelength all-optical single-aperture (DAS) FSO transmitter followed by the synthesis of the all-optical receiver for OWC.

### 5.1 Dual-wavelength single-aperture transmitter

The concept of dual-wavelength FSO transmitter was developed mainly for two reasons. First, long-range FSO links needed a precise position stabilisation requiring a beacon signal at different wavelength (or carrier frequency) than the main signal wavelength. Common concept used  $\lambda_1 = 1550$  nm for data transmission and  $\lambda_2 = 850$  nm as the beacon. Moreover, in testing FSO links these two wavelengths

were used to compare influence of various atmospheric effects on either of these wavelengths. Due to lack of dual-wavelength source, the transmitter assembly always consisted out of two individual (separated) transmitters, one for each signal.

Multi aperture approach as in Fig.1.3 was shown to be unsuitable for reasons mentioned earlier in the Chapter 1. On the other hand, effective merging of two or multiple optical beams of different wavelengths into a single beam is a specific task due to various polarisation and wave effects influencing either of the wavelengths differently. One approach involves using a bulk non-polarising beamsplitter which can efficiently combine both beams in the free-space. The main drawback of using bulk optics is that it would not solve the mechanical instability issues. Also, since the input beam comes coupled in an optical fibre, it is more straightforward to use a fibre-optical beamsplitter. Therefore, commercially available wavelength-division multiplexers (WDM) were used in first prototypes of DAS FSO transmitters.

### 5.1.1 WDM-based DAS

Fibre-optic WDM components are available in many different variations based on the combination of working wavelengths (e.g 980/1550 or 1310/1550), fibre core diameter (e.g. SM or MM) and connectors (e.g. FC/PC, FC/APC or SC/PC). Dense WDM (DWDM), which serves to merge beams within a single telecommunication band, e.g. C or L band, with small wavelength difference will not be discussed. Due to application requirements on SM fibre and high reliability of the system, combination of SM fibre type WDM with FC/APC connectors was used in order to mitigate unwanted reflections at the connection points. Also, in order to protect the laser sources, WDM was equipped with optical isolators at its inputs.

Fig.5.1 shows the schematic of the WDM-based DAS transmitter, where on the left-hand side there are two laser optical sources for each working wavelength connected by FC/APC connectors with optical isolator (OI). The OI output is then connected by FC/APC connectors to WDM, input of which is used as the final fibre. The output beam from final fibre is then collimated and transmitted to free-space. In the upper branch of the Fig.5.1, optical fibre SM800-5.6-125 was used, while in the lower branch, optical fibre SM980-5.8-125 was used due to difference in the working wavelengths.

Due to physical constraints, the fibre-optic WDM with inputs at  $\lambda_1 = 1550$  nm and  $\lambda_2 = 850$  nm cannot be manufactured. The reason for this is the difference in wavelengths which is nearly in the order of two, which prevents a single-mode operation of both beams inside a cylindrical waveguide. The most suitable and commercially available WDM is for the wavelength combination 980 and 1550 nm (e.g. from Newport Corporation [48], Thorlabs GmbH [49] or OZ Optics Ltd. [50]).

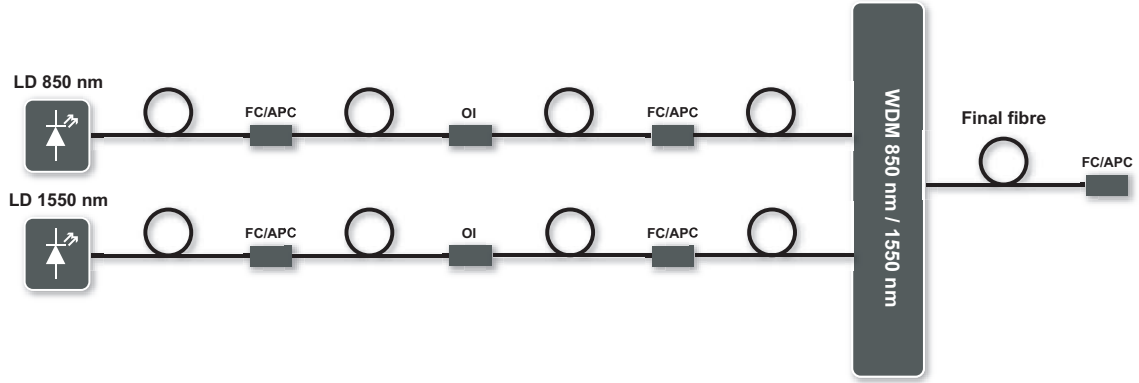


Fig. 5.1: Dual-wavelength all-optical single-aperture transmitter. LD – laser diode, OI – optical isolator. Detailed specifications are shown in Chapter A.

The wavelength incompatibility in the 980 nm branch, when we working with 850 nm laser, gives rise to the fluctuation of the optical power at the end of the fibre in the order of 10 to 20%. This output power fluctuation is caused by mode instability when the optical beam doesn't propagate in a single-mode operation, but it's energy is redistributed to higher modes and to cladding modes [51]. Hence, the power instability ruled out using the WDM from the DWAOSA transmitter design for 850/1550 wavelengths. To overcome these power fluctuations, one would need to use a fibre with a smaller mode field diameter (MFD), which would increase the attenuation in the lower branch in Fig.5.1.

### 5.1.2 POF-based DAS

This section discusses possible use of plastic OF (POF) in FSO systems for beam shaping. As was shown in previous chapters, optical intensity distribution of the beam emerging from a laser source, or an OF, can be approximated by the Gaussian beam. Recent studies show how to use other types of the beams, e.g. Top-Hat [52] or orbital angular momentum beams [53]. During experimentation with the WDM-based DAS final fibre, an interesting feature usable in FSO system was observed when POF was connected to the output of the final fibre. The optical intensity distribution of the POF output beam (Fig. 5.2) when excited by a SM optical beam at 850 nm was no longer a single Gaussian beam [54]. The reason for this is in a large core of POF (core diameter is up to 1 mm), which allows millions of modes to be excited within its volume. The envelope of all the modes (beam cross-sections are shown in Fig. 5.2 on the right and on the bottom) were nearly Top-Hat and the beam was called “quasi-Top-Hat”.

There are two main drawbacks in the practical use of the POF in transmitters for

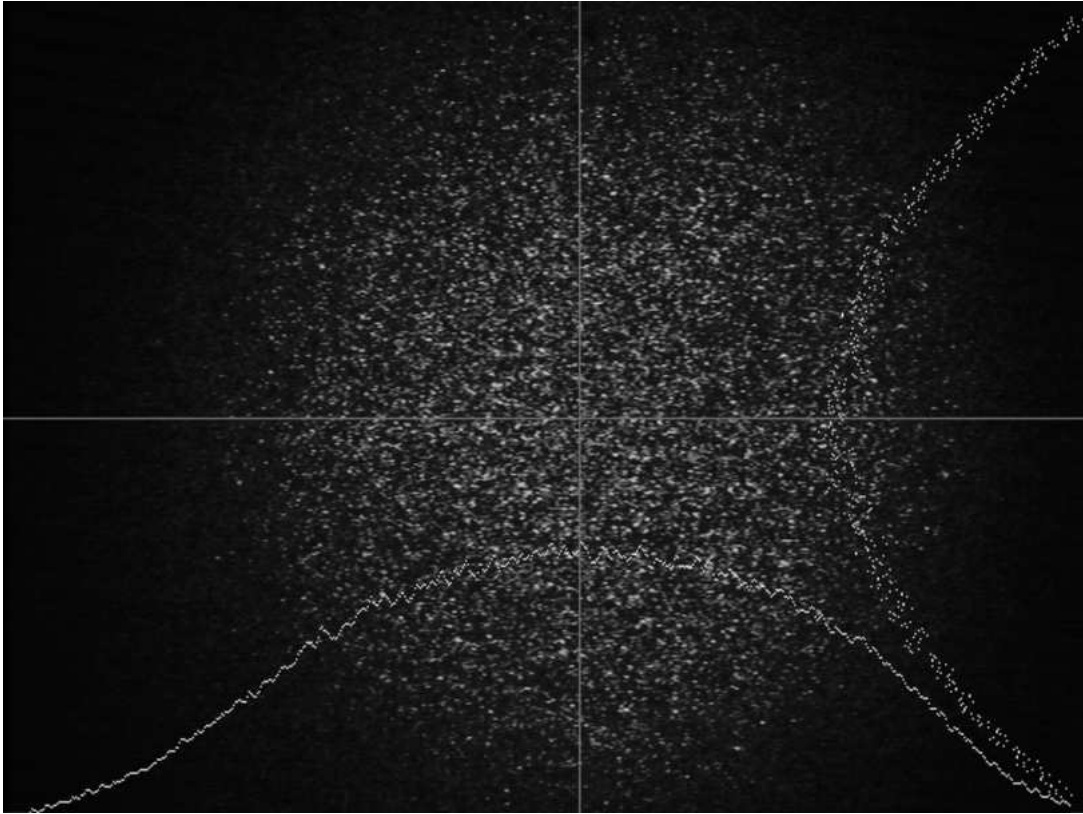


Fig. 5.2: Optical intensity distribution at the end of POF excited by laser diode with  $\lambda = 850$  nm. Cross-sections of the beam pattern, shown in the right and lower part of the figure, demonstrate the “quasi-Top-Hat” pattern.

FSO. First, the material of the POF core is poly(methyl methacrylate) (PMMA), which in NIR region, where the FSO systems operate, has attenuation too high for any practical use ( $10^3$  up to  $10^6$  dB/km [51]). However, commercially available solutions provide acceptable attenuation (up to hundreds of dB/km) for perfluorinated (PF) POF, which is feasible for applications in DAS, where only several metres of fibre are required to achieve the “quasi-Top-Hat” intensity distribution.

Second drawback in POF-based DAS according Fig. 5.3 is modal instability of the 850 nm signal which gives rise to dynamic modal instability also at the output of the PF-POF [54].

Following text discusses a possible solution to the output power instability of the final fibre based on dual-core (DC) OF combining two different optical fibres – SM800-5.6-125 for 850 nm and SM980-5.8-125 for 1550 nm.

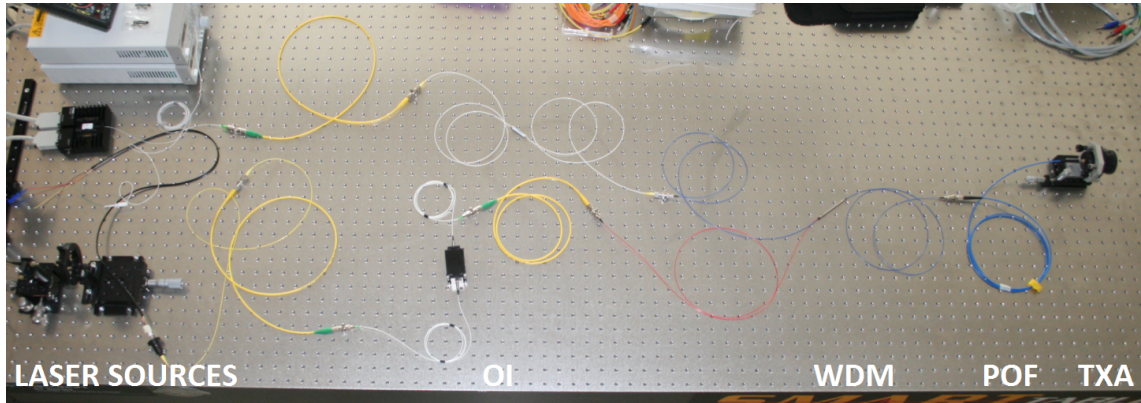


Fig. 5.3: Prototype of the testing FSO link transmitter using the fibre WDM and POF final fibre. Two laser sources (1550 nm on the top and 850 nm on the bottom) are connected via optical isolators (OI) to the inputs of WDM. WDM output is coupled using POF to the collimating lens (TXA) from which both beams are transmitted to the free-space. The three yellow fibres are fibre patch cables, which solve the connector compatibility problem. They are equipped with FC/PC connector on one side and FC/APC on the other side.

### 5.1.3 Dual-core fibre-based DAS

DC OF consists of two individual fibres (SM800-5.6-125 for 850 nm and SM980-5.8-125 for 1550 nm), cores and claddings of which are stripped down at the output side and molded together into a single jacket. They are used nowadays in many applications, e.g. sensing [55] and gain flattening [56] and their performance has been studied [57, 58]. In the transmitter part of the proposed DAS terminal, similar concept was adopted in order to virtually merge both optical beams. Custom-made DC OF was manufactured for this purpose. The cross-section of the DC OF is shown in Fig.5.4. Cores of the OFs are separated by only 125  $\mu\text{m}$  distance, which allows us to use a single FC/APC connector at the output of the system, which is then collimated by a single lens to the free-space. This approach increases reliability of the whole system by reducing several degrees of freedom compared to the situation with two individual transmitters. If cores are aligned properly in the jacket, both beams propagate in the same physical channel. Also, due to stable position of the cores inside the final fibre, there is no need for alignment of the relative pointing of the beams. The complete schematics of the DAS FSO transmitter is shown in Fig.5.5. On the left-hand side, there are two external FC/APC inputs used when signals are coupled from an external source, e.g. when the terminal is used as an FSO bridge for existing fibre-based network, or when transmitting LDs are located outside the terminal (when controlled conditions are required). The terminal is equipped also

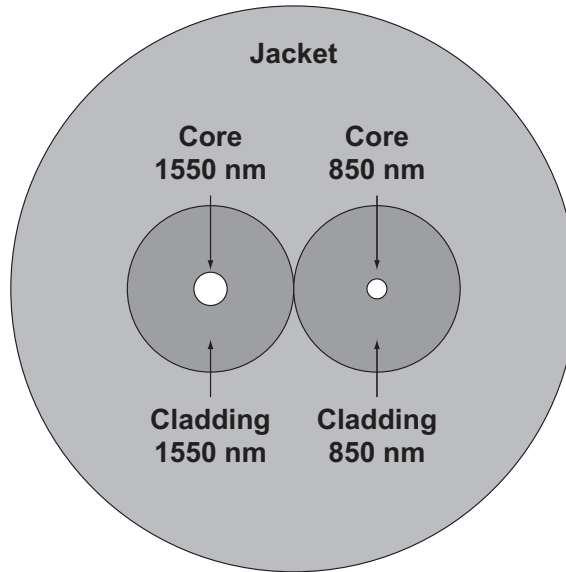


Fig. 5.4: Cross-section of the dual core OF. Distance between centre of the cores is  $125\mu\text{m}$ . Not to scale.

with two internal pigtailed LDs, which are via OI connected in each branch (850 and 1550) to the SM fibre coupler, which merges optical signal generated from the internal source with the signal coupled via external input to the respective input of the custom-made DC final fibre.

Output of the DC OF is fitted with FC/PC optical connector at the end of a lens tube with diameter  $D_{\text{TxA}} = 50 \text{ mm}$  for testing FSO links and  $D_{\text{TxA}} = 25 \text{ mm}$  for data links. In order to collimate the optical beam effectively to the free-space, i.e. not to restrict the beam due to attenuation and at the same time to use as much of the lens surface, the f-number  $f\#$  of the optical system should fit the inverse of the double numerical aperture (NA) of the final fibre. F-number is defined as the ratio between lens focal length  $f$  and its diameter  $D$ . It is customary to express f-number preceded by  $f/$  (contraction of the expression “ $f/D$ ”).

Different lens diameters for data and testing links are due to fact that testing FSO links are simplex, therefore due to lack of the receiving part, there is enough room for larger aperture, which produces larger beam, which is less sensitive to some non-standard effects discussed later (e.g. raindrops on the terminal cover window).

In practice, spherical lenses always show some aberrations when an image is formed. The most critical aberrations encountered in FSO systems are spherical and chromatic aberration. The spherical aberration occurs when the beams parallel but not identical to the optical axis are focused not to the same point as the beams close to the optical axis. Chromatic aberration, on the other hand, occurs due to chromatic dispersion in the material when beams of different wavelengths are

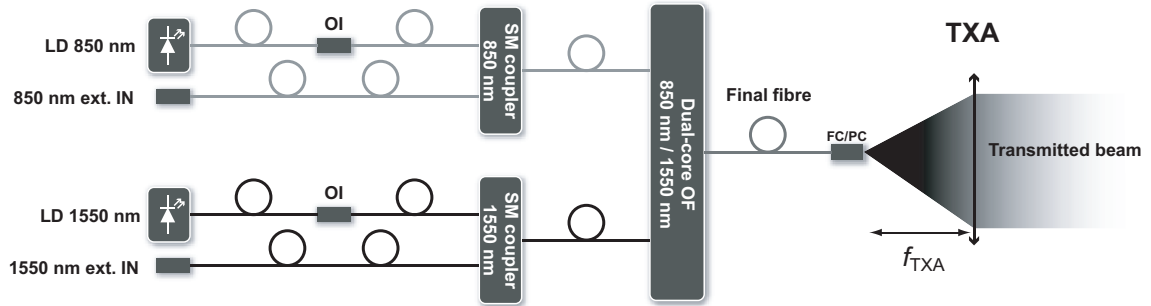


Fig. 5.5: Schematics of the dual-wavelength all-optical single-aperture (DAS) FSO transmitter. Two external inputs and two internal laser diodes (LD) with optical isolator (OI) are in each branch of SM fibre coupler connected to the respective input of a dual-core (DC) final fibre. Output optical beam emerging from the output of the final fibre is coupled to the free-space by the plano-convex lens (TXA) with focal length  $f_{\text{TXA}}$ . Light gray colour indicates SM OF SM800-5.6-125 for 850 nm, black colour indicates SM OF SM980-5.8-125 for 1550 nm and dark gray colour represents the DC OF. Unless otherwise stated, all optical connectors are FC/APC type.

focused to different points at the optical axis. The chromatic aberration is critical mainly when the optical system transmits more than a single wavelength (usually FSO systems work with monochromatic light). In order to reduce the effects of these aberrations in FSO systems, achromatic lenses (or achromats) are used to minimise the chromatic aberration while at the same time to reduce the spherical aberration. Achromats consist usually out of two or three spherical lenses made out of different materials to compensate for the aberrations. Together with the  $f\#$  and aberration performance of the collimating lens, anti-reflection coating is an important feature, which reduces unwanted background noise, mainly in the VIS part of the EM spectrum.

The optomechanical assembly (OMA) of the transmitting optical system should allow change of the relative distance between the final fibre output connector and the collimating lens in order to change the beam divergence angle  $\theta$ . Moreover, it should allow for the beam steering and positioning in order to point the beam towards the receiver as precisely as possible. Again, the larger the beam spot at the receiver side, the lower is turbulence-induced power fluctuation, but also the lower is the received optical power. For long-range FSO links, the transmitted power must

be increased. The proposed fibre-based FSO terminal has yet another advantage in the possibility of using the erbium-doped fibre amplifier (EDFA), which can increase the output optical power by up to 30 dB [10].

## 5.2 All-optical receiver: optomechanical design

Optomechanical part of the receiver serves for focusing the received optical beam to the active area of the photosensitive detector or, in our case, for coupling into OF. The critical system requirements include radius  $r_{\text{RXA}}$  of the receiver aperture (RXA), half-angle  $\theta_{\text{FOV}}$  of field of view (FOV), operating wavelength  $\lambda$ , effective focal length (EFL), f-number  $f\#$  of the receiving lens, core diameter and acceptance angle of the fibre and others [10]. This section presents considerations and requirements on the OMA RX design used for optical beam coupling from free-space to a SM OF at  $\lambda = 1550$  nm.

### 5.2.1 Telescope selection

The size (diameter) of the RXA should be as large as possible in order to reduce turbulence effects by means of aperture averaging [9], to compensate for geometrical attenuation, lateral displacement and pointing errors (discussed in previous chapter). For smaller RXA sizes and for commercial applications, refractive systems provide practical solution in terms of cost and performance. Although Fresnel lenses are used for RXA diameters up to tens of centimetres, due to their poor performance in terms of precision, reflective systems are generally used for dedicated, precise, scientific, long-range or satellite FSO links. These can be based on several telescope architectures used in astronomy. The most common receiver telescope architecture for OWC is Cassegrain system with its two modifications by Schmidt (SCT) and Maksutov (MCT). Due to all-spherical design of MCT, the overall image quality is usually higher than of SCT. SCT is more complex and more expensive than MCT, but provides light-weight solution in smaller dimensions. The weak point of SCT and MCT is the obscuration of the beam by the secondary mirror. This is generally smaller for the MCT due to higher  $f\#$  of the primary mirror. The obscuration is avoided with off-axis telescope designs. For its light-weight, compact size and relative good performance in terms of aberrations, SCT was proposed as viable solution for all-optical FSO receiver.

The telescope itself can be afocal ( $f = \infty$ ), when a collimated beam is generated at its output, or focal, by adjusting the primary mirror position. Afocal setup can be used for a beam expander or for a single-aperture transceiver design, which

facilitates the incorporation of beam-matching optics [10]. For fibre-coupling applications, focal mode of operation with  $f\# = f/10$  is assumed in the following text, which is achievable with commercially available telescopes for astronomical observation (at price of hundreds EUR). Telescope itself cannot be used for coupling the received optical beam into a SM fibre due to fibre's low acceptance angle. Therefore, following subsection introduces and summarises fibre-coupling possibilities usable in the receiver.

## 5.2.2 Fibre-coupling elements

In order to couple optical beam from free-space into a SM fibre [59], there are several commercially available solutions:

- Free-space to fibre coupler (e.g. KT110 from Thorlabs)
- Aspherical lens
- Fibre-optic collimator
- Ball lens
- GRIN lens

The first solution provides a complete solution, but lacks the flexibility needed in the development process. However, it is good to get accustomed with the practical aspects of fibre-coupling applications.

Now, aspherical lens shape reduces or even eliminates the spherical aberration, which makes it good for fibre-coupling applications. However, it would require very precise lens positioning relative to the fibre-end to focus the light in the fibre core of only several micrometres in diameter. This can be solved by using a fibre-optic collimator, where the lens comes adjusted from the factory and the fibre is simply connected to the other side of the collimator. The collimator requires collimated beam at its input and since it is available in diameters up to 1 inch (25.4 mm) it is not usable in the telescope.

Ball lens is a spherical lens usually with a relatively high refractive index  $n \approx 2$  [60]. When the fibre end is positioned at its focal point, the light is coupled in the fibre. Advantage of the ball lens is that it can be glued to the fibre end and serve as a collimator [61], which is used in also in fibre-optic connectors for harsh environments and military applications (HMA connector).

Finally, the GRIN lens offers an alternative to the ball lens in fibre-coupling applications. It is a cylindrical component with the refractive index  $n$  changing in the radial direction from the optical axis. This change is defined by gradient constant  $k$  ( $[k] = \text{mm}^{-1}$ ). Its dimensionless parameter called "pitch" is defined by a full sinusoidal path of an optical beam as shown in Fig. 5.6 [62]. For fibre-coupling applications, the GRIN lens with pitch  $p \approx 0.25$  are used and are available already

pigtailed to an OF. Due to this fact and based on the price, the GRIN lens was chosen as the final fibre-coupling element in the RX OMA design. However, size of a GRIN is only approx. 1.8 mm in diameter and the diameter of its active area  $D_{\text{GRIN}} = 0.5$  mm. Therefore, additional optical element between the telescope and the GRIN lens is required.

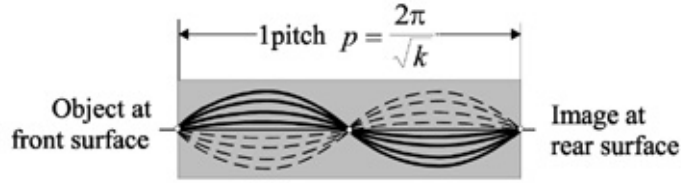


Fig. 5.6: Schematic representation of the optical ray propagation in a GRIN lens exactly one “pitch”  $p$  long [62] and the definition of the pitch  $p$ .

### 5.2.3 Final RX OMA design

Previous two subsections introduced two main parts of OMA of the proposed all-optical RX; Cassegrain (or Schmidt-Cassegrain) telescope in focal mode used to collect as much beam optical power from the free-space and GRIN lens for its coupling into SM OF. In order to collimate convergent beam at the output of the telescope for the GRIN lens, an aspherical lens can be used. Cassegrain telescope with aspherical lens form a Keplerian telescope. The schematics of the proposed OMA RX is shown in Fig. 5.7.

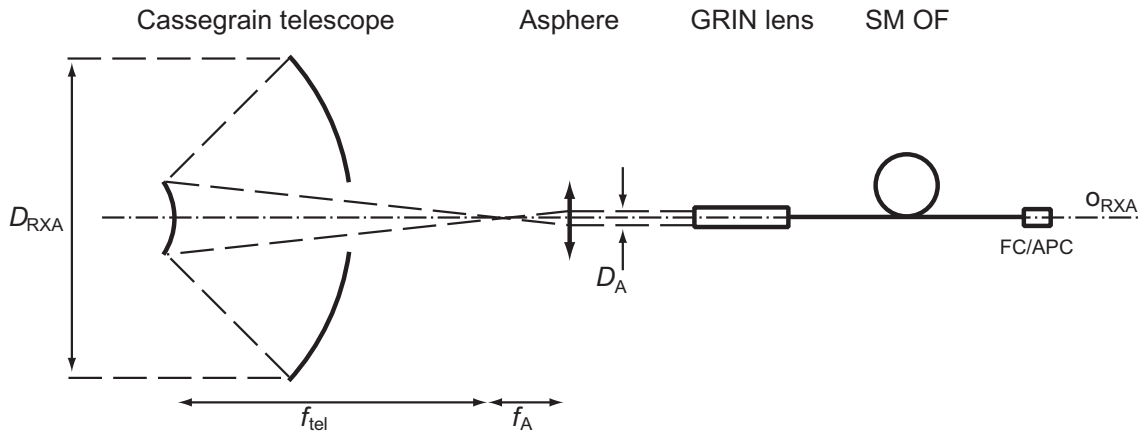


Fig. 5.7: Schematics of the proposed OMA RX design.  $D_{\text{RXA}}$  and  $D_{\text{A}}$  stand for the Keplerian telescope diameter and the beam diameter at the output of the asphere, respectively,  $f_{\text{tel}}$  and  $f_{\text{A}}$  stand for the telescope and collimating asphere diameter, respectively,  $O_{\text{RXA}}$  represents the OMA optical axis. Not to scale.

The length  $l_{\text{KT}}$  of a Keplerian telescope is

$$l_{\text{KT}} = f_{\text{tel}} + f_{\text{A}}, \quad (5.1)$$

where  $f_{\text{tel}}$  and  $f_{\text{A}}$  are focal lengths of the telescope and asphere, respectively. The angular magnification  $M_{\text{a}}$  of the Keplerian telescope, defined as the negative ratio of the focal length  $f_{\text{tel}}$  to  $f_{\text{A}}$ , is essential for the estimation of the beam diameter  $D_{\text{A}}$  at its output, which should not exceed size of the active area of the GRIN lens  $D_{\text{GRIN}}$ . The beam diameter  $D_{\text{A}}$  is

$$D_{\text{A}} = f_{\text{A}} \frac{D_{\text{RXA}}}{f_{\text{tel}}}, \quad (5.2)$$

which will be derived later together with  $M_{\text{a}}$ .

In order to meet the requirement  $D_{\text{A}} \leq D_{\text{GRIN}}$ , the focal length  $f_{\text{A}}$  of the asphere must fulfill requirement

$$f_{\text{A}} \leq D_{\text{GRIN}} \frac{f_{\text{tel}}}{D_{\text{RXA}}}. \quad (5.3)$$

Assuming commercially available Cassegrain telescope with  $f_{\text{tel}} = 1250$  mm and  $D_{\text{RXA}} = 125$  mm

$$f_{\text{A}} \leq 0.5 \frac{1250}{125} = 5 \text{ mm}, \quad (5.4)$$

which narrows the selection down to aspheres with focal length  $f_{\text{A}} = 4.50$  mm, which are commercially available (e.g. Thorlabs 355230-C or Newport 5722-H-C), typically with numerical aperture  $\text{NA} \approx 0.5$ . In that case the beam diameter at the input of the GRIN lens is

$$D_{\text{A}} = f_{\text{A}} \frac{D_{\text{RXA}}}{f_{\text{tel}}} = 4.51 \frac{125}{1250} = 0.451 \text{ mm} \leq D_{\text{GRIN}}, \quad (5.5)$$

which satisfies the requirement in Eq. (5.3).

There is an alternative to the asphere as coupling element using a bi-concave lens to form a Galileian telescope, instead of the Keplerian type. However, there is no affordable and commercially available bi-concave lens meeting the focal length restriction discussed above.

## 5.2.4 OMA alignment tolerances

Relatively small diameter of the optical fibre core poses strict requirements on the alignment tolerances of the whole system. The alignment tolerance of a single lens is proportional to the tolerable focal spot displacement in the perpendicular plane (OF core radius  $r_{\text{OF}}$  in this case) and inversely proportional to its focal length  $f$ . The angular magnification of the optical system gives rise to multiplication of the

<b>Telescope</b>	
Type	Schmidt-Cassegrain
Diameter $D_{\text{RXA}}$	125 mm
Focal length $f_{\text{tel}}$	1250 mm
Primary mirror f-number f#	f/2
Secondary mirror f-number f#	f/20
Telescope f-number f#	f/10
<b>Collimating lens</b>	
Type	Aspheric lens
Model	Thorlabs 355230-C
Focal length $f_{\text{A}}$	4.51 mm
Numerical aperture NA	0.55
<b>Fibre-coupling element</b>	
Type	GRIN lens (SM pigtailed)
Model	50-1550A-APC
Active area diameter $D_{\text{GRIN}}$	0.5 mm
Central wavelength	1550 nm
Beam diameter	0.5 mm
Beam divergence $\text{FOV}_{\text{GRIN}}$	0.25°
Insertion loss	<0.1 dB

Tab. 5.1: Specifications of the all-optical RX design.

angular misalignment at the input of the optical system, which for the proposed system can be written in terms of matrix optics as (cf. Fig. 5.8)

$$\begin{bmatrix} r_o \\ \theta_o \end{bmatrix} = M_4 \cdot M_3 \cdot M_2 \cdot M_1 \begin{bmatrix} r_i \\ \theta_i \end{bmatrix} = \begin{bmatrix} 1 & d_4 \\ 0 & 1 \end{bmatrix} \cdot \begin{bmatrix} 1 & 0 \\ -\frac{1}{f_A} & 1 \end{bmatrix} \cdot \begin{bmatrix} 1 & l_{\text{KT}} \\ 0 & 1 \end{bmatrix} \cdot \begin{bmatrix} 1 & 0 \\ -\frac{1}{f_{\text{tel}}} & 1 \end{bmatrix} \cdot \begin{bmatrix} r_i \\ \theta_i \end{bmatrix}, \quad (5.6)$$

where  $r_i$  and  $\theta_i$  represent the ray lateral and angular displacement, respectively, in the plane of the telescope input,  $r_o$  and  $\theta_o$  represent the ray lateral and angular displacement, respectively, in the plane of the GRIN input aperture.  $M_i$  stand for the matrices of the individual subsystems of the receiver (cf. Fig. 5.8); telescope modelled as a convex lens  $M_1$ , space between telescope and asphere  $M_2$ , aspheric lens  $M_3$  and space between asphere and GRIN lens  $M_4$ ;  $l_{\text{KT}} = f_{\text{tel}} + f_{\text{A}}$  represents the distance between telescope and asphere and  $d_4$  represents the distance between asphere and GRIN lens. Multiplying the matrices yields

$$\begin{bmatrix} r_o \\ \theta_o \end{bmatrix} = \begin{bmatrix} d_4 \left( \frac{f_A + f_{\text{tel}}}{f_A f_{\text{tel}}} - \frac{1}{f_A} - \frac{1}{f_{\text{tel}}} \right) - \frac{f_A}{f_{\text{tel}}} & \frac{f_{\text{tel}}}{f_A} d_4 + f_A + f_{\text{tel}} \\ 0 & -\frac{f_{\text{tel}}}{f_A} \end{bmatrix} \begin{bmatrix} r_i \\ \theta_i \end{bmatrix}. \quad (5.7)$$

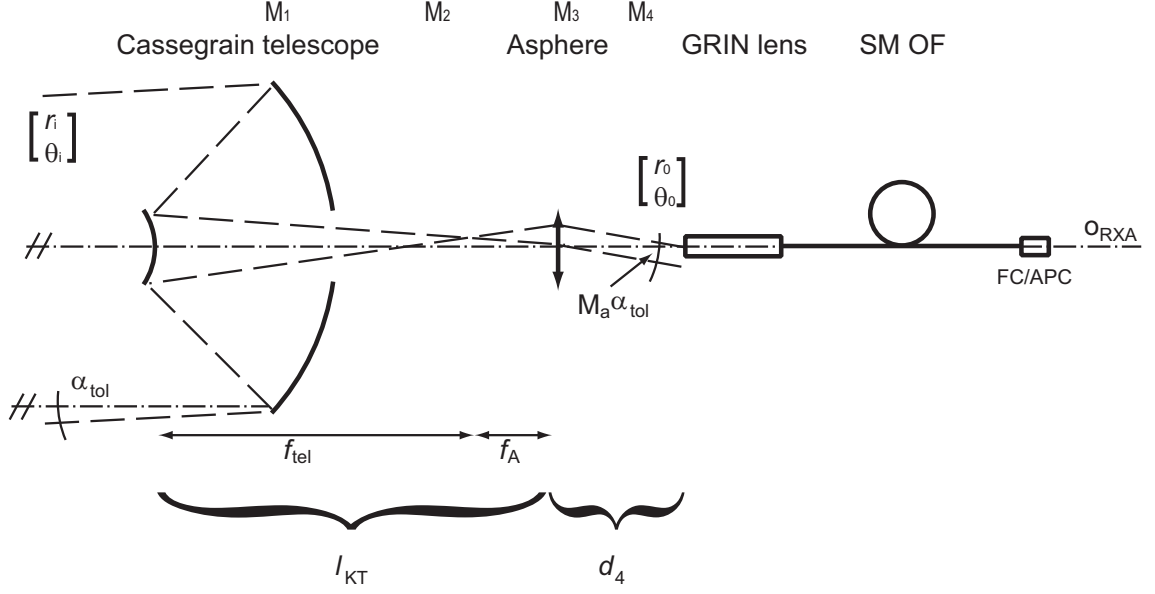


Fig. 5.8: Schematic representation of the angular alignment tolerance  $\alpha_{\text{tol}}$  of the proposed receiver.  $r_i$  and  $\theta_i$  represent the ray lateral and angular displacement, respectively, in the plane of the telescope input,  $r_o$  and  $\theta_o$  represent the ray lateral and angular displacement, respectively, in the plane of the GRIN input aperture,  $M_1$ ,  $M_2$ ,  $M_3$  and  $M_4$  represent matrices of the telescope, space between telescope and asphere, aspheric lens and space between asphere and GRIN lens. Not to scale.

From here, the alignment tolerance estimation yields

$$r_o = \left( \frac{f_{\text{tel}}}{f_A} d_4 + f_A + f_{\text{tel}} \right) \theta_i. \quad (5.8)$$

Let's assume that  $r_o$  should not exceed the radius of the input aperture of GRIN  $r_G$  and that  $\theta_i = \alpha_{\text{tol}}$ . Then, the angular ray misalignment at the RXA is

$$\alpha_{\text{tol}} < \frac{r_G}{M_A d_4 + f_A + f_{\text{tel}}}, \quad (5.9)$$

which after substitution of the parameters from Table 5.1 yields

$$\alpha_{\text{tol}} < \frac{5 \cdot 10^{-4}}{277 \cdot 10^{-2} + 4.51 \cdot 10^{-3} + 1.25} = 0.12 \text{ mrad} = 0.007^\circ, \quad (5.10)$$

which is smaller than the used divergence by one order of magnitude. The estimation in (5.9) directly determines the half-angle of receiver's FOV  $\theta_{\text{FOV}}$ .

Now, using Eq. (5.7), will be shown the derivation of expression for angular magnification  $M_a$  defined after (5.1) and the expression (5.2) for beam size at the input of GRIN lens  $D_A$ . The angular magnification  $M_a$  can be derived from Eq. (5.7) for zero displacement  $r_o$  and  $r_i$  as

$$\theta_o = -\frac{f_{\text{tel}}}{f_A} \theta_i, \quad (5.11)$$

from which the angular magnification  $M_a$  is

$$M_a = \frac{\theta_o}{\theta_i} = -\frac{f_{\text{tel}}}{f_A}, \quad (5.12)$$

which for negative  $f_A$  (concave lens) yields magnification of the Galileian telescope (upright image), whereas for positive  $f_A$  (convex lens) yields magnification of the Keplerian telescope (inverted image).

Similarly, for beam size  $D_A$  Eq. (5.7) yields for zero angular displacement  $\theta_o$  and  $\theta_i$

$$r_o = \left[ d_4 \left( \frac{f_A + f_{\text{tel}}}{f_A f_{\text{tel}}} - \frac{1}{f_A} - \frac{1}{f_{\text{tel}}} \right) - \frac{f_A}{f_{\text{tel}}} \right] r_i, \quad (5.13)$$

from which I derived, assuming  $r_o = D_A$  and  $r_i = D_{\text{RXA}}$ , for the beam size at the input of GRIN lens

$$D_A = \left[ d_4 \left( \frac{f_A + f_{\text{tel}}}{f_A f_{\text{tel}}} - \frac{1}{f_A} - \frac{1}{f_{\text{tel}}} \right) - \frac{f_A}{f_{\text{tel}}} \right] D_{\text{RXA}}, \quad (5.14)$$

from which the  $D_A$  can be calculated using parameters in Table 5.1

$$\begin{aligned} D_A &= \left[ 10^{-2} \left( \frac{4.51 \cdot 10^{-3} + 1.25}{4.51 \cdot 10^{-3} \cdot 1.25} - \frac{1}{4.51 \cdot 10^{-3}} - \frac{1}{1.25} \right) - \frac{4.51 \cdot 10^{-3}}{1.25} \right] 0.125 = \\ &= 4.51 \cdot 10^{-4} \text{ m} = 0.451 \text{ mm}, \end{aligned} \quad (5.15)$$

which is in agreement with the result of Eq.(5.2).

In order to verify this estimation, one can benefit from using a computer SW (e.g. ZEMAX) [63].

Due to low FOV of the proposed RX OMA and its tolerance to alignment derived in (5.9) the system, even when ideally aligned, might suffer from critical power fluctuations due to wavefront disturbance causing change in the angle of arrival (AoA) of the optical wave [64]. This angular change of the wavefront incident angle relative to the optical axis is in the order of tens of microradians [65, 66]. In order to compensate for the wavefront disturbance due to turbulence effects, adaptive optics techniques can be used [67, 68, 69].

### 5.3 Non-standard atmospheric effects

The following text discusses effects, not directly related to the OAM design, responsible for availability deterioration (e.g. building and terminal sway, cover window dewing and lensing effect from raindrops) that the author refers to as non-standard atmospheric effects [70]. The author presented the topic of non-standard effects to the international COST IC1101 community at its biannual meetings and other conferences [5, 70], where it was very well acknowledged.

Not only turbulence is responsible for the AoA fluctuation, but also building and terminal sway. Dependency of the wind speed, direction, link and beam geometry has been discussed in Chapter 4.4. Since there is now general link location, one cannot generalise the influence of the wind on the specific building or terminal stand. It is recommended, however, to take into account this effect prior to the OAM design in order to optimise 1) long-term statistics of the wind speed and direction at the given location, 2) terminal's shape and size, 3) required terminal reliability and link availability and 4) robustness of the terminal stand. The optimisation process is schematically depicted in Fig. 5.9, where tight relation between all of these four parameters is shown.

In terms of wind-induced fading, the aerodynamics of the terminal design is essential. Not only are the curved (rounded) shapes preferred from the rectangular, but also the all-optical transceivers concept allows for more compact terminal design. The all-optical transceiver may be divided into an internal unit with all electronics (laser current drivers) and optics, leaving only the final fibres for signal transmission and reception together with the OMA in the external unit. This approach leaves all the necessary electronics and optical components (lasers, photodiodes) in a more or less stabilised and controlled conditions. Although to change the link direction is not always feasible, it is optimal to turn it along the direction of the highest probability of the wind direction according to the long-term measurements.

The terminal stand serves for the attachment of the terminal to a building or post, for the mechanical isolation from the building as well as for its alignment. Once aligned, the stand should maintain the terminal's direction. Often, this terminal is designed as a rigid construction, which is more sensitive to possible vibrations from the outside environment giving rise to fast fading. On the other hand, more elastic construction design may damp the high-frequency vibrations, but is more liable to wind-induced slow fading. The building sway cannot be neglected and often is responsible for link outages, especially for high-rise buildings in a windy areas or during earthquakes. Although it cannot be avoided, using an elliptically symmetrical beam with the main axis positioned vertically can minimise the wind-induced losses [40].

Reliability of the system and link availability are features closely related to each other. While the first one being mainly determined by the terminal electrical and OMA design and the latter influenced by the atmospheric environment along the beam path, one must first improve the system reliability in order to increase the overall link availability.

Last, but not least, the location statistics serve mainly as an input to the link availability estimation models. Based on the long-term statistics, one can improve the system design in order to minimise the wind-induced deteriorating effects and

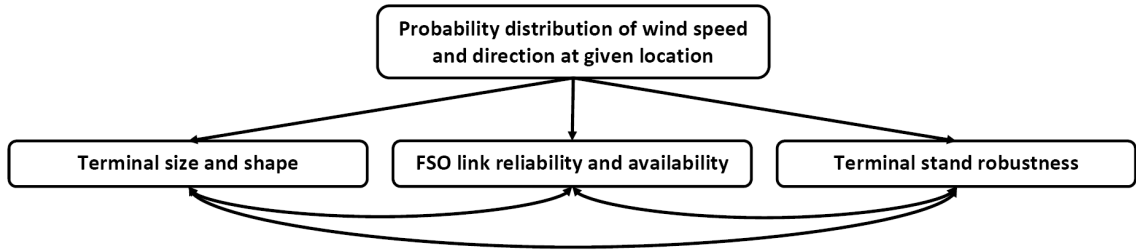


Fig. 5.9: Wind-related FSO link availability estimation model.

hence increase the overall availability of the system based on the recommendations above. Having determined the wind-related statistical parameter of the location and either two of the three influences in Fig. 5.9, one can estimate the remaining feature. Be it terminal size and shape by the calculation of the aerodynamics drag and the FSO link availability and the required terminal stand robustness from the misalignment model presented in Chapter 4.

Sunlight has been identified as the (background) noise source not only in optical receivers, but in transmitters as well. The purpose of a monitoring photodiode in a laser diode package (module) is to collect a portion of light emitted by a photodiode and to stabilise it in a closed-loop. Due to the sunlight incident into a laser source, the monitoring photodiode detects an increased optical power and decreases the laser diode current. This behaviour is then misinterpreted at the receiver as an additional attenuation even in case of clear-sky conditions [71]. Although this effects is usually observed only at specific day time for several days and twice a year for a certain link direction, it may give rise to severe decrease in the overall link availability. Influence of the solar radiation background noise is reduced at the receivers usually by an optical filter which transmits only specific wavelengths. An advantage of the proposed design is also high attenuation of the solar radiation incident back on the transmitter due to a relatively small diameter of the fibre core and the reflective coating on the TX lens. Laser sources are protected from unwanted radiation also using optical fibre isolators in both branches.

The influence of the solar radiation on the measured attenuation data as well as the influence of other effects can be studied using duplex testing FSO links. Such links can be also used to study the phenomenon of cross-sensitivity of the measurement of atmospheric influence on various effects and on their homogeneity along the propagation path. Duplex measurement requires each of the terminals to be equipped with both the transmitter and the receiver and hence introduces a redundancy to the measurement. Comparison of the measured data from both directions would effectively reveal inhomogeneity along the path, whether its inhomogeneity of a meteorological event (rain, fog) or misalignment of one of terminals. In case of

data mismatch, these data would be excluded from further analysis as faulty.

Last, but not least significant, effect observed during development of FSO receiver is the inhomogeneous dependency of the sensitivity of photodiode's active area. This effect gives rise to unstable output current reading from PD when the received beam is focused not ideally in its centre, but rather close to the edge of PD [72]. An advantage of the proposed RX design is that it allows to connect a pigtailed PD to its output, where the relative position of the OF and PD is fixed and optimised, what eliminates the dependency of the output current of the PD on the beam position on its active area.

## 5.4 Summary

This last chapter covers the development of the optomechanical assembly of an all-optical (fully photonic) transceiver, mainly for data transmission and testing applications. The transceiver OMA consists out of two parts: transmitter and receiver optics.

The transmitter part is designed as a dual-wavelength all-optical single-aperture system. It is suitable for the transmission of two different wavelengths at each input (850 nm and 1550 nm), which can be used to separate data streams, to separate users, to provide beacon along with the primary beam or to study spectral dependency of different atmospheric effects. These beams need to be merged into a single beam due to random mechanical misalignment of the individual transmitter OMA. In the chapter I showed that in order to merge beams with wavelengths 850 nm and 1550 nm, respectively, one cannot use a WDM due to unstable output power in one of the branches. However, I showed, how a dual-core OF can be used to overcome this difficulty. Both beams then propagate within the same atmospheric volume and their axis are nearly identical and always parallel to each other. The dual-core fibre is then placed near the focal point of an aspherical lens to generate slightly divergent beam optimal for application in terrestrial free-space optical links. Application of POF as the final fibre in the DAS transmitter was also discussed.

The receiver OMA serves for focusing of the received optical beam on to the active area of a photodiode. In all-optical links, it is used to couple to beam from the free-space to a SM OF. Commercially available solutions provide too small aperture sizes (simple aspherical or ball lens) or expensive solutions (adaptive optics). I presented an OMA of the receiver consisting of a Cassegrain telescope in focal mode, which together with an aspherical lens form a Keplerian telescope. At the output of such system, one obtains collimated beam, which can be coupled into an SM OF using a GRIN lens attached to its end. The performance of the proposed

system was analysed by means of the geometrical optics in terms of its angular magnification, and beam size at the input of a GRIN lens. I showed that the maximal angular misalignment (pointing error) of the system is one order of the magnitude higher than the fluctuation of the angle of arrival of the beam transmitted through a turbulent atmosphere. Therefore I concluded that it can be used for terrestrial FSO link applications.

Finally, I introduced the term of non-standard atmospheric effects and discussed its influence on FSO link performance.

Author also contributed to the development of an FSO link with FPGA-based Ethernet media converter, which was published in [73] and registered as a functional sample (prototype). Selected results were published also in [5, 18, 54, 70, 74].

## 6 CONCLUSION

The dissertation summarises the state-of-the-art in OWC field, where despite its many benefits, one finds a lack of a thorough analysis of various aspects and effects of wave, electromagnetic, geometrical or atmospheric nature.

Fraunhofer diffraction effects (far-field diffraction) have been well described mainly in terms of the beam broadening effect in FSO links. One of the most influential wave effect in OWC nowadays is the Fresnel diffraction, which is also one of the main focuses of the dissertation. Fresnel effects are well known in structural analysis of materials, however, the dissertation sets them into a new aspect of FSO links, where it hasn't been thoroughly studied so far. The thesis then defines the divergent elliptical Gaussian beam as an appropriate approximation of a real laser beam used in FSO systems nowadays. This beam is used as an input function for Fresnel diffraction integral, which for the first time, introduces and defines Fresnel diffraction integral of a divergent elliptical Gaussian beam restricted by a circular aperture. The expression is in form of Fourier transform and in Cartesian coordinates, which offers straightforward computer simulations of the near-field diffraction effects.

The diffraction integral has been derived also in terms of Bessel function integration model. Although this model assumes circularly symmetrical scenario, it allowed for a definition of the diffraction pattern contrast, which was used to estimate the influence of the Fresnel diffraction on the performance of the FSO link. An optimal ratio between link distance, wavelength and transmitter aperture size was identified in order to minimise the diffraction pattern contrast and the systems's misalignment sensitivity associated with it.

Restriction of the beam gives rise not only to the aforementioned wave effects, but also to optical power attenuation, which was analysed by means of electromagnetic optics. The dissertation introduced four independent derivations of the geometrical attenuation calculations assuming elliptically symmetrical Gaussian beam on a circular receiver aperture. It also provided analysis of the impact of various misalignment scenarios on the link reliability and availability. The analysis is useful during the link design phase when the proper attenuation and misalignment analysis is crucial for link budget estimation.

Based on the aforementioned results, new challenge in the theoretical study of the diffraction effects can be set to analytically investigate the amount of the optical power being transmitted by a diffracting beam as a function of the restricting aperture size. There are analytical result assuming Fraunhofer diffraction and circular symmetry of the scenario, but to the best of my knowledge, no solution was presented for the Fresnel diffraction or for an elliptically symmetrical beam.

Last chapter introduces the design and development of an all-optical transceiver for testing and data FSO links. First, the design consideration of a dual-wavelength all-optical single-aperture transmitter have been presented utilising various optical components. Using a custom-made dual-core optical fibre I managed to merge two beams with wavelengths 850 nm and 1550 nm into a single optical fibre (final fibre), which illuminated a single collimating lens. Not only this design reduces number of objectives needed in a transmitter, but it also significantly improves reliability of the system in terms of mechanical stability. The two beams might either carry different information, or one serves as the beacon for pointing of the primary beam, or be used for measurement of the spectral dependency of the atmospheric attenuation in testing links.

Development of the receiver optomechanical assembly was more challenging due to the requirement on the receiver aperture size and limitation of the overall length. The design incorporates the Cassegrain telescope and the aspherical lens to form a Keplerian telescope. It produces a relatively small collimated beam, which is then focused into a single-mode fibre using the fibre-pigtailed GRIN lens. I presented the performance analysis by means of the geometric (matrix) optics to derive and optimise the relevant receiver parameters. The alignment tolerance showed that despite relatively low FOV, the receiver is capable of dealing with turbulence-induced change of the beam angle of arrival.

Last, but not least, the paper introduces and discusses non-standard atmospheric effects on FSO links, mainly taking into account their sensor-like behaviour when used for testing of the atmospheric impact on the optical beam propagation. Important outcome is the identification of the influence of the wind speed and direction and the rain drops impact on the terminal covers on the FSO link performance. The main contribution of this part is the identification of the weak points of the current FSO link design approach and the recommendation to its improvement in terms of the FSO link reliability.

## BIBLIOGRAPHY

- [1] K.-D. LANGER and J. GRUBOR, “Recent developments in optical wireless communications using infrared and visible light,” in *Transparent Optical Networks, 2007. ICTON '07. 9th International Conference on*, vol. 3, pp. 146–151, 2007.
- [2] E. LEITGEB, T. PLANK, P. PEZZEI, D. KRAUS, and J. POLIAK, “Integration of fso in local area networks – combination of optical wireless with wlan and dvb-t for last mile internet connections,” in *Proceedings of 2014 19th European Conference on Networks and Optical Communications*, pp. 120–125, 2014.
- [3] H. HENNIGER and O. WILFERT, “An introduction to free-space optical communications,” *Radioengineering*, vol. 19, no. 2, pp. 203–212, 2010.
- [4] A. K. MAJUMDAR and J. C. RICKLIN, *Free-Space Laser Communications: Principles and Advances*. Springer, 2008.
- [5] O. WILFERT and J. POLIAK, “New research areas in the field of terrestrial optical wireless links,” in *Proceedings of the 16th International Conference on Transparent Optical Networks ICTON 2014*, pp. 1–4, 2014.
- [6] N. PERLOT, E. DUCA, J. HORWATH, D. GIGGENBACH, and E. LEITGEB, “System requirements for optical hap-satellite links,” in *Communication Systems, Networks and Digital Signal Processing, 2008. CNSDSP 2008. 6th International Symposium on*, pp. 72–76, 2008.
- [7] H. HEMMATI, A. BISWAS, and I. DJORDJEVIC, “Deep-space optical communications: Future perspectives and applications,” *Proceedings of the IEEE*, vol. 99, no. 11, pp. 2020–2039, 2011.
- [8] V. E. ZUEV, *Laser Beams in the Atmosphere*. Plenum Publishing Corporation, 1982.
- [9] L. C. ANDREWS, *Laser Beam Propagation through Random Media*. SPIE Press, 2005.
- [10] H. HEMMATI, ed., *Near-Earth Laser Communications*. Boca Raton, FL: CRC Press, 2009.
- [11] Z. GHASSEMLOOY, W. POPOOLA, and S. RAJBHANDARI, *Optical wireless communications; system and channel modelling with MATLAB*. CRC Press, 2012.

- [12] P. W. KRUSE, L. D. MCGLAUCHLIN, and R. B. MCQUISTAN, *Elements of infrared technology: Generation, transmission and detection*. Wiley, 1962.
- [13] I. I. KIM, B. MCARTHUR, and E. J. KOREVAAR, “Comparison of laser beam propagation at 785 nm and 1550 nm in fog and haze for optical wireless communications,” in *Proc. SPIE 4214, Optical Wireless Communications III*, vol. 4214, pp. 26–37, 2001.
- [14] C. CAPSONI, L. LUINI, and R. NEBULONI, “Prediction of cloud attenuation on earth-space optical links,” in *Antennas and Propagation (EUCAP), 2012 6th European Conference on*, pp. 326–329, 2012.
- [15] G. PARCA, “Optical wireless transmission at 1.6-tbit/s (16x100 gbit/s) for next-generation convergent urban infrastructures,” *Optical Engineering*, vol. 52, p. 116102, Nov. 2013.
- [16] D. BOROSON, J. SCOZZAFAVA, D. MURPHY, B. ROBINSON, and H. SHAW, “The lunar laser communications demonstration (llcd),” in *Space Mission Challenges for Information Technology, 2009. SMC-IT 2009. Third IEEE International Conference on*, pp. 23–28, July 2009.
- [17] V. BRAZDA, V. SCHEJBAL, and O. FISER, “Rain impact on fso link attenuation based on theory and measurement,” in *Antennas and Propagation (EUCAP), 2012 6th European Conference on*, pp. 1239–1243, 2012.
- [18] V. BRAZDA, O. FISER, Z. CHLADOVA, J. POLIAK, and V. SCHEJBAL, “On wind influence on fso link attenuation,” in *Antennas and Propagation (EUCAP), 2013 7th European Conference on*, pp. 966–968, 2013.
- [19] O. WILFERT, Z. KOLKA, V. BIOLKOVA, P. KRIVAK, L. DORDOVA, O. FISER, and J. NEMECEK, “Dual optical wireless test link,” in *Proc. SPIE 7091, Free-Space Laser Communications VIII*, vol. 7091, pp. 70910W–70910W–8, 2008.
- [20] J. POLIAK, P. PEZZEI, E. LEITGEB, and O. WILFERT, “Link budget for high-speed short-distance wireless optical link,” in *Communication Systems, Networks Digital Signal Processing (CSNDSP), 2012 8th International Symposium on*, pp. 1–6, 2012.
- [21] M. BORN and E. WOLF, *Principles of Optics*. Cambridge University Press, 2003.
- [22] F. M. GRIMALDI, *Physico mathesis de lumine, coloribus, et iride, aliisque annexis libri duo*. Bologna, Italy: Vitorio Bonati, 1665.

- [23] A. FRESNEL, “Mémoire sur la diffraction de la lumière,” *Mém. de l’Académie des Sciences*, pp. 247–382, 1818.
- [24] B. E. A. SALEH and M. C. TEICH, *Fundamentals of Photonics*. John Wiley & Sons, Inc., 1991.
- [25] J. KOMRSKA, “Difrakce světla,” 2000.
- [26] R. FEYNMAN, R. LEIGHTON, and M. SANDS, *The Feynman Lectures on Physics*. No. v. 1 in The Feynman Lectures on Physics, Addison-Wesley, 1963.
- [27] J. ALDA, “Laser and gaussian beam propagation and transformation,” *Encyclopedia of Optical Engineering*, pp. 999–1013, 2003.
- [28] A. E. SIEGMAN, *Lasers*. University Science Books, 1986.
- [29] E. a. HOVENAC, “Fresnel diffraction by spherical obstacles,” *American Journal of Physics*, vol. 57, no. 1, pp. 79 – 84, 1989.
- [30] F. SLIMANI, G. GREHAN, G. GOUESBET, and D. ALLANO, “Near-field lorenz-mie theory and its application to microholography,” *Appl. Opt.*, vol. 23, pp. 4140–4148, Nov 1984.
- [31] I. S. GRADSHTEYN and I. M. RYZHIK, *Table of integrals, series, and products*. Elsevier/Academic Press, Amsterdam, seventh ed., 2007. Translated from the Russian, Translation edited and with a preface by Alan Jeffrey and Daniel Zwillinger, With one CD-ROM (Windows, Macintosh and UNIX).
- [32] R. L. LUCKE, “Rayleigh-Sommerfeld Diffraction vs Fresnel-Kirchhoff , Fourier Propagation , and Poisson’s Spot,” tech. rep., Naval Research Laboratory, 2004.
- [33] G. N. WATSON, *A Treatise On The Theory Of Bessel Functions*. London: Cambridge University Press, second ed., 1966.
- [34] C. J. R. SHEPPARD and M. HRYNEVYCH, “Diffraction by a circular aperture: a generalization of fresnel diffraction theory,” *J. Opt. Soc. Am. A*, vol. 9, pp. 274–281, Feb 1992.
- [35] M. E. HUFFORD and H. T. DAVIS, “The diffraction of light by a circular opening and the lommel wave theory,” *Phys. Rev.*, vol. 33, pp. 589–597, Apr 1929.
- [36] J. POLIAK, J. KOMRSKA, and O. WILFERT, “Restricted beam analysis for fso links,” in *Antennas and Propagation (EUCAP), 2012 6th European Conference on*, pp. 335–339, 2012.

- [37] J. SVĚTLÍK, “Simple methods for the measurement of laser beam parameters,” *Appl. Opt.*, vol. 13, pp. 1276–1278, Jun 1974.
- [38] G. D. GILLEN and S. GUHA, “Modeling and propagation of near-field diffraction patterns: A more complete approach,” *American Journal of Physics*, vol. 72, no. 9, p. 1195, 2004.
- [39] P. BARCÍK and L. HUDCOVÁ, “Measurement of Spatial Coherence of Light Propagating in a Turbulent Atmosphere,” *Radioengineering*, vol. 22, pp. 341–345, April 2013.
- [40] J. POLIAK, P. PEZZEI, P. BARCIK, E. LEITGEB, L. HUDCOVA, and O. WILFERT, “On the derivation of exact analytical fso link attenuation model,” *Transactions on Emerging Telecommunications Technologies*, vol. 25, no. 6, pp. 609–617, 2014.
- [41] J. POLIAK and O. WILFERT, “Extended model of restricted beam for fso links,” in *Proc. SPIE 8517, Laser Communication and Propagation through the Atmosphere and Oceans*, vol. 8517, pp. 851711–1–851711–8, 2012.
- [42] O. WILFERT, J. KOMRSKA, J. POLIAK, and Z. KOLKA, “Influence of optical elements on the laser beam profile,” in *Proc. SPIE 8162 Free-Space and Atmospheric Laser Communications XI*, pp. 81620V–81620V–7, 2011.
- [43] J. POLIAK, P. PEZZEI, E. LEITGEB, and O. WILFERT, “Analytical expression of fso link misalignments considering gaussian beam,” in *Network and Optical Communications (NOC), 2013 18th European Conference on and Optical Cabling and Infrastructure (OC&I), 2013 8th Conference on*, pp. 99–104, 2013.
- [44] S. BLOOM, E. KOREVAAR, J. SCHUSTER, and H. WILLBRAND, “Understanding the performance of free-space optics [invited],” *J. Opt. Netw.*, vol. 2, pp. 178–200, Jun 2003.
- [45] R. PAUDEL, J. POLIAK, Z. GHASSEMLOOY, and E. LEITGEB, “Modelling and analysis of fso ground-to-train communications for straight and curved tracks,” in *Antennas and Propagation (EuCAP), 2013 7th European Conference on*, pp. 3180–3184, 2013.
- [46] R. PAUDEL, J. POLIAK, Z. GHASSEMLOOY, O. WILFERT, and E. LEITGEB, “Curved track analysis of fso link for ground-to-train communications,” *Radioengineering*, vol. 23, pp. 452–459, April 2014.

- [47] R. TYSON, *Principles of Adaptive Optics*. CRC Press, third ed., 2010.
- [48] “<http://www.newport.com/>.”
- [49] “<http://www.thorlabs.com/>.”
- [50] “<http://www.ozoptics.com/>.”
- [51] J. M. SENIOR, *Optical Fiber Communications (3rd Ed.): Principles and Practice*. Hertfordshire, UK: Prentice Hall International (UK) Ltd., 2009.
- [52] L. HUDCOVA and P. BARCIK, “Experimental measurement of beam wander in the turbulent atmospheric transmission media,” in *Radioelektronika (RADIOELEKTRONIKA), 2012 22nd International Conference*, pp. 1–4, 2012.
- [53] M. MALIK, M. O’SULLIVAN, B. RODENBURG, M. MIRHOSSEINI, J. LEACH, M. P. J. LAVERY, M. J. PADGETT, and R. W. BOYD, “Influence of atmospheric turbulence on optical communications using orbital angular momentum for encoding,” *Opt. Express*, vol. 20, pp. 13195–13200, Jun 2012.
- [54] J. POLIAK and O. WILFERT, “Dual transmitter for optical testing links with optimized beam shape,” in *Radioelektronika (RADIOELEKTRONIKA), 2012 22nd International Conference*, pp. 1–4, 2012.
- [55] P. PATTANASATTAYAVONG, V. KULTAVEWUTI, W. THANOPACHAI, and W. MOHAMMED, “Dual core fiber for strain sensing applications,” in *Optical Fiber Communication Optoelectronic Exposition Conference, 2008. AOE 2008. Asia*, pp. 1–3, Oct 2008.
- [56] Y. B. LU and P. CHU, “Gain flattening by using dual-core fiber in erbium-doped fiber amplifier,” *Photonics Technology Letters, IEEE*, vol. 12, pp. 1616–1617, Dec 2000.
- [57] F. CHAN, P. SHUM, K. YASUMOTO, and E. SHARMA, “Modal analysis of asymmetric dual-core fibers,” in *PhotonicsGlobal@Singapore, 2008. IPGC 2008. IEEE*, pp. 1–3, Dec 2008.
- [58] L. DONG, T. BIRKS, M. OBER, and P. RUSSELL, “Intermodal coupling by periodic microbending in dual-core fibers-comparison of experiment and theory,” *Lightwave Technology, Journal of*, vol. 12, pp. 24–27, Jan 1994.
- [59] A. NICIA, “Lens coupling in fiber-optic devices: efficiency limits,” *Appl. Opt.*, vol. 20, pp. 3136–3145, Sep 1981.

- [60] CVI Melles Griot, *All Things Photonics [The CVI Melles Griot Technical Guide]*, 2-1 ed.
- [61] J. ANGENENT, G. KHOE, G. MAHON, A. van de GRIJP, C. POTTERS, and K. WRIGHT, “Low-reflection ball lens connector part,” June 11 1991. US Patent 5,022,733.
- [62] M. J. RIEDL, *Optical Design Fundamentals for Infrared Systems*. SPIE Press, second ed., 2001.
- [63] F. LEVANDER and P. SAKARI, “Design and Analysis of an All-optical Free-space Communication Link ,” Tech. Rep. FOI-R-0486-SE, FOI – Swedish Defence Research Agency Division of Sensor Technology, May 2002.
- [64] H. T. EYYBOGLU and Y. K. BAYKAL, “Effects of laser multimode content on the angle-of-arrival fluctuations in free-space optical access systems,” in *Proc. SPIE 5473, Noise in Communication*, vol. 5473, pp. 184–190, 2004.
- [65] H. T. EYYBOGLU and Y. BAYKAL, “Angle-of-arrival fluctuations for general-type beams,” *Optical Engineering*, vol. 46, no. 9, pp. 096001–096001–8, 2007.
- [66] L. PENG and W. XUEYING, “Angle-of-arrival measurement system with high-frame rate cmos camera,” in *Imaging Systems and Techniques (IST), 2011 IEEE International Conference on*, pp. 7–11, May 2011.
- [67] E. J. KIBBLEWHITE and M. R. CHUN, “Design of tip-tilt and adaptive optics servos using measured angle-of-arrival and phase power spectra,” in *Proc. SPIE 3353, Adaptive Optical System Technologies*, vol. 3353, pp. 522–530, 1998.
- [68] H. HEMMATI and N. A. PAGE, “Preliminary optomechanical design for the x2000 transceiver,” in *Proc. SPIE Free-Space Laser Communication Technologies XI*, vol. 3615, pp. 206–211, 1999.
- [69] K. SHORTT, D. GIGGENBACH, R. MATA-CALVO, F. MOLL, C. FUCHS, C. SCHMIDT, J. HORWATH, J. YEH, V. SELVARAJ, and R. BANARJEE, “Channel characterization for air-to-ground free-space optical communication links,” in *Proc. SPIE 8971, Free-Space Laser Communication and Atmospheric Propagation XXVI*, vol. 8971, pp. 897108–897108–13, 2014.
- [70] O. WILFERT, J. POLIAK, P. BARCÍK, J. L. ARCE-DIEGO, F. FANJUL-VELÉZ, I. SALAS-GARCÍA, and N. ORTEGA QUIJANO, “Detection of non-standard atmospheric effects in fso systems,” in *Proc. SPIE 8874, Laser Communication and Propagation through the Atmosphere and Oceans II*, vol. 8874, pp. 88740S–88740S–8, 2013.

- [71] V. BRAZDA, O. FISER, L. REJFEK, and M. MANDLIK, “Attenuation of optical signal in free space & event analysis,” in *Proceedings of the Microwave and Radio Electronics Week 2013 (MAREW 2013)*, 2013.
- [72] M. DURAK, F. SAMADOV, and A. K. TURKOGU, “Spatial non-uniformity measurements of large area silicon photodiodes,” *Turkish Journal of Physics*, vol. 26, pp. 375–379, Sep 2002.
- [73] J. POLIAK and M. KUBÍČEK, “Fpga-based media converter for fso links,” in *Optical Wireless Communications (IWOW), 2013 2nd International Workshop on*, pp. 157–161, Oct 2013.
- [74] M. PAVLŮ and J. POLIAK, “Modeling of the multichannel optical wireless link,” in *Microwave Techniques (COMITE), 2013l Conference on*, pp. 79–82, April 2013.

# LIST OF SYMBOLS, PHYSICAL CONSTANTS AND ABBREVIATIONS

$a$	Wave amplitude
$A$	Complex envelope
$C$	Contrast
$C_R$	Scaling coefficient of Rayleigh scattering model
$D$	Diameter
$D_a$	Diameter of photodiode's active area
$D_A$	Beam diameter at the output of asphere
$D_{GRIN}$	Diameter of the GRIN active area
$D_{RXA}$	Diameter of the receiver telescope
$D_{TXA}$	Diameter of the transmitter lens
$f$	Focal length of lens
$f_{RXA}$	Focal length of the receiver optics
$f_{TXA}$	Focal length of the transmitter lens
$f\#$	F-number of lens
$\mathcal{F}$	Fourier Transform
$h$	Height of a building
$i$	Imaginary Unit
$I$	Optical intensity
$I_0$	Modified Bessel function of the first kind and order zero
$I_{max}$	Maximal optical intensity
$I_{min}$	Minimal optical intensity
$J_0$	Bessel function of the first kind and order zero
$\mathbf{k}$	Wave vector

$\mathbf{k}$	Gradient constant of GRIN lens
$K(\vartheta)$	Inclination factor
$l_{\text{KT}}$	Length of Keplerian telescope
$L$	Distance; range
$M$	Point in the plane $\Sigma_{\text{TXA}}$
$M_{\text{a}}$	Angular magnification
$M_i$	Matrix of the optical component $i$
$n$	Refractive index
$\mathbf{n}$	Unit vector in the direction of wave propagation
$N_{\text{f}}$	Fresnel number
$p$	Pitch of a GRIN lens
$P$	Optical power
$P$	Point in the plane $\Sigma_{\text{RXA}}$
$P_0$	Total optical power of the beam
$P_{\text{r}}$	Received optical power
$P_{\text{t}}$	Optical power of the unrestricted part of the beam
$q$	Scaling coefficient of Mie and Kruse model of atmospheric attenuation
$r$	Radius
$r$	Radial coordinate in the plane $\Sigma_{\text{RXA}}$
$r_{\text{G}}$	Radius of input aperture of GRIN
$r_{\text{i}}$	Input optical ray displacement
$r_{\text{n}}$	Radius of $n^{\text{th}}$ Fresnel zone
$r_{\text{o}}$	Output optical ray displacement
$r_{\text{OF}}$	Radius of OF core
$r_{\text{RXA}}$	Radius of receiver aperture

$r_{\text{TXA}}$	Radius of transmitter aperture
$R$	Beam's radius of curvature
$\mathbf{s}$	Position vector
$S$	Unrestricted part of the surface of the beam
$t$	Time
$t_0$	Initial time
$T$	Period
$U(u, v)$	Two-dimensional Lommel function
$v$	Phase velocity
$V$	Meteorological visibility
$w$	Gaussian beam half-width
$w_0$	Gaussian beam half-width at the waist
$x$	Cartesian coordinate x
$x_M$	Coordinate x in the plane $\Sigma_{\text{TXA}}$
$y$	Cartesian coordinate y
$y_M$	Coordinate y in the plane $\Sigma_{\text{TXA}}$
$z$	Cartesian coordinate z
$z_R$	Rayleigh distance
$\alpha$	Absorption coefficient
$\alpha_a$	Absorption coefficient from aerosols
$\alpha_{\text{app}}$	Approximative expression of geometrical attenuation
$\tilde{\alpha}_{\text{atm}}$	Attenuation of a clear atmosphere
$\alpha_{\text{ex}}$	Exact expression of geometrical attenuation
$\alpha_{\text{geom}}$	Geometrical attenuation
$\alpha_{\text{geom,circ}}$	Precise geometrical attenuation of a circular beam

$\alpha_{\text{geom,ellip}}$	Precise geometrical attenuation of an elliptical beam
$\alpha_i$	Initial phase
$\alpha_m$	Absorption coefficient from molecules
$\tilde{\alpha}_{\text{rain}}$	Attenuation coefficient of rain
$\tilde{\alpha}_{\text{snow}}$	Attenuation coefficient of snow
$\beta$	Scattering coefficient
$\beta_a$	Scattering coefficient from aerosols
$\beta_m$	Scattering coefficient from molecules
$\gamma$	Extinction coefficient
$\gamma_t$	Transmitter tilt angle
$\gamma_r$	Receiver tilt angle
$\delta_a$	Uncertainty of aperture setting
$\delta_c$	Uncertainty of collimation setting
$\delta_e$	Measurement error
$\delta_{\text{VPP}}$	Uncertainty of sensor readout
$\delta_z$	Uncertainty of distance measurement
$\Delta$	Displacement; Change of relative position of two objects
$\theta$	Half-angle of divergence
$\theta$	Angular coordinate in the plane $\Sigma_{\text{RXA}}$
$\theta_{\text{FOV}}$	Half-angle of field-of-view
$\theta_i$	Input optical ray angle of arrival
$\theta_o$	Output optical ray angle of arrival
$\vartheta$	Angle between normal to the plane $\Sigma_{\text{TXA}}$ and the direction $s$
$\lambda$	Wavelength
$\nu$	Frequency

$\rho$	Radial coordinate in the plane $\Sigma_{\text{TXA}}$
$\sigma$	Spherical wavefront
$\sigma_C^2$	Relative variance of laser beam motion
$\sigma_I^2$	Relative variance of optical intensity
$\Sigma_{\text{RXA}}$	Receiver plane
$\Sigma_{\text{TXA}}$	Transmitter plane
$\varphi$	Divergence
$\varphi$	Angular coordinate in the plane $\Sigma_{\text{TXA}}$
$\psi$	Wave function
$\psi_0$	Primary wave
$\omega$	Angular frequency
AoA	Angle-of-arrival
CCD	Charge-coupled device
cf.	lat. confer; Eng. compare
CWDM	Coarse Wavelength Division Multiplexer
DC	Dual-core
DWAOSA	Dual-Wavelength All-Optical Single-Aperture
DWDM	Dense Wavelength Division Multiplexer
e.g.	lat. exempli gratia; Eng. for instance
EDFA	Erbium-doped fibre amplifier
EFL	Effective focal length
EM	Electromagnetic
E/O	Electro-Optic
FFT	Fast Fourier Transform
FOV	Field of View

FSO Free-space Optics

GB Gaussian beam

GEO Geostationary Earth Orbit

GRIN Gradient Index of Refraction

He-Ne Helium-Neon

i.e. lat. id est; Eng. that is

IR Infrared

LD Lase Diode

LED Light-emitting diode

LEO Low Earth Orbit

Li-Fi Light Fidelity

LLST Lunar Lasercom Space Terminal

LOS Line-of-Sight

MCT Maksutov-Cassegrain telescope

MM Multi-mode

MMW Millimetre wave

NIR Near Infrared

NLOS Non-Line-of-Sight

O/E Opto-electronic

OF Optical Fibre

OGS Optical Ground Station

OI Optical Isolator

OMA Optomechanical assembly

OWC Optical Wireless Communications

PAT Pointing, Acquisition and Tracking

PF Perfluorinated  
PMMA Poly(methyl methacrylate)  
POF Plastic Optical Fibre  
RF Radio Frequency  
RX Receiver  
RXA Receiver Aperture  
SCT Schmidt-Cassegrain telescope  
SM Single-mode  
TX Transmitter  
TXA Transmitter Aperture  
UV Ultraviolet  
VIS Visible  
WDM Wavelength Division Multiplexer  
Wi-Fi Wireless Fidelity

# LIST OF APPENDICES

A Sheet specifications of used components

106

## A SHEET SPECIFICATIONS OF USED COMPONENTS

Item #	Thorlabs LP852-SF30
Wavelength	852 nm $\pm$ 5 nm
Threshold Current	20 to 50 mA
Optical Output Power	Typ. 30 mW
Fiber	SM800-5.6-125
Connector	FC/APC

Tab. A.1: Sheet specifications of 850 nm LD.

Item #	Thorlabs FPL1009S
Wavelength	1550 nm $\pm$ 20 nm
Threshold Current	35 to 55 mA
Optical Output Power	Typ. 100 mW
Fiber	SMF-28e+
Connector	FC/APC

Tab. A.2: Sheet specifications of 1550 nm LD.

Item #	Thorlabs SM800-5.6-125
Cladding Diameter	125 $\pm$ 1.0 $\mu$ m
Coating Diameter	245 $\pm$ 5%
Core-Clad Concentricity	< 1.0 $\mu$ m
Coating Material	Dual Acrylate
Proof Test Level	100 kpsi (1%)
Numerical Aperture (nominal)	0.10 – 0.14
Attenuation	<5 dB/km
Design Wavelength	830 nm
Cut-Off Wavelength	660 – 800 nm
Mode Field Diameter	5.6 $\mu$ m

Tab. A.3: Sheet specifications of SM800-5.6-125 fibre.

Item #	Thorlabs SM980-5.8-125
Cladding Diameter	$125 \pm 1.0 \mu\text{m}$
Coating Diameter	$245 \pm 5\%$
Core-Clad Concentricity	$< 0.75 \mu\text{m}$
Coating Material	Dual Acrylate
Proof Test Level	100 or 200 kpsi (1% or 2%)
Numerical Aperture (nominal)	0.13 – 0.15
Attenuation	$< 3 \text{ dB/km}$
Design Wavelength	980 / 1064 / 1550 nm
Cut-Off Wavelength	870 – 970 nm
Mode Field Diameter	$10.4 \mu\text{m} @ 1550 \text{ nm}$

Tab. A.4: Sheet specifications of SM980-5.8-125 fibre.

Item #	SMF-28e+
Core Diameter	8.2 micron
Cladding Diameter	$125 \pm 0.7 \mu\text{m}$
Coating Diameter	$245 \pm 5 \mu\text{m}$
Core-Clad Concentricity	$< 0.5 \mu\text{m}$
Coating-Clad Concentricity	$< 12 \mu\text{m}$
Numerical Aperture (nominal)	0.14
Attenuation	0.19 - 0.20 dB/km @ 1550 nm
Operating Wavelength	1260 - 1625 nm
Mode Field Diameter	$10.4 \pm 0.5 \mu\text{m} @ 1550 \text{ nm}$
Dispersion	$\leq 18.0 \text{ ps}/(\text{nm km}) @ 1550 \text{ nm}$

Tab. A.5: Sheet specifications of SMF-28e+ fibre.

Item #	Thorlabs IO-F-850APC
Polarization	Independent
Fiber Type	SM
Center Wavelength	850 nm
Operating Range	840 - 860 nm
Max Power	2 W (CW)
Isolation	30 - 38 dB
Insertion Loss (Without Connectors)	1.0 - 1.6 dB
Polarization Dependent Loss (PDL)	$\leq 0.25$ dB
Return Loss	$> 50$ dB
Fiber	780HP

Tab. A.6: Sheet specifications of IO-F-850APC optical isolator.

Item #	Thorlabs IO-H-1550APC
Polarization	Independent
Fiber Type	SM
Center Wavelength	1550 nm
Operating Range	1530 - 1570 nm
Max Power	300 mW (CW)
Isolation	$\geq 29$ dB
Insertion Loss (Without Connectors)	0.5 - 0.7 dB
Polarization Dependent Loss (PDL)	$\leq 0.15$ dB
Return Loss	$> 55/50$ dB (input/output)
Fiber	SMF-28e

Tab. A.7: Sheet specifications of IO-H-1550APC optical isolator.

Item #	Thorlabs WD202A
Fiber Type	Corning Flexcore 1060
MFD	5.9 micron @ 980 nm 6.2 micron @ 1060 nm
Cladding	$125.0 \pm 0.5 \mu\text{m}$
Coating	$245 \pm 10 \mu\text{m}$
Attenuation (Max)	2.1 dB/km @ 980 nm 1.5 dB/km @ 1060 nm
NA	0.14
Fiber Length	1 m
Fiber Jacket	900 $\mu\text{m}$ Loose Tube

Tab. A.8: Sheet specifications of fibre-optic WDM.

## Ing. Juraj Poliak

---

CONTACT INFORMATION	Technicka 12 Brno CZ-61600 Czech Republic tel: +420 54114 6558 fax: +420 54114 6597 mailto: xpolia00@stud.feec.vutbr.cz web: <a href="http://www.urel.feec.vutbr.cz/OptaBro/">http://www.urel.feec.vutbr.cz/OptaBro/</a>	Oponice 190 Oponice SK-95614 Slovak Republic mobile: +420 608 202 918 mobile: +421 948 666 165 poliak.juraj@gmail.com
CITIZENSHIP	Slovak Republic	
RESEARCH INTERESTS	Free-space optical communications modelling, optical wave effects – diffraction modelling, study of various optical environments in which the laser beam propagates, fully photonic FSO terminals and non-standard atmospheric phenomena.	
EDUCATION	<b>Brno University of Technology</b> , Brno, Czech Republic  09/2011 – 09/2014 (exp.) PhD. Candidate, Electronics and Communication <ul style="list-style-type: none"><li>• Thesis Topic: <i>Diffraction effects in the transmitted laser beam</i></li><li>• Supervisor: Prof. Otakar Wilfert</li></ul> 09/2009 – 06/2011 Master of Engineering (Dipl-Ing.), Electronics and Communication <ul style="list-style-type: none"><li>• Thesis Topic: <i>Effect of optical elements on transmitted laser beam</i></li><li>• Supervisor: Prof. Otakar Wilfert</li><li>• With results of the thesis author won 2<sup>nd</sup> prize on EEICT 2011</li><li>• Author was awarded the Dean price in 2011</li><li>• The thesis was acknowledged by the Lambert publishing house</li></ul> 09/2005 – 06/2009 Bachelor of Engineering (Bc.), Electronics and Communication <ul style="list-style-type: none"><li>• Thesis Topic: <i>Synchronnous detection of modulated optical signals</i></li><li>• Supervisor: Dr. Petr Drexler</li></ul> <b>Masaryk University</b> , Brno, Czech Republic  09/2007 – 06/2010 Bachelor of Physics (Bc.), Applied Physics – Astrophysics <ul style="list-style-type: none"><li>• Thesis Topic: <i>Detection of Radioastronomical Sources</i></li><li>• Supervisor: Dr. Filip Hroch</li><li>• The thesis was acknowledged by the Lambert publishing house</li></ul>	
ACADEMIC APPOINTMENTS	<b>PhD. Candidate</b> Department of Radio Electronics, Brno University of Technology <ul style="list-style-type: none"><li>• since 08/2011 member of OptaBro – the Optical Communications Research Group</li><li>• since 06/2012 research assistant at CEITEC – Central European Institute of Technology</li><li>• since 01/2013 PhD. student employee at SIX – Sensor, Information and Communication Systems Centre</li><li>• experience with national, international, European and ESA project proposals</li><li>• active member of COST Action IC1101 Opticwise</li></ul> <b>Teaching Assistant</b> <ul style="list-style-type: none"><li>• Quantum and Laser Electronics (winter semester 2011)</li><li>• Optical Communication Fundamentals and Optoelectronics (summer semester 2013)</li><li>• Computer and Communication Networks (summer semester 2013)</li></ul>	since 09/2011
RESEARCH STAYS	<b>Graz University of Technology, Austria</b> <ul style="list-style-type: none"><li>• Supervisor Prof. Erich Leitgeb, leader of the Research Group for Optical Communications (OptiKom), Institute of Microwave and Photonics Engineering</li><li>• Development of general analytical (elliptical) Gaussian beam free-space attenuation model for FSO links considering various misalignments</li><li>• Passed exams in Optical Communications (in German) with ”‘Excellence’”</li></ul>	01/2012 – 03/2012

**Pforzheim University of Applied Sciences, Germany** 10/2012 – 12/2012

- Supervisor: Prof. Friedemann Mohr, leader of the Electrooptics and Measurement & Instrumentation Lab, Dept. of Information Technology
- Derivation of the mathematical model of the Y-branch laser tuning characteristics for use in sensor applications

PROFESSIONAL  
EXPERIENCE

**FEI, Czech republic**, Brno, Czech Republic

**02/2010 to 10/2011** *Intern for Technical Support Group*

- Quality-related data mining supporting design changes on electron microscopes
- Processing of proposals and requirements (SW, HW, electronics) on new products

**Motorola**, Brno, Czech Republic

**06/2007 to 09/2007** *Service technician*

- Service of barcode readers
- Quality inspection of wireless modules for various products

COMPUTER SKILLS

**Programming languages** Matlab (advanced user), MathCAD (advanced user), VBA (certified advanced user), Python, C/C++

**Office tools** Proficient LaTeX and Microsoft Office (Word, Excel, Outlook, Powerpoint) user, Certified advanced user of Excel 2007 (Certificate of advanced methods and functions in Microsoft Excel 2007)

**Specialized SW** Zemax, PSpice, Eagle, Origin Pro

LANGUAGE SKILLS **Slovak** native speaker

**Czech** advanced

**English** advanced (ESOL CAE-C1 level passed, 78 %)

**Italian** upper-intermediate

**German** intermediate

**Spanish** basic knowledge of the language

MISCELLANEOUS Driving license category A1, B (pursuing B+E); 100k+ km driving experience

PERSONAL QUALITIES Hard-working, team player, flexible, self-motivated.

HOBBIES Music, Physics, Travelling, Flying.

## Ing. Juraj Poliak – List of publications

---

- CONTACT INFORMATION Technicka 12  
Brno CZ-61600  
Czech Republic  
tel: +420 54114 6558  
fax: +420 54114 6597  
mailto: xpolia00@stud.feec.vutbr.cz  
web: <http://www.urel.feec.vutbr.cz/OptaBro/>
- Oponice 190  
Oponice SK-95614  
Slovak Republic  
mobile: +420 608 202 918  
mobile: +421 948 666 165  
poliak.juraj@gmail.com
- IMPACTED JOURNAL PAPERS POLIAK, J.; PEZZEI, P.; BARCÍK, P.; LEITGEB, E.; HUDCOVÁ, L.; WILFERT, O.  
On the derivation of exact analytical FSO link attenuation model. *Transactions on Emerging Telecommunications Technologies*, 2014, vol. 25, no. 6, pp. 609-617. ISSN: 2161- 3915.
- PAUDEL, R.; POLIAK, J.; GHASSEMLOOY, Z.; WILFERT, O.; LEITGEB, E. Curved Track Analysis of FSO Link for Ground-to-Train Communications. *Radioengineering*, 2014, vol. 23, no. 1, pp. 452-459. ISSN: 1210- 2512.
- DOBESCH, A.; POLIAK, J. IR Thermometer with Automatic Emissivity Correction. *Radioengineering*, 2013, vol. 22, no. 4, pp. 1301-1306. ISSN: 1210- 2512.
- CONFERENCE PUBLICATIONS LEITGEB, E.; PLANK, T.; PEZZEI, P.; KRAUS, D.; POLIAK, J. Integration of FSO in Local Area Networks – Combination of Optical Wireless with WLAN and DVB- T for Last Mile Internet Connections. In *Proceedings of 2014 19th European Conference on Networks and Optical Communications (NOC)*. Milano, Italy: 2014. pp. 120-125. ISBN: 978-1-4799-3872- 8.
- WILFERT, O.; POLIAK, J. New Research Areas in the Field of Terrestrial Optical Wireless Links. In *Proceedings of the 16th International Conference on Transparent Optical Networks ICTON 2014*. Warsaw, Poland: National Institute of Telecommunications, Department of Transmission and Optical Technologies, 2014. pp. 1-4. ISBN: 978-1-4799-5600- 5.
- SALAS-GARCÍA, I.; FANJUL-VÉLEZ, F.; ORTEGA-QUIJANO, N.; WILFERT, O.; HUDCOVÁ, L.; POLIAK, J.; BARCÍK, P. Analysis of thermal effects in endoscopic nanocarriers- based Photodynamic Therapy applied to esophageal diseases. In *Proc. SPIE 8941, Optical Interactions with Tissue and Cells XXV; and Terahertz for Biomedical Applications*. 15. Bellingham: SPIE, 2014. pp. 84910C- 1 (89410C-6 s.)ISBN: 978-0-8194-9854- 0.
- POLIAK, J.; PEZZEI, P.; LEITGEB, E.; WILFERT, O. Analytical Expression of FSO Link Misalignments Considering Gaussian Beam. In *Proceedings of the 2013 18th European Conference on Network and Optical Communications & 2013 8th Conference on Optical Cabling and Infrastructure (NOC-OC&I)*. Graz: TU Graz, 2013. pp. 99-103. ISBN: 978-1-4673-5822- 4.
- POLIAK, J.; KUBÍČEK, M. FPGA- based Media Converter for FSO Links. In *Proceedings of 2013 2nd International Workshop on Optical Wireless Communications (IWOW)*. Newcastle upon Tyne: 2013. pp. 157-161. ISBN: 978-1-4799-1188-2.
- POLIAK, J.; HEININGER, H.; MOHR, F.; WILFERT, O. Modelling of MG- Y laser tuning characteristics. In *Proceedings of SPIE Optics & Photonics 2013 Conference on Infrared Sensors, Devices, and Applications III*. San Diego: SPIE Press, 2013. pp. 1-7. ISBN: 978-0-8194-9718-5.
- POLIAK, J.; PEZZEI, P.; LEITGEB, E.; WILFERT, O. Analytical Expression of FSO Link Misalignments Considering Gaussian Beam. In *Proceedings of the 2013 18th European Conference on Network and Optical Communications & 2013 8th Conference on Optical Cabling and Infrastructure (NOC-OC&I)*. Graz: TU Graz, 2013. pp. 99-103. ISBN: 978-1-4673-5822- 4.

- WILFERT, O.; POLIAK, J.; BARCÍK, P.; ARCE-DIEGO, J.; FANJUL-VÉLEZ, F.; SALAS-GARCÍA, I.; ORTEGA-QUIJANO, N. Detection of non- standard atmospheric effects in FSO systems. In SPIE Optics & Photonics 2013 Conference on Laser Communication and Propagation through the Atmosphere and Oceans II. San Diego: SPIE Press, 2013. pp. 1-8. ISBN: 978-0-8194-9724- 6.
- PEZZEI, P.; STIEBLER, N.; PLANK, T.; POLIAK, J.; LEITGEB, E.; LÖSCHNIGG, M. Measurement system for analyzing the spectral radiation pattern of light sources for FSO systems. In SPIE Optics & Photonics 2013 Conference on Laser Communication and Propagation through the Atmosphere and Oceans II. San Diego: SPIE Press, 2013. pp. 1-11. ISBN: 978-0-8194-9724- 6.
- BRÁZDA, V.; FIŠER, O.; CHLÁDOVÁ, Z.; POLIAK, J.; SCHEJBAL, V. On wind influence on FSO link attenuation. In Proceedings of the European Conference on Antennas and Propagation, EuCAP 2013. Gothenburg: 2013. pp. 966-968. ISBN: 978-88-907018-3- 2.
- PAUDEL, R.; POLIAK, J.; GHASSEMLOOY, Z.; LEITGEB, E. Modelling and Analysis of FSO Ground-to- Train Communications for Straight and Curved Tracks. In Proceedings of the European Conference on Antennas and Propagation, EuCAP 2013. 2013. pp. 1-5. ISBN: 978-88-907018-1-8.
- PAVLŮ, M.; POLIAK, J. Modeling of the multichannel optical wireless link. In Proceedings of the 23rd International Conference Radioelektronika 2013. 2013. pp. 1-4. ISBN: 978-1-4673-5513- 1.
- SALAS-GARCÍA, I.; FANJUL-VÉLEZ, F.; ORTEGA-QUIJANO, N.; POLIAK, J.; HUDCOVÁ, L.; WILFERT, O.; ARCE-DIEGO, J. Heat Generation in Biological Tissues during Photodynamic Therapy combined with Gold Nanoparticles. In Proceedings of 22nd International Conference Radioelektronika 2012. 2012. pp. 183-186. ISBN: 978-80-214-4468- 3.
- POLIAK, J.; WILFERT, O. Dual Transmitter for Optical Testing Links with Optimized Beam Shape. In Proceedings of 22nd International Conference Radioelektronika 2012. Brno: 2012. pp. 187-190. ISBN: 978-80-214-4468- 3.
- POLIAK, J.; KOMRSKA, J.; WILFERT, O. Restricted Beam Analysis for FSO Links. In Proceedings of the 6th European Conference on Antennas and Propagation (EUCAP). Praha: Garant s.r.o., 2012. pp. 1-5. ISBN: 978-1-4577-0919- 7.
- POLIAK, J.; WILFERT, O. Extended Model of the Restricted Beam for FSO links. In Proceedings of the Optics & Photonics 2012 Conference on Laser Communication and Propagation through the Atmosphere and Oceans. San Diego: SPIE, 2012. pp. 1-8. ISBN: 978-0-8194-9234-0.
- POLIAK, J.; PEZZEI, P.; LEITGEB, E.; WILFERT, O. Link budget for high-speed short-distance wireless optical link. In Proceedings of the 2012 8th International Symposium on Communication Systems, Networks & Digital Signal Processing (CSNDSP). 2012. pp. 1-6. ISBN: 978-1-4577-1471-9.
- POLIAK, J. Effect of Optical Elements on Transmitted Laser Beam. In Proceedings of the 17th conference Student EEICT. Brno: NOV PRESS, 2011. pp. 50-52. ISBN: 978-80-214-4272- 6.
- WILFERT, O.; POLIAK, J. Influence of Diffraction Effect on FSOL function. In Proceedings of National Conference on Emerging Areas of Photonics and Electronics (EAPE 2011). Kolkata: DE & CE, 2011. pp. 10-15.
- POLIAK, J.; KOMRSKA, J.; WILFERT, O. Wave Effects in FSO Links and Their Influence on Transmitted Laser Beam. In Optické Komunikace 2011. Praha: Agentura Action M, 2011. pp. 62-65. ISBN: 978-80-86742-32- 8.
- WILFERT, O.; KOMRSKA, J.; POLIAK, J.; KOLKA, Z. Influence of Optical Elements on the Laser Beam Profile. In Proceedings of the Optics & Photonics 2011 Conference on Free- Space and Atmospheric Laser Communications XI. San Diego: SPIE, 2011. pp. 1-7. ISBN: 978-0-8194-8772-8.